#1

IMAGING OF OBJECTS VIEWED THROUGH A TURBULENT ATMOSPHERE

JOHN C. MOLDON

TECHNICAL REPORT 469

MARCH 3, 1969

MASSACHUSETTS INSTITUTE OF TECHNOLOGY
RESEARCH LABORATORY OF ELECTRONICS
CAMBRIDGE, MASSACHUSETTS 02139

The Research Laboratory of Electronics is an interdepartmental laboratory in which faculty members and graduate students from numerous academic departments conduct research.

The research reported in this document was made possible in part by support extended the Massachusetts Institute of Technology, Research Laboratory of Electronics, by the JOINT SERVICES ELECTRONICS PROGRAMS (U.S. Army, U.S. Navy, and U.S. Air Force) under Contract No. DA 28-043-AMC-02536(E), and by the National Aeronautics and Space Administration (Grant NGL 22-009-013).

MASSACHUSETTS INSTITUTE OF TECHNOLOGY

RESEARCH LABORATORY OF ELECTRONICS

Technical Report 469

March 3, 1969

IMAGING OF OBJECTS VIEWED THROUGH A TURBULENT ATMOSPHERE

John C. Moldon

Submitted to the Department of Electrical Engineering, M.I.T., September 6, 1968, in partial fulfillment of the requirements for the degree of Doctor of Science.

(Manuscript received October 21, 1968)

Abstract

This report is concerned with estimating the high-resolution amplitude and phase parameters of the spatial Fourier transform of an object illuminated with incoherent radiation and viewed through a turbulent atmosphere.

The Cramer-Rao technique is employed to lower-bound the variance of any unbiased estimator, and receiver structures that approach these bounds are then exhibited. It is found that significant improvement over many existing systems is often possible, provided one is willing to pay for increased system complexity. The reduction of the processors to somewhat less efficient but more practically attractive forms is then considered.

Some experimental results are presented which illustrate the effects of turbulence on wave-front coherence.

TABLE OF CONTENTS

CONTENTS

I. INTRODUCTION

1.1 STATEMENT OF THE PROBLEM

It has long been recognized in astronomy that angular resolution is controlled primarily by the refractive index inhomogeneities in the atmospheric path. These inhomogeneities result from the continuous turbulent mixing of air from layers of differing temperature.

A wave that propagates through the atmosphere suffers random fluctuations in phase and amplitude. Thus the image formed by a telescope is diffused, thereby reducing the resolution of detail on the object. This problem, the bane of astronomers, is often referred to as "poor seeing". A familiar example of this phenomenon is the blurring and dancing of an object viewed through an optical path containing a source of strong local heating such as a radiator or roadway.

Even upon the best mountaintop locations, it is doubtful that wavefront coherence is maintained over a large enough area and for a long enough time for the full diffraction limited capabilities of large telescopes to be attained. These large apertures are of value mainly for energy gathering.

In many situations such as satellite surveillance one is even more constrained in the choice of observing location and time. Average apparent spreading of a point source is often from 1 to 6 seconds of arc (1 second of arc = 4.85 μrad). Daytime observations are usually the most severely affected.

In recent years, there has been a strong revival of interest in atmospheric optics, which is partly due to the development of laser communication systems. The resultant cross-fertilization of physical optics, system, and communication theory has given rise to the application of signal analysis and processing techniques to the imaging problem. This was the subject of a National Academy of Sciences study in the summer of 1966 at Woods Hole Oceanographic Institute, which stimulated the present research.[1]

Much of the contemporary work has dealt with improving the quality of images formed conventionally with a telescope and photographic recording. In previous applications, however, statistical communication theory has made its most significant impact when released from the narrow confines of a specified detection scheme, and allowed to seek instead the basic limitations of the problem within which all schemes must operate. Thus through such techniques as maximum-likelihood estimation, the best receiving structures can be found, and at times may be fundamentally different from the hitherto employed techniques. Also, once the basic performance constraints have been found, we are able to more objectively evaluate any receiving structure that may be contrived.

Our aim in this investigation was to determine the ultimate limits above which any estimate of the phase or amplitude of the spatial Fourier transform of the object must lie. Various receiving structures that approach these limits were found, discussed in terms of practical realization, and compared with existing techniques. For our purposes, the Fourier transform of the object is more convenient to consider than the

equivalent angular intensity function, since the factors limiting the resolution are more easily understood.

1.2 REVIEW OF THE PROBLEM

In order to acquaint the reader with the basic resolution problem, we shall review the theory of telescope imaging, particularly as resolution is affected by the atmospheric turbulence (see Fig. 1).

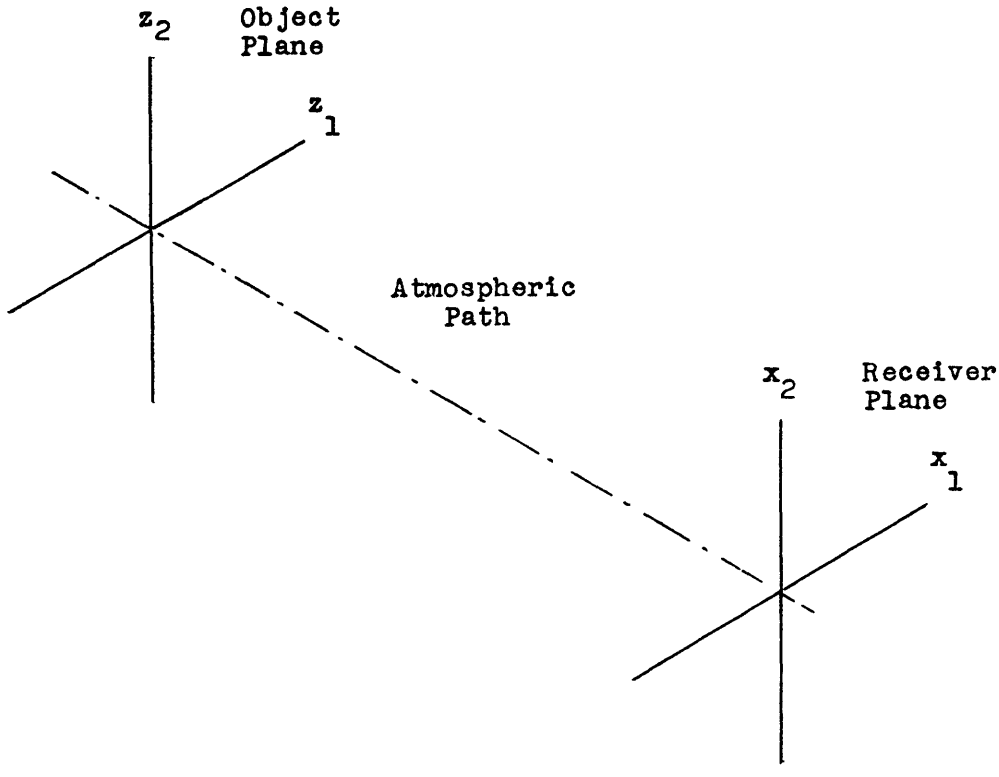

Fig. 1. Receiver geometry.

Points on the object are denoted by the angular coordinates $\underline{z} = (z_1, z_2)$, measured from the center of the receiving coordinates $\underline{x} = (x_1, x_2)$. The light radiated from the object is assumed to be noiselike. That is, similar to black-body radiation, which is (i) spatially incoherent across the object, each surface element radiating independently, and (ii) temporally incoherent, with a smoothly varying spectrum. Objects that are self-illuminated, as, for example, the sun and other stars, immediately justify this assumption. The model is also a reasonable description of most bodies that reflect light of natural origin. Indeed, even the illumination of a reasonably rough object by a multimode laser with bandwidth of a few megahertz can be considered.

The imaging equations simplify if we assume that the light is almost monochromatic, and describe the electric field as a narrow-band random process

$E(\underline{z}, t)\, e^{j2\pi ft}$, where $E(z,t)$ is the complex envelope, and f is the center frequency.

The spatial distribution of the average intensity of this radiation constitutes the pattern that is to be imaged. We assume that the object is stable or can be perfectly tracked, and describe its intensity by the function $\theta(\underline{z})$ which is proportional to $|\overline{E(\underline{z},t)}|^2$, where the bar is an ensemble average.

An equivalent description of the object, and one more responsive to resolution analysis, is the spatial Fourier transform

$$\Theta(\underline{k}) = \int_{\text{object}} d\underline{z}\ \theta(\underline{z})\ e^{-j2\pi \underline{z}\cdot\underline{k}} \tag{1}$$

The vector coordinates $\underline{k} = (k_1, k_2)$ are the two-dimensional spatial frequencies. By good angular resolution in an image, we mean a reconstruction, in which all spatial frequency components out to some desired limit appear in the picture within some acceptable tolerance.

1.2.1 Image Formation in the Free-Space Environment

In the absence of any turbulence, the complex envelope of the received field behaves as

$$E(\underline{x}, t) \propto \int_{\text{object}} E(\underline{z},t)\, e^{-j2\pi \underline{z}\cdot\underline{x}/\lambda}\, d\underline{z}, \tag{2}$$

where we have assumed (i) that the object is at sufficient distance relative to the aperture dimensions that a plane wave approximation is valid, and (ii) that the object subtends a small enough angle that $\sin z \approx z$.

If an aberration-free lens is placed in the aperture ($\underline{x}$ plane), the field appearing in the focal plane has the form

$$E(\underline{u}, t) \propto \int E(\underline{x},y)\, w(\underline{x})\, e^{-j2\pi \underline{x}\cdot\underline{u}/(\lambda L)}\, d\underline{x}, \tag{3}$$

where L is the focal length of the lens, and $w(\underline{x})$ is a transmittance function describing the shading of the lens (see Fig. 2).

A photograph, like most other detectors, responds to a time-averaged value of intensity, rather than to the instantaneous value of the incident field. This focal plane intensity we describe as

$$\begin{aligned} I(\underline{u}) &\propto \langle |E(\underline{u}, t)|^2 \rangle \\ &\propto \iint d\underline{x}d\underline{x}'\ w(\underline{x})\, \overset{*}{w}(\underline{x}')\, \langle E(\underline{x}, t)\overset{*}{E}(\underline{x}', t)\rangle\, e^{-j2\pi \underline{u}\cdot(\underline{x}-\underline{x}')/\lambda L}, \end{aligned} \tag{4}$$

where the result of the time averaging is denoted by angular brackets. In general, this

does not give a deterministic result because of the random nature of the original radiation. Practically, however, the bandwidth of even the most monochromatic natural light is many times greater than the detector bandwidth. This bandwidth is the reciprocal of

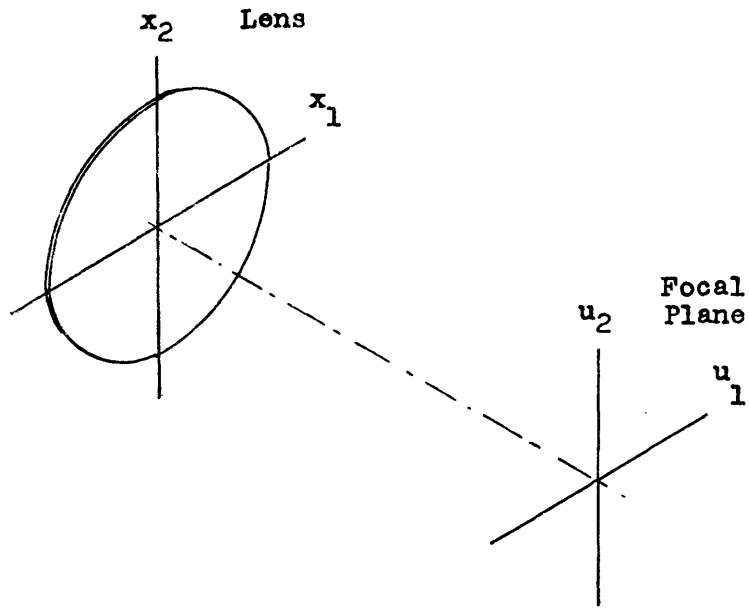

Fig. 2. Imaging with a lens.

exposure time for a photograph. Thus the output of the detector represents a sum of a large number of independent samples of the radiation process; hence, there is an overwhelming tendency for the sample average to approach the expectation of an ensemble of source radiation processes. The bracketed term in Eq. 4 is then closely approximated by the ensemble average mutual coherence function

$$\Gamma(\underline{x}, \underline{x}') = \overline{E(\underline{x}, t)\, \overset{*}{E}(\underline{x}', t)} \approx \langle E(\underline{x}, t) \overset{*}{E}(\underline{x}', t) \rangle. \tag{5}$$

When the object is spatially incoherent, with the aid of (1) and (2) we obtain the well-known result

$$\Gamma(\underline{x}, \underline{x}') \propto \Theta[(\underline{x}-\underline{x}')/\lambda]. \tag{6}$$

That is, the mutual coherence function of the received field is dependent only upon the displacement $\underline{x} - \underline{x}'$, and is simply proportional to the object Fourier transform evaluated at $\underline{k} = (\underline{x}-\underline{x}')/\lambda$.

The image formed by the telescope can now be obtained. Rather than study the pattern in the focal plane, however, it is more convenient to evaluate the image Fourier transform

$$\mathcal{I}(\underline{k}) = \int I(-\underline{u})\, e^{-j2\pi \underline{k} \cdot \underline{u}/L}\, d\underline{u}, \tag{7}$$

where the argument of I has a sign reversal to account for the familiar image inversion that occurs with a single lens. This image transform becomes simply

$$\mathscr{I}(\underline{k}) \propto \Theta(\underline{k}) \int d\underline{x}\, w(\underline{x})\, \overset{*}{w}(\underline{x}+\lambda\underline{k}). \tag{8}$$

1.2.2 Diffraction-Limited Modulation Transfer Function

Equation 8 shows that the spatial frequency components in the object and image are directly related by a function

$$H(\underline{k}) = \int d\underline{x}\, w(\underline{x})\, \overset{*}{w}(\underline{x}+\lambda\underline{k}), \tag{9}$$

which is commonly referred to as the modulation transfer function (MTF). Generally, aperture points are either completely transparent or opaque; the pupil function then has only two values, zero and one. $H(\underline{k})$ is then the area in the available aperture over which the mutual coherence function is integrated for a displacement $\lambda\underline{k}$. Equivalently, it is the common area between the aperture and a replica translated by $\lambda\underline{k}$ (see Fig. 3).

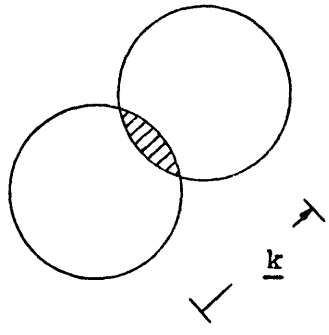

Fig. 3. Evaluation of $H(\underline{k})$.

The common circular aperture with diameter D has a radially symmetric MTF with the general shape indicated in Fig. 4. The upper limit of spatial frequencies appearing

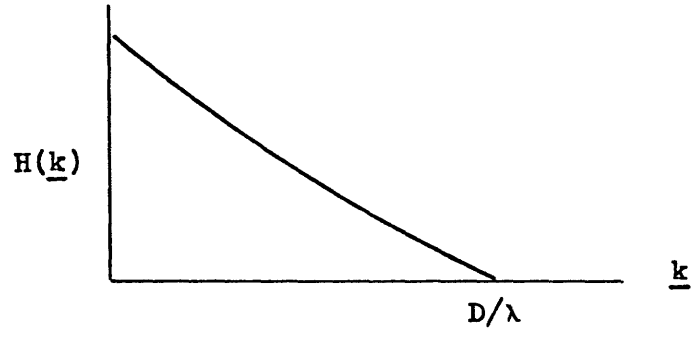

Fig. 4. MTF for circular aperture.

in the image is then D/λ. As an example, a 10-cm aperture operating in the middle of the visible spectrum (0.55 μ), has an upper resolution limit of 0.18 lines/μrad. This limit is commonly referred to as the diffraction limit of the system, since it is due to the fact that diffraction of light from the edges of the aperture diffuses the image.

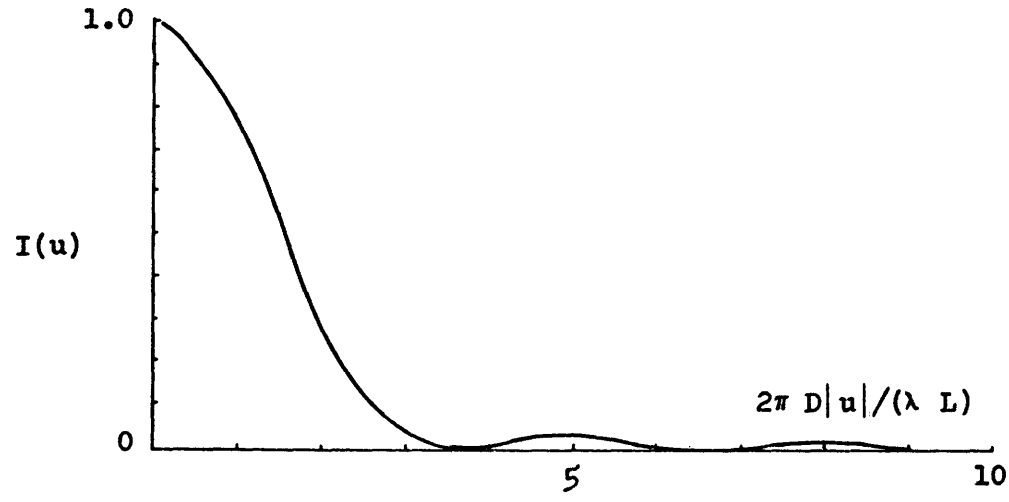

Fig. 5. Point-spread function.

In the focal plane itself, this diffraction effect transforms a point source (incident plane wave) into an Airy disk surrounded by fainter concentric rings. The general form of the intensity is sketched in Fig. 5, and is given precisely as

$$I(\underline{u}) = \left[\frac{J_1[2\pi D|\underline{u}|/(\lambda L)]}{\pi D|\underline{u}|/(\lambda L)}\right]^2 . \tag{10}$$

Arbitrary resolution criteria have been defined in terms of this point smearing. Rayleigh's criterion states that two point sources can be "resolved" when the center of the one disk is beyond the first null of the other. This requires that the points be separated by more than 0.61 λ/D rad (see Born and Wolf[2]).

Although such criteria are reasonable rules of thumb when it comes to visual observations, they are rather meaningless in a precise analysis, since they evade entirely the effects of background noise in the image. Indeed, if there is absolutely no noise in the image, the choice between the hypotheses of one or two sources can be perfectly resolved, regardless of the aperture size. In the language of the communication theorist, it is a singular detection problem.

It is absolutely necessary, then, in speaking of resolution to include the effects of the noise. In any recording device the induced noise is ultimately due to the basic quantum nature of the photodetection process. With a photograph the noise is associated with the individual grains that are developed. In the absence of reciprocity failures and other

nonlinear effects, the consequences of the noise can usually be made arbitrarily small by increasing the amount of light energy, either by increasing the area of the aperture or the exposure time. The diffraction-limited MTF will be maintained, however, only when the incoming wavefronts remain undisturbed.

1.2.3 Atmospheric Modulation Transfer Function

The effect of the atmosphere is to reduce the wavefront coherence to only a few centimeters. The time rate of change of these disturbances is usually measured in milliseconds. These atmospheric effects are commonly described by the introduction of a complex multiplicative process, $e^{a(\underline{x}, \underline{z}, t)+jb(\underline{x}, \underline{z}, t)}$, into each incident wave. The mutual coherence function of the received process is now not only dependent upon the displacement $\underline{x}-\underline{x}'$ but also upon the time t and point of origin $\underline{x}$ in the aperture.

Equation 6 for the mutual coherence function now becomes

$$\Gamma(\underline{x}, \underline{x}', t) \propto \int d\underline{z}\, \theta(\underline{z})\, e^{-j2\pi \underline{z}\cdot(\underline{x}-\underline{x}')/\lambda}\, e^{a(\underline{x}, \underline{z}, t)+a(\underline{x}', \underline{z}, t)+j[b(\underline{x}, \underline{z}, t)-b(\underline{x}', \underline{z}, t)]} \tag{11}$$

As a function of the displacement $\underline{x} - \underline{x}'$, Γ no longer has a one-to-one correspondence with the spatial frequency components in the object, since the angular variations in the disturbances induce a dispersion of spatial frequencies between object and image. The analysis is simplified, however, if we suppose that the object is small enough to be completely within an isoplanatic patch, that is, a region over which the wave disturbances are invariant with angle. Equation 11 then reduces to

$$\Gamma(\underline{x}, \underline{x}', t) \propto \Theta\left[\frac{\underline{x}-\underline{x}'}{\lambda}\right] e^{a(\underline{x}, t)+a(\underline{x}', t)+j[b(\underline{x}, t)-b(\underline{x}', t)]}. \tag{12}$$

Although there is now no dispersion of frequencies, the factor of proportionality between the mutual coherence function and the object transform is a random process, which we denote by

$$h(\underline{x}, \underline{x}', t) = e^{a(\underline{x}, t)+a(\underline{x}', t)+j[b(\underline{x}, t)-b(\underline{x}', t)]}. \tag{13}$$

In the focal plane of a telescope, the image is now a time-variant random process. In the Fourier transform domain it behaves as

$$\mathcal{I}(\underline{k}, t) \propto \int w(\underline{x})\, \overset{*}{w}(\underline{x}+\lambda\underline{k})\, \Gamma(\underline{x}, \underline{x}', t)\, d\underline{x} \propto \Theta(\underline{k}) \int w(\underline{x})\, \overset{*}{w}(\underline{x}+\lambda\underline{k})\, h(\underline{x}, \underline{x}+\lambda\underline{k}, t)\, d\underline{x}. \tag{14}$$

Thus there is a random MTF relating the object and image. When the aperture is large or the exposure time long, we expect that the sample MTF will approach the same value as an average over an ensemble of atmospheres. Under such an averaging, the effects of the aperture dimensions and the atmosphere are separable, and we have

$$\mathcal{I}(\underline{k}, t) \propto \Theta(\underline{k})\, H(\underline{k})\, H_A(\underline{k}), \tag{15}$$

where $H_A(\underline{k})$ is the average atmospheric MTF. This function has been estimated analytically in several ways. Hufnagel and Stanley[3] obtained an approximate solution of the wave equation that must be satisfied by the mutual coherence function as averaged over an ensemble of atmospheres. Fried[4] has used an approach that gives similar results, and this is the tack that we follow. Since Tatarski[5] and others have already shown that a and b behave as jointly Gaussian random processes, $h(\underline{x}, \underline{x}', t)$ can be averaged directly to give

$$H_A(\underline{k}) = \overline{h(\underline{x}, \underline{x}+\lambda\underline{k}, t)}$$

$$= e^{-1/2\,[D_a(|\lambda\underline{k}|)+D_b(|\lambda\underline{k}|)]}. \tag{16}$$

Both a and b are assumed locally stationary and homogeneous with structure functions

$$D_a(\underline{x}-\underline{x}') = \overline{[a(\underline{x}, t)-a(\underline{x}', t)]^2} \tag{17}$$

$$D_b(\underline{x}-\underline{x}') = \overline{[b(\underline{x}, t)-b(\underline{x}', t)]^2}. \tag{18}$$

The mean value of b is taken as zero but, in order to maintain conservation of energy

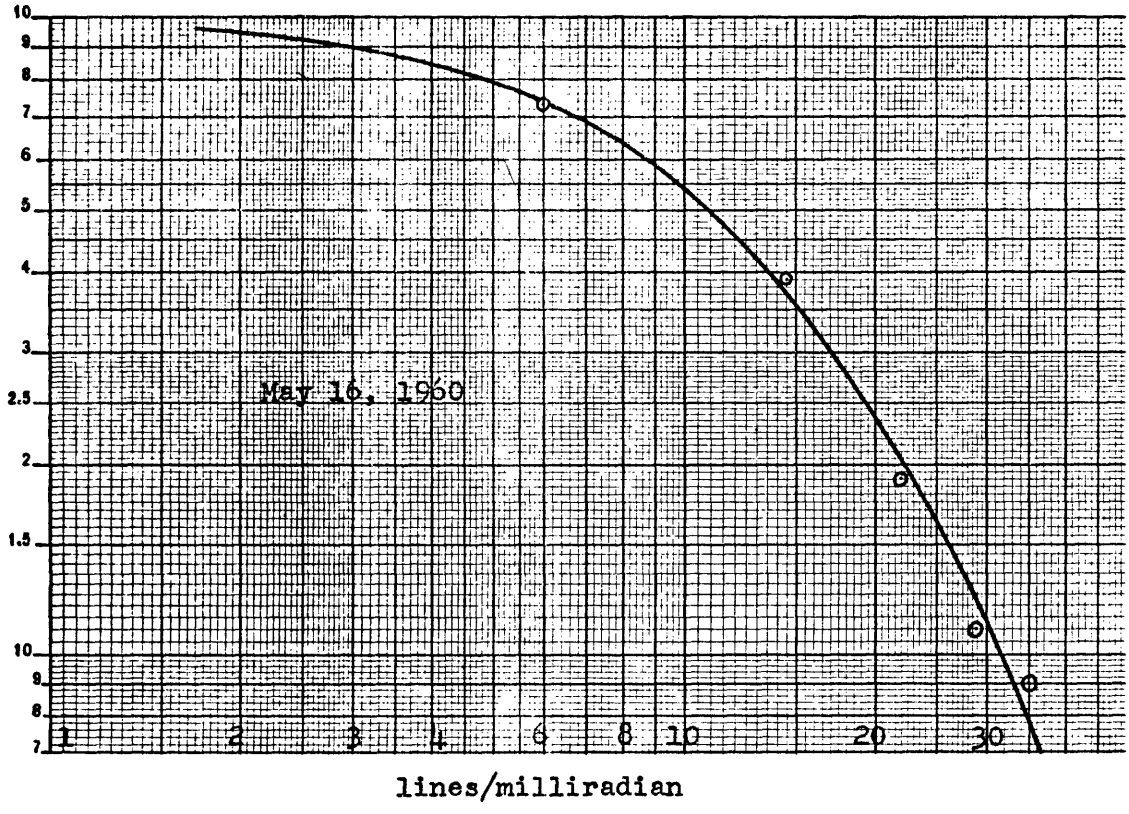

Fig. 6. Typical atmospheric MTF (Djurle and Back[6]).

regardless of the severity of the fading, the mean and variance of a are related by

$$\bar{a} = -\overline{[a-\bar{a}]^2}. \tag{19}$$

Because of the exponential behavior of (16), the attenuation is very strong once $|\lambda \underline{k}|$ exceeds the correlation distance. Djurle and Back[6] have made some measurements of atmospheric MTF which are representative of the image degradation to be expected. These results are reproduced in Fig. 6, and it can be seen that an attenuation of more than 20 dB (factor of 10 in H_A) is encountered for spatial frequencies greater than 0.03 lines/μrad. Recall that 0.03 lines/μrad is well within the diffraction limit of a 10-cm diameter aperture.

At larger values of displacement the attenuation is even greater, and is difficult to measure directly from a distorted image. In Section IV, some experimental results are presented in which it was found that a phase variance of 50 $(\text{rad})^2$ was common on a long horizontal path. Such a variance corresponds to an MTF attenuation of more than 200 dB.

1.2.4 Image Reconstruction by Linear Filtering

One way in which some of the detail in a photograph can be restored is through spatial frequency enhancement techniques. The image from a long-exposure photograph is Fourier-transformed, divided by the average MTF, and transformed back, into a high-quality picture. Harris[7] used such a technique to make distorted images more distinguishable. This technique is similar to that used for edge enhancement in restoring telemetered pictures. Its success in the atmospheric problem is rather limited, mainly because of the following considerations:

1. the ever-present background noise is enhanced, together with the signal and may tend to dominate the final picture
2. the enhancement ratio may even be more than the linear dynamic range of the original recording
3. the residual uncertainty between the sample averaged MTF and the ensemble value generates an additional error which will also be enhanced.

Helstrom[8] considered the optimizing of the linear filtering procedure in order to minimize the total mean-square error in the picture. This is the optimum filtering technique of Wiener and Lee[9] and requires a priori knowledge of the average spatial spectrum of the class of objects considered.

In many imaging problems an ensemble description is not justified and, indeed, when some a priori assumptions are fed to such an "optimum" processor, the tendency will be, especially when the noise is strong, for the estimate to be biased toward the one which the processor believes is most likely a priori. For such reasons, it does not appear that the high-resolution imaging problem is really too suitable for the Wiener technique.

1.2.5 Image Motion Tracking

Fried[4] and Heidbreder[10] determined the improvements that are realized when the random motion of the image is eliminated. Over small values of displacement, the phase structure is believed to depend upon the 5/3 power of the separation. With such a structure function, it can be shown that over small apertures, at least, the wavefront distortion is primarily a change in the local angle of arrival. This random wavefront tilting appears in the focal plane as a movement of the image. It is interesting to note that a 5/3 behavior is not far from a $6/3 = 2$ behavior, for which the distortion would be entirely wavefront tilting.

If this motion can be eliminated by tracking of the tilt, the resultant average MTF can show possible improvement of three times the resolution bandwidth over the uncompensated case. This resolution bandwidth is defined as the first moment, or center of gravity of the MTF.

This maximum improvement was found to occur when the aperture is stopped down to approximately 3 or 4 correlation diameters. For high spatial frequencies, which require considerably larger apertures just to overcome the diffraction limitations, the reduction in attenuation is unspectacular, image motion being only a small part of the total distortion. Moreover, the object must be bright enough to generate a reliable tracking signal.

1.3 OUTLINE OF THE REPORT

Our intention has been to bring a more fundamental communication theory approach to the problem of imaging in a turbulent environment.

The classical statistical estimation problem is first formulated in Section II where we suppose, at least conceptionally, that the incident electric field is the input to the signal processor. From this initial formulation we derive the sufficient statistics for the incident process. These are the numbers containing all of the information relevant to an estimation of the object, and those that a receiver should extract if it is to utilize all available information. The necessary measurements are found to be the mutual coherence process as appropriately sampled in optical frequency, time, position in the aperture, and displacement. Implicit in the sampling operation is a prior local integration of the coherence process over corresponding correlation regions of the above-mentioned variables. The sample averaging is then shown to give essentially the same result as an expectation over an ensemble of source radiation processes, the result of which is still dependent upon the instantaneous atmospheric disturbances. The physical measurement of mutual coherence then follows, and we explore various interferometer configurations of lenses, mirrors, etc. terminated with energy detectors. A model for the noise that must inevitably accompany the detection is then developed.

The ultimate performance limitations are the subject of Section III. With the aid of the Cramer-Rao inequality we are able to underbound the variance of any unbiased

estimate of either the phase or the amplitude of the spatial Fourier transform. Various processing structures that approach these bounds are then studied and compared with conventional techniques. We find that if the signal-to-noise ratio is very high, optimum estimation of the parameters is realized by tracking the phase and amplitude disturbances in the mutual coherence function. At lower values of signal-to-noise ratio, a reliable tracking signal cannot be obtained, and a square-law or crosscorrelation processing of the samples appears to be most favorable.

Finally, with extremely small signal levels it is found that a straight integration of the samples may be most advantageous. That is, the techniques of long-exposure recording should be employed, perhaps with a device other than a photograph for recording, because of effects of reciprocity failure and other nonlinearities. Finally, the various proposed processing structures are compared with techniques employed at the present time, including the Hanbury Brown and Twiss[11,12] intensity interferometry.

Some results of a parallel experimental investigation are presented in Section IV. Photographic and photoelectric measurements illustrate both qualitatively and quantitatively the major effects of the atmosphere as they affect image estimation.

Derivations that would have required more than a few lines in the main text are relegated to appendices.

Only the more recent journal articles are referenced in their original form. Much of the older source material has by this time been chewed over by many authors and been republished in more digestible forms. For this reason, we have referenced publications that are readily available and whose explanations are most suitable for our analysis. The reader interested in more source material will usually find that the cited authors have provided a plethora of references.

II. CHANNEL MODEL

We have given a rather abbreviated analysis of the general features of the problem of imaging through a turbulent atmosphere. This analysis was primarily directed toward the image degradation experienced with photographs taken through telescopes. We now want to develop a broader model for the problem, and to find the optimal set of field measurements that should be recorded and their statistical form. The study of optimum schemes of processing these measurements and the performance limitations will be considered in Section IV.

We shall begin with a classical approach to the estimation problem and consider the action of a statistically optimum receiver structure when it has complete specification of the incident electric field process. By this means, we are able to show that samples of the spatial mutual coherence properties of the field constitute a statistically sufficient set of measurements. The relationship of these measurements to the average field intensity pattern across the object will then be discussed. We shall then show that the local coherence measurements are related to the spatial Fourier transform of the object through a random multiplicative term attributable to the atmosphere and an additive shot-noise term introduced by the detector.

2.1 RECEIVED ELECTRIC FIELD

We imagine that the object and our receiving aperture are orientated as in Fig. 7. We model the object as an unknown distribution of point radiators, and restrict ourselves to that class of objects whose radiation is noiselike. This implies that the radiators are spatially and temporally incoherent. By these terms we mean that each element emits a statistically independent electric-field process with a smoothly varying spectrum. By smoothly varying we mean that significant changes do not occur on a scale of less than a few megahertz at least.

Objects that are self-illuminated immediately satisfy these conditions, since each atom is excited independently and decays with a time constant that is usually very short. Only when the radiators are coupled, as in a resonant laser cavity, must we be concerned with the temporal characteristics of the radiation.

When the object is a secondary scatterer, we must be somewhat more careful because if the illuminating light is either highly temporally or spatially coherent, the light received from the object may still carry some of these properties. Often, however, when the surface of the object is rough and has some vibrational motion, these coherence properties are destroyed. What we must exclude from our model are such phenomena as the "grainy" pattern sometimes observed on an object illuminated by a laser beam.

The function that is of interest to us and constitutes the picture of the object is the average intensity profile which we denote $\theta_\nu(\underline{z})$, where the subscript ν allows for a possible frequency dependence of the radiation. An equivalent description of the object,

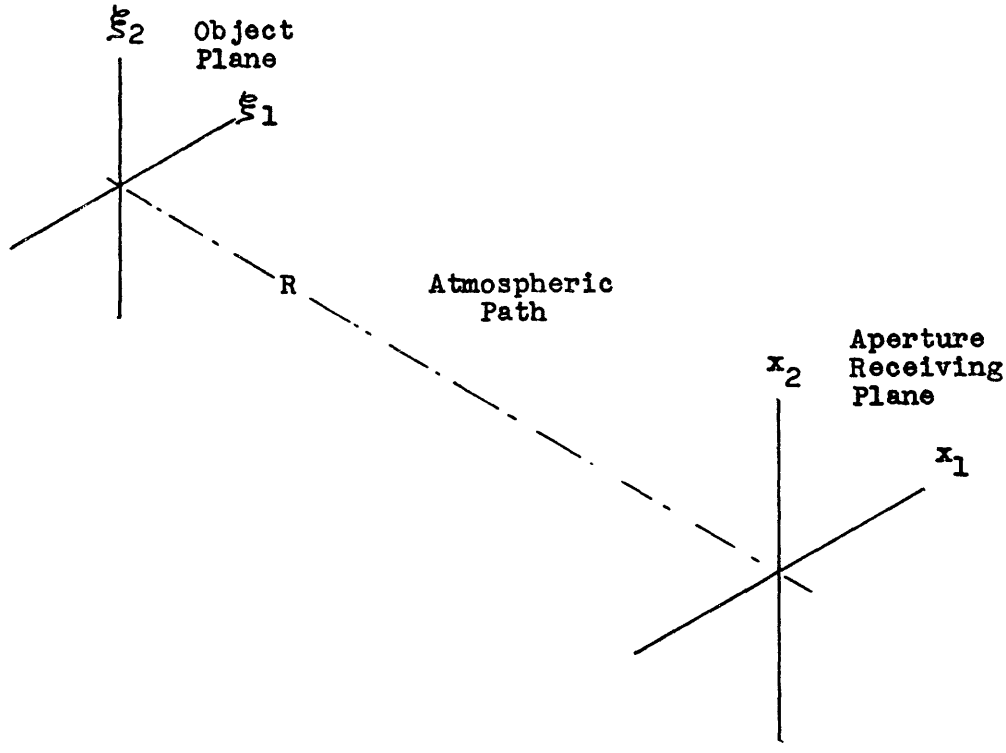

Fig. 7. Problem geometry.

and one that is often more responsive to resolution analysis is the spatial Fourier transform, which we denote $\Theta_v(\underline{k})$, where the vector $\underline{k}$ represents the two-dimensional spatial frequencies.

The electric field radiated from the object is modelled as a Gaussian (normal) random process. This process is most conveniently described with a Fourier series representation. We first subdivide the entire observation time interval T into segments of length ΔT, where ΔT is the correlation time of the atmospheric disturbances. That is, we can consider the disturbances as constant over such a period. Over the l^{th} such interval the field emitted from point p on the object is expressed as a sum of frequency components as

$$E_p(t) = \frac{1}{\Delta T^{1/2}} \sum_{m=0}^{\infty} \rho_{p,l,m}\, e^{-j2\pi mt/\Delta T}$$

$$l\,\Delta T \leq t < (l+1)\Delta T, \tag{20}$$

where the complex random coefficients are given as

$$\rho_{p,l,m} = \frac{1}{\Delta T^{1/2}} \int_{l\,\Delta T}^{(l+1)\Delta T} E_p(t)\, e^{+j2\pi mt/\Delta T}\, dt. \tag{21}$$

Only those frequencies $v = m/\Delta T$ that fall within the optical spectral range of the object give significant contributions to Eq. 20. We assume that the field strength $E_p(t)$ is referenced to unit distance from the element. In the absence of an inhomogeneous atmosphere, the corresponding complex representation of the field received over the aperture coordinates $\underline{x} = (x_1, x_2)$ is

$$E_{l,m}(x) = \sum_p \frac{\rho_{p,l,m}}{R} e^{-j2\pi \underline{\xi} \cdot \underline{x}/(\lambda R)}, \tag{22}$$

where $\underline{\xi} = (\xi_1, \xi_2)$ are the coordinates of the point p, and λ is the wavelength associated with frequency v.

Two simplifications are implicit in arriving at (22). First, we have assumed that the aperture is sufficiently small compared with the radius R of the incident spherical wave, so that a plane wave approximation is valid. Second, we have ignored the average propagation delay, since only the relative delay over the aperture is of importance.

When turbulence is present, we follow the lead of Tatarski[5] and others and introduce a random amplitude and phase term of the form

$$e^{a_v(\underline{x}, \underline{\xi}, t)+jb_v(\underline{x}, \underline{\xi}, t)}. \tag{23}$$

Theoretical and experimental results strongly suggest that both a and b are well modelled as Gaussian random processes. The results here do not require this Gaussian hypothesis, and only the correlation scales are needed. The correlation times typically have been found to be of the order of 1 msec or more with a spatial scale of, perhaps, a few centimeters. The strength of the fading is described by the variance of a, which has been found to be as much as one at times. The variance of the phase process is often extremely large, but in our work the absolute phase is unimportant. Rather the phase difference between aperture points is of more significance, and has been observed to vary many radians. This spatial phase incoherence is the most troublesome as far as imaging is concerned, but, as we shall see, the amplitude disturbances also play an important role in the performance of estimator structures.

The description of the received field is not complete without including some background noise. This may be sunlight, moonlight, and so forth scattered from particles in the air. We simply represent it as an additional Gaussian component $n_{l,m}(\underline{x})$ in the received field.

With the effects of the atmosphere and the noise included, (22) now becomes

$$E_{l,m}(\underline{x}) = \sum_p \frac{\rho_{p,l,m}}{R} e^{-j2\pi \underline{\xi} \cdot \underline{x}/(\lambda R)} e^{a_v(\underline{x}, \underline{\xi}, t)+jb_v(\underline{x}, \underline{\xi}, t)} + n_{l,m}(\underline{x}). \tag{24}$$

2.2 SUFFICIENT FIELD MEASUREMENTS

The functions $E_{l,m}(\underline{x})$, though a complete representation of the received random process, cannot be practically measured if for no other reason than that it would require so many functions to represent the process over any reasonable interval. We now seek a simpler set of measurements that still retain all of the information relevant to the intensity pattern on the object. We continue to treat the problem classically and ask what a statistically optimum processor would do with the functions $E_{l,m}(\underline{x})$ if it actually had them available. Such a receiver extracts all of the relevant information, by calculating a measure of the probability of the received process conditioned on all acceptable hypotheses. This conditional probability is very difficult to express directly, since the processes $E_{l,m}(\underline{x})$ are products of normal and log-normal forms. We circumvent this difficulty by conditioning the probability function on the atmospheric processes a and b, as well as on the unknown object pattern θ. The processes $E_{l,m}(\underline{x})$ are then Gaussian under the additional condition, and the probability function is well known. The conditioning on the atmosphere can be removed by averaging the result over a and b; however, this last operation is unnecessary in the determination of the simpler yet sufficient measurements.

As we have mentioned, the spectra of our objects are smoothly varying on a scale of at least many megahertz. Thus when we choose ΔT as 1 msec or so we expect the set of spatial random processes $E_{l,m}(\underline{x})$ to be independent in the disjoint time intervals l and orthogonal frequencies m. The probability of the entire set of processes is then simply a product of probabilities of each term taken separately.

Before we can express the probability of a particular sample function we must reduce to a random-variable representation. Such a representation is most conveniently obtained with a Karhunen-Loève expansion (see Van Trees[13]). We first require the spatial correlation properties of the received process. These properties are completely contained in the two complex correlation functions

$$\Gamma_{l,m}(\underline{x},\underline{x}') = \overline{E_{l,m}(\underline{x})\, E^{*}_{l,m}(\underline{x}')} \tag{25}$$

$$\tilde{\Gamma}_{l,m}(\underline{x},\underline{x}') = \overline{E_{l,m}(\underline{x})\, E_{l,m}(\underline{x}')}. \tag{26}$$

Under the natural assumption that the complex coefficients describing the object and noise radiation have uniformly distributed phases, (26) is identically zero. Also, the real and imaginary components of each sample function turn out to be uncorrelated. Each of these components then has the same correlation function

$$R_{l,m}(\underline{x},\underline{x}') = \overline{\mathrm{Re}\,[E_{l,m}(\underline{x})]\,\mathrm{Re}\,[E_{l,m}(\underline{x}')]} = \overline{\mathrm{Im}\,[E_{l,m}(\underline{x})]\,\mathrm{Im}\,[E_{l,m}(\underline{x}')]}$$

$$= \frac{1}{2}\,\mathrm{Re}\,[\Gamma_{l,m}(\underline{x},\underline{x}')]. \tag{27}$$

The processes $E_{l,m}(\underline{x})$ are now expanded in the orthogonal series

$$E_{l,m}(\underline{x}) = \sum_{n=1}^{\infty} E_{l,m,n}\psi_{l,m,n}(\underline{x}), \tag{28}$$

where the $\psi_{l,m,n}(x)$ are real functions that have been chosen as the orthonormal eigenfunctions of the equation

$$c_{l,m,n}\psi_{l,m,n}(\underline{x}) = \int_{\text{aperture}} \psi_{l,m,n}(\underline{x}')\, R_{l,m}(\underline{x}, \underline{x}')\, d\underline{x}'. \tag{29}$$

The coefficients in the expansion (29) are determined by

$$E_{l,m,n} = \int_{\text{aperture}} E_{l,m}(\underline{x})\, \psi_{l,m,n}(\underline{x})\, dx. \tag{30}$$

These coefficients have independent zero-mean real and imaginary components, each with a variance $c_{l,m,n}$, the corresponding eigenvalue of (29).

If we approximate (28) with the first N terms, the conditional probability then is

$$p(E_{l,m}(\underline{x})/\theta, a, b) \approx \frac{\exp\left[-\sum_{n=1}^{N} |E_{l,m,n}|^2/(2c_{l,m,n})\right]}{(2\pi)^N} \tag{31}$$

Multiplying the results for all time intervals and frequencies, taking the logarithm, and retaining only the part that is dependent upon the electric field leaves

$$\sum_{l=0}^{T/\Delta T} \sum_{m=0}^{\infty} \sum_{n=1}^{\infty} |E_{l,m,n}|^2/(2c_{l,m,n}), \tag{32}$$

where the summation on n has now been extended to $+\infty$. This triple summation (32) is then the operation that an optimal receiver would perform on the electric field, but the receiver is required to know the $c_{l,m,n}$ for each possible hypothesis concerning θ, a, and b.

The determination of a sufficient set of measurements comes, as we now show that the summations in (32) can be reduced considerably even with θ, a, and b unknown.

We first rewrite (32) as

$$\int d\underline{x} \int d\underline{x}' \sum_{l=0}^{T/\Delta T} \sum_{m=0}^{\infty} E_{l,m}(\underline{x})\, \overset{*}{E}_{l,m}(\underline{x}')\, Q_{l,m}(\underline{x}, \underline{x}'), \tag{33}$$

where

$$Q_{l,m}(\underline{x},\underline{x}') = \sum_{n=1}^{\infty} \frac{\psi_{l,m,n}(\underline{x})\,\psi_{l,m,n}(\underline{x}')}{2c_{l,m,n}} \tag{34}$$

is the inverse kernel of the correlation function $R_{l,m}(\underline{x},\underline{x}')$.

Now we can safely assume that over some range of the frequency index m, the kernel Q will remain virtually unchanged. We then rewrite the summation on m in (33) as

$$\sum_{m=0}^{\infty}(\ ) = \sum_{q=0}^{\infty} Q_{l,Mq}(\underline{x},\underline{x}') \sum_{m=Mq}^{M(q+1)-1} E_{l,m}(\underline{x})\,\overset{*}{E}_{l,m}(\underline{x}'), \tag{35}$$

and with the aid of Parseval's theorem we find that expression (33) is proportional to

$$\int d\underline{x} \int d\underline{x}' \sum_{l=0}^{T/\Delta T} \sum_{q=0}^{\infty} Q_{l,Mq}(\underline{x},\underline{x}') \int_{l\Delta T}^{(l+1)\Delta T} E_{v}(\underline{x},t)\,\overset{*}{E}_{v}(\underline{x}',t)\,dt. \tag{36}$$

The term $E_v(\underline{x},t)$ in expression (36) is just the narrow-band field process resulting from the M Fourier frequency components, and can be obtained by bandpass-filtering the incident field between frequencies $Mq/\Delta T$ and $M(q+1)/\Delta T$, $v \approx Mq/\Delta T$.

The integration in (36) is then simply a sample time average of the coherence between the fields at points $\underline{x}$ and $\underline{x}'$ within the optical band about frequency v. This average is commonly referred to as the mutual-coherence process. We use the word process rather than function to denote that it is still a local sample average, rather than an ensemble average.

The number of terms M that can be brought within the partial sum of (35) is an important parameter of the measurement, as it sets the optical bandwidths of the set of filters that the receiver should employ. This bandwidth we denote

$$\Delta v = M/\Delta T. \tag{37}$$

We can estimate the width of this band by considering the correlation function

$$\Gamma_{l,m}(\underline{x},\underline{x}') = \overline{E_{l,m}(\underline{x})\,\overset{*}{E}_{l,m}(\underline{x}')}$$

$$= \sum_{p} \frac{\overline{|\rho_{p,l,m}|^2}}{R^2}\, e^{-j2\pi\underline{\xi}\cdot(\underline{x}-\underline{x}')/(\lambda R)}\, h_v(\underline{x},\underline{x}',\underline{\xi},t) + \overline{n_{l,m}(\underline{x})\,n_{l,m}(\underline{x}')}, \tag{38}$$

where h is the atmospheric function defined as

$$h_v(\underline{x}, \underline{x}', \underline{\xi}, t) = e^{a_v(\underline{x}, \underline{\xi}, t)+a_v(\underline{x}', \underline{\xi}, t)+j[b_v(\underline{x}, \underline{\xi}, t)-b_v(\underline{x}', \underline{\xi}, t)]}. \tag{39}$$

The dependence upon m in the terms $\overline{|\rho_{p,l,m}|^2}$ and $\overline{n_{l,m}(\underline{x})\, n_{l,m}(\underline{x}')}$ describes the spectral behavior of the object and noise background. We shall suppose that these are sufficiently wideband that the limit on Δv is due to the behavior of the terms

$$e^{-j2\pi\underline{\xi}\cdot(\underline{x}-\underline{x}')/(\lambda R)} \tag{40}$$

and

$$h_v(\underline{x}, \underline{x}', \underline{\xi}, t). \tag{41}$$

To see the general order of Δv to be encountered, consider the following example:

1. maximum field of view

   $|\underline{\xi}|_{max}/R = 100\ \mu rad$ ($\approx$25 seconds of arc)

2. maximum aperture displacement

   $|\underline{x}-\underline{x}'| = 1$ meter.

We find that the phase angle associated with (40) changes only about 1 rad when the frequency is swept over some 0.5×10^{12} Hz. In terms of wavelength bandwidth this is almost 50 Å for light near the middle of the visible spectrum.

The optical correlation bandwidth of the term (41) is also significant in determining the allowable Δv. Very little experimental work has been reported on the frequency dependence of a and b, but we can still get a rough estimate with a ray theory argument. Under the assumption that the index of refraction of the air itself is constant over the small optical bands of interest, the ray analysis predicts an attenuation term a independent of frequency, and a phase that is linearly related to frequency. Thus if at one particular frequency the phase difference between aperture points is 10 rad, a frequency 10% higher would show a corresponding phase difference of 11 rad. Admittedly, a ray analysis is weak on a long path, diffraction effects being important. Nevertheless, we can still convince ourselves that the optical correlation bandwidth Δv is of the same general order as that predicted in the previous paragraph.

Although interpretation of expression (36) gives the general form of the sufficient measurements, namely time and frequency sampled coherence measurements, we still seek some additional reduction. Rather than have to measure this coherence process for all continuous pairs of points $\underline{x}$ and $\underline{x}'$, we want to get a spatial sampled measurement. Showing that this reduction is possible requires demonstrating that the kernel Q has characteristic scale dimensions $\underline{x}$ and $\underline{x}'$ over which there is little significant change.

This is most easily demonstrated if we look at a special case. Let us suppose that

the background noise power is high compared with the signal, and that the noise correlation function is impulsive in the displacement variable $\underline{x}-\underline{x}'$, or at least has a correlation scale shorter than that of the field from the object. As we shall see, this essentially means that the noise power appears evenly distributed over a region of the sky larger than that subtended by the object. Under these conditions, we can invoke the CUP results (Coherently Unestimable Parameters – see Van Trees[13]). We are able to approximate the kernel

$$Q_{l,m}(\underline{x},\underline{x}') \approx \frac{1}{N_m}\mu_o(\underline{x}-\underline{x}') - \left[\frac{1}{N_m}\right]^2 R_{l,m}(\underline{x},\underline{x}'), \tag{42}$$

where we have supposed that for the stationary noise process

$$\overline{n_{l,m}(\underline{x})\, n_{l,m}(\underline{x}')} = N_m \mu_o(\underline{x}-\underline{x}'). \tag{43}$$

Expression (17) then reduces to

$$\sum_{l=0}^{T/\Delta T}\sum_{q=0}^{\infty}\left[\begin{array}{l} \dfrac{1}{N_{Mq}}\displaystyle\int dx \int_{t=l\Delta T}^{(l+1)\Delta T} |E_v(\underline{x},t)|^2\, dt \\ \\ \dfrac{-1}{N_{Mq}^2}\displaystyle\int dx \int dx'\, R_{l,Mq}(\underline{x},\underline{x}') \int_{t=l\Delta T}^{(l+1)\Delta T} E_v(\underline{x},t)\, \overset{*}{E}_v(\underline{x}',t)\, dt \end{array}\right] \tag{44}$$

The first term in (44) is simply a measure of the total incident flux in each band, and is an almost trivial measurement. In the second term the kernel is now the correlation function whose dependence upon $\underline{x}$ and $\underline{x}'$ is known in terms of the atmospheric function h. Consider then just the integral part of the second term of (44). Changing variables so that $x' = \underline{x} + \underline{y}$, we can rewrite it

$$\int d\underline{y} \int d\underline{x}\, R_{l,Mq}(\underline{x},\underline{x}+\underline{y}) \int_{t=l\Delta T}^{(l+1)\Delta T} E_v(\underline{x},t)\, \overset{*}{E}_v(\underline{x}+\underline{y},t)\, dt. \tag{45}$$

Suppose now that we divide up the aperture into cells, each of side Δx, where Δx is the $\underline{x}$ correlation scale of the atmospheric function h. Numbering these cells with the index r = 1, 2 . . . , we can then rewrite (45) as

$$\int d\underline{y} \sum_r R_{l,Mq}(\underline{x}_r,\underline{x}_r+\underline{y}) \int_{r^{th}\ cell} d\underline{x} \int_{t=l\Delta T}^{(l+1)\Delta T} E_v(\underline{x},t)\, \overset{*}{E}_v(\underline{x}+\underline{y},t)\, dt. \tag{46}$$

Thus we find that sufficient measurements can be obtained by a local integration of the mutual coherence in both time and aperture space.

We still have the displacement variable $\underline{y}$ which can also be quantized. We can see from Eqs. 36 and 39 that the dependence upon $\underline{y}$ is in the atmospheric function h and the term

$$e^{-j2\pi\underline{\xi}\cdot(\underline{x}-\underline{x}')/(\lambda R)} = e^{+j2\pi\underline{y}\cdot\underline{\xi}/(\lambda R)}. \tag{47}$$

The correlation scale for $\underline{y}$ in the atmospheric function is the same as for the $\underline{x}$ variable. It is usually the second function (47) which sets the quantization scale of $\underline{y}$ for reducing (46) further, and it is the field of view subtended by the object that is the determining factor. We require that the exponent term $2\pi\underline{y}\cdot\underline{\xi}/(\lambda R)$ change less than approximately 1 rad over the local integration on $\underline{y}$. Indeed, the operation of integrating the displacement variable over a $\Delta y \times \Delta y$ region is really equivalent to restricting the field of view of the receiver to a solid angle of

$$\Omega = \lambda^2/\Delta y^2. \tag{48}$$

This can be thought of as spatial filtering to suppress background noise.

In summary, a statistically sufficient set of data can be obtained by local measurement of the mutual coherence process denoted

$$\hat{\Gamma}_v(\underline{x}, \underline{x}+\underline{y}, t) = \langle E_v(\underline{x}, t)\, \overset{*}{E}_v(\underline{x}+\underline{y}, t)\rangle, \tag{49}$$

where the angular brackets represent the local integrations in

1. time over the correlation time ΔT
2. frequency over the correlated optical bandwidth Δv
3. position over the correlation region Δx^2
4. displacement over the region $\Delta y^2 = \lambda^2/\Omega$.

A further point should be mentioned before passing to the next topic. Throughout the foregoing analysis we treated the electric field as a scalar quantity. Saleh[14] has shown that the atmosphere introduces no significant depolarization effects. If the intensity of the emitted radiation is the same for both polarization components, and these components are uncorrelated (uniform polarization angle), the mutual-coherence samples for each component should just be added together to form the sufficient measurements.

2.3 BEHAVIOR OF SAMPLED MUTUAL-COHERENCE PROCESS

We now want to consider the statistical properties of the measurements defined by Eq. 30. There are basically three random phenomena reflected in the data:

1. the radiation processes (both object and background)
2. the atmospheric turbulence
3. the noise disturbances introduced by the detector.

The first of these phenomena is most easy to treat in the optical case and, in fact, is almost negligible compared with the other two. This is because the large number of essentially independent samples of the process entering into each sample integration lets us substitute the ensemble average as the result.

2.3.1 Ensemble-Average Mutual-Coherence Process

If we average over the entire ensemble of object and background radiation processes, the average data samples are proportional to the correlation result of (38), where we still treat the atmospheric disturbances as parameters rather than random processes,

$$\overline{\hat{\Gamma}_v(\underline{x}, \underline{x}+\underline{y}, t)} \propto \Gamma_{l,m}(\underline{x}, \underline{x}+\underline{y})$$

$$\propto \sum_p \frac{\overline{|\rho_{p,l,m}|^2}}{R^2} e^{-j2\pi \underline{\xi} \cdot \underline{y}/(\lambda R)} \overline{h_v(\underline{x}, \underline{x}+\underline{y}, \underline{\xi}, t) + n_{l,m}(\underline{x})\, \overset{*}{n}_{l,m}(\underline{x}+\underline{y})}, \qquad (50)$$

where

$\underline{\xi}$ is the location of object point p

l is the time index

m is the frequency index

v is the frequency = $m/\Delta T$

λ is the wavelength = velocity of light/v

h is the atmospheric disturbance (Eq. 20)

$n_{l,m}$ is the background noise process

$\overline{|\rho_{p,l,m}|^2}$ is proportional to the average energy radiated from the object (for simplicity, we suppress the factor $\epsilon_0/4$ which really relates the energy to the mean-square value of field coefficients).

Representing the object as a spatially continuous collection of radiators allows us to replace the summation in (50) by an integral

$$\sum_p \frac{\overline{|\rho_{p,l,m}|^2}}{R^2} (\ ) = \int \frac{d\underline{\xi}}{R^2} \tilde{\theta}_m(\underline{\xi})(\ ), \qquad (51)$$

where $\tilde{\theta}_m(\underline{\xi})$ is the average energy flux received on the m^{th} frequency during a ΔT time interval from an area $d\underline{\xi} = d\xi_1 d\xi_2$ on the object. Time dependence (subscript l), has been dropped in $\tilde{\theta}$, since we take for granted that the pattern on the object is stationary.

We now replace the linear coordinates by angular variables

$$z_1 = \frac{\xi_1}{R} \qquad (52)$$

and

$$z_2 = \frac{\xi_2}{R} \quad . \tag{53}$$

It is assumed that the object is of small enough angular size that sin $z \approx z$. Expression (50) can now be written

$$\overline{\hat{\Gamma}_v(\underline{x}, \underline{x}+\underline{y}, t)} \propto \int d\underline{z}\ \theta_v(z)\ e^{+j2\pi \underline{z} \cdot \underline{y}/\lambda}\ h_v(\underline{x}, \underline{x}+\underline{y}, z, t) + \overline{n_{l,m}(\underline{x})\ \overset{*}{n}_{l,m}(\underline{x}+\underline{y})}. \tag{54}$$

$\theta_v(z)$ is now proportional to the energy per solid angle and has the units: watts/(unit bandwidth), (unit solid angle), (unit area on aperture).

If we consider, for a moment, the special case of a free-space environment (h = 1), expression (54) reduces to simply

$$\overline{\hat{\Gamma}_v(\underline{x}, \underline{x}+\underline{y}, t)} \propto \Theta_v(-\underline{y}/\lambda) + \overline{n_{l,m}(\underline{x})\ \overset{*}{n}_{l,m}(\underline{x}+\underline{y})}, \tag{55}$$

where Θ is the spatial Fourier transform of the object defined as

$$\Theta_v(\underline{k}) = \int d\underline{z}\ \theta_v(\underline{z})\ e^{-j2\pi \underline{z} \cdot \underline{k}}. \tag{56}$$

We can look at the background-noise process as being due to a continuous distribution of radiators on a shell centered on the aperture. If we denote this distribution by the function $N_v(\underline{z})$, assuming that the received noise is both stationary and homogeneous, the spatial correlation then follows from analogy with (55) and (56) as

$$\overline{n_{l,m}(\underline{x})\ \overset{*}{n}_{l,m}(\underline{x}+\underline{y})} = \int d\underline{z}\ N_v(z)\ e^{+j2\pi \underline{z} \cdot \underline{y}/\lambda}. \tag{57}$$

Because of the filtering operation in the receiver structure (local integration on $\underline{y}$ restricting the field of view), we need only be concerned with the nature of $N_v(z)$ in the neighborhood of the object. Usually the noise will appear uniform over a reasonably large area, and we can simply denote the spectral flux density of the noise radiation as N_v watts/(unit bandwidth), (unit solid angle), (unit area on aperture).

The ensemble average value of our measurements, which contain a local integration on t, v, $\underline{x}$, and $\underline{y}$ becomes

$$\overline{\hat{\Gamma}_v(\underline{x},\underline{x}+\underline{y},t)} \propto \Delta T\ \Delta v\ \Delta x^2\ \Delta y^2 \int d\underline{z}\ \theta_v(\underline{z})\ e^{+j2\pi \underline{z} \cdot \underline{y}/\lambda}\ h_v(\underline{x}, \underline{x}+\underline{y}, \underline{\xi}, t) + \Delta T\ \Delta v\ \Delta x^2\ \lambda^2\ N_v \delta_{O,y}. \tag{58}$$

The delta function $\delta_{O,\underline{y}}$ is used to show that the noise contributes to the correlation only at zero displacement. For all other discrete sample points of $\underline{y}$ the noise field gives no correlation.

In evaluating the $\underline{y}$ integration on the background noise term (38) we assumed that the noise power was uniform over a region considerably larger than that subtended by the object. If we divide expression (58) by Δy^2, replacing $\lambda^2/\Delta y^2$ by the field of view Ω, we get the somewhat more agreeable form

$$\overline{\hat{\Gamma}_v(\underline{x}, \underline{x}+\underline{y}, t)} \propto$$

$$\Delta T\ \Delta v\ \Delta x^2 \left[\int d\underline{z}\ \theta_v(\underline{z})\ e^{+j2\pi \underline{z}\cdot\underline{y}/\lambda}\ h_v(\underline{x}, \underline{x}+\underline{y}, z, t) \right.$$

$$\left. + N_v\ \Omega\ \delta_{O,\underline{y}} \right] \tag{59}$$

When there is no atmospheric turbulence, the first term in Eq. 59 reduces simply to the Fourier transform of the object evaluated at spatial frequency $(\underline{k}) = -\underline{y}/\lambda$. In general, when turbulence is present, the angular variations in the atmospheric function h induce a dispersion of spatial frequencies; that is, there is no longer a one-to-one correspondence between spatial frequencies on the object and mutual coherence measurements on the receiving aperture. We simplify our analysis considerably, however, by restricting ourselves to those cases in which the angular dimensions of the object are less than the correlation angle of the disturbances. In section 2.3.3 we shall consider the possible applicability of the isoplanatic results to the more general case.

In this isoplanatic case the function h is independent of $\underline{z}$, and we then have

$$\overline{\hat{\Gamma}_v(\underline{x}, \underline{x}+\underline{y}, t)} \propto \Delta v\ \Delta T\ \Delta x^2\ \Theta_v(-\underline{y})\ h_v(\underline{x}, \underline{x}+\underline{y}, t) + \Delta v\ \Delta T\ \Delta x^2\ N_v\ \Omega\ \delta_{O,\underline{y}}, \tag{60}$$

where

$$h_v(\underline{x}, \underline{x}+\underline{y}, t) = e^{a_v(\underline{x}, t)+a_v(\underline{x}+\underline{y}, t)+j\left[b_v(\underline{x}, t) - b_v(\underline{x}+\underline{y}, t)\right]}. \tag{61}$$

We again have a one-to-one correspondence between the Fourier transform Θ and the average mutual coherence, but the multiplying factor h is a random process that prevents us from obtaining Θ easily from single measurements of $\hat{\Gamma}$.

The effect of the background noise, since we have assumed that it has uniform intensity across the field of view, is simply to raise the zero displacement value of $\hat{\Gamma}$ above the $\Theta(O)$ value. We can think of the background radiation as simply an intensity bias to the object pattern.

2.3.2 Convergence of Sampled Mutual-Coherence Process to Ensemble-Average Value

The foregoing analysis has all been concerned with the ensemble average value of the mutual-coherence process. We now want to show that, with high probability, the sample average that we obtain by integrating over the channel coherence time ΔT yields essentially the same result as the ensemble average. By ensemble average we mean an average over only the random fluctuations in the emission process; we still have dependence upon the phase and amplitude disturbances introduced by the atmosphere.

The convergence of the sample average is demonstrated by the mean-square error $\overline{|\epsilon|^2}$ defined as

$$\overline{|\epsilon|^2} = \overline{\left|\hat{\Gamma}_v(\underline{x}, \underline{x}', t) - \overline{\hat{\Gamma}_v(\underline{x}, \underline{x}', t)}\right|^2}. \tag{62}$$

This turns out to be (see Appendix A)

$$\overline{|\epsilon|^2} = \Delta T\, \Delta v\, \Delta x^4 \left[\Theta_v(0)\, e^{2a_v(\underline{x}, t)} + N_v\, \Omega\right]\left[\Theta_v(0)\, e^{2a_v(\underline{x}', t)} + N_v\, \Omega\right]. \tag{63}$$

If we normalize this error by dividing by the mean-square value of the mutual coherence measurement, we obtain

$$\frac{|\epsilon|^2}{\left|\hat{\Gamma}_v(\underline{x}, \underline{x}', t)\right|^2} = \frac{1}{\Delta T\, \Delta v} \frac{\left[\Theta_v(0)\, e^{2a_v(\underline{x}, t)} + N_v\, \Omega\right]\left[\Theta_v(0)\, e^{2a_v(\underline{x}', t)} + N_v\, \Omega\right]}{\left|\Theta_v[(\underline{x}-\underline{x}')/\lambda]\right|^2 e^{2[a_v(\underline{x}, t)+a_v(\underline{x}', t)]}}. \tag{64}$$

This normalized error drops inversely as the product $\Delta T\, \Delta v$, the number of essentially independent samples of the emission process enclosed in the sample average. The other factor is often defined as a "fringe visibility function" (FVF).

$$\text{FVF} = \frac{\left|\Theta_v[(\underline{x}-\underline{x}')/\lambda]\right|^2 e^{2[a_v(\underline{x}, t)+a_v(\underline{x}', t)]}}{\left[\Theta_v(0)\, e^{2a_v(\underline{x}, t)} + N_v\, \Omega\right]\left[\Theta_v(0)\, e^{2a_v(\underline{x}', t)} + N_v\, \Omega\right]}. \tag{65}$$

As an example of the strong convergence of the sample mutual coherence toward the ensemble-average value, consider the case when the FVF is, say, 10^{-2}. Were it not for the noise term in (60), this would mean that the spatial frequency component in which we are interested has a squared magnitude only 1% of that of the zero-order component. With a conservative time-bandwidth product of 10^8, the resultant mean-square error in the sample coherence average is only one part in 10^6. The error tends to increase with the depth of fading; however, only rarely would the error be more than one or two orders

of magnitude greater. Because the error is so small, we can neglect it in comparison with the multiplicative disturbances introduced by the atmosphere and the inevitable measurement noise resulting from the quantum nature of the detectors. This is very important, as it means that not only is the mutual-coherence process a statistically sufficient description of the received electromagnetic phenomenon but the original uncertainty in the emission process is insignificant in the sampled values.

For this reason, we shall now discard the circumflex and denote the sample measurements $\Gamma_v(\underline{x}, \underline{x}+\underline{y}, t)$, since they are essentially identical to the ensemble values.

2.3.3 Extension to the Nonisoplanatic Case

Much of the preceding analysis has been predicated upon the condition that the object was entirely within an isoplanatic region. That is, both the phase and amplitude disturbances induced by the turbulence were invariant with angle over the dimensions of the object. If an object is small enough, this condition will surely hold. Often, however, there will be a variation in the angular dependence of the disturbances as we sweep across the source and we shall no longer get the simple relationship (Eq. 60) between the mutual-coherence process and the object intensity pattern.

In this more general case we have the result of Eq. 59 (disregarding the noise term)

$$\Gamma_v(\underline{x}, \underline{x}+\underline{y}, t) = \int d\underline{z}\, \Theta_v(z)\, e^{j2\pi \underline{z}, \underline{y}/\lambda}\, h_v(\underline{x}, \underline{x}+\underline{y}, \underline{z}, t), \tag{66}$$

or rewritten in terms of $\Theta(\underline{k})$

$$\Gamma_v(\underline{x}, \underline{x}+\underline{y}, t) = \int d\underline{k}\, \Theta_v(\underline{k}) \int d\underline{z}\, e^{-j2\pi \underline{z} \cdot (\underline{k}-\underline{y}/\lambda)}\, h_v(\underline{x}, \underline{x}+\underline{y}, \underline{z}, t), \tag{67}$$

where the inner integral determines the severity of the spatial frequency dispersion, because of the angular variations of the disturbances.

We can often reduce this more complicated form to something quite similar to the isoplanatic case. Suppose that we divide the field of view into a grid of areas, each of which is within an isoplanatic region. Furthermore, suppose that at the receiver we are able to separate the mutual coherence process into the separate contributions from each of these cells. If we can do this, we can then decompose the channel into a number of parallel channels, each of which behaves in the isoplanatic manner, although the particular atmospheric disturbance may be different on each channel. We can look at each channel independently, and build up a composite picture of the object.

The problem in such an approach is distinguishing the contributions to the mutual-coherence process from each individual isoplanatic region. Whether we can or cannot make this separation depends upon the angular scale of the disturbances relative to the correlation scale as a function of the aperture coordinate; that is, whether

the aperture coherence area Δx^2 is capable of "resolving" the angular correlation scale.

The separation of the mutual coherence process into angular components is accomplished by first mathematically Fourier-transforming on the variable $\underline{y}$ to generate a pseudo image

$$I(\underline{u}, t) = \int d\underline{y}\ \hat{\Gamma}_v(\underline{x}, \underline{x}+\underline{y}, t)\ e^{-j2\pi \underline{u} \cdot \underline{y}/\lambda}. \tag{68}$$

This pseudo image differs from the regular image formed by a lens (see section 1.2.1), in that there is no $\underline{x}$ integration of Γ beyond a coherence area. If we ignore the background radiation, which only adds a uniform intensity bias, (68) becomes

$$I(\underline{u}, t) = \int d\underline{z}\ \theta_v(\underline{z}) \int d\underline{y}\ e^{-j2\pi(\underline{u}-\underline{z}) \cdot \underline{y}/\lambda}\ h_v(\underline{x}, \underline{x}+\underline{y}, \underline{z}, t) \tag{69}$$

which can be put in the simpler form

$$I(\underline{u}, t) = \int d\underline{z}\ \theta_v(\underline{z})\ H_v(\underline{x}, \underline{u}-\underline{z}, \underline{z}, t), \tag{70}$$

where

$$H_v(\underline{x}, \underline{w}, \underline{z}, t) = \int d\underline{y}\ e^{-j2\pi \underline{w} \cdot \underline{y}/\lambda}\ h_v(\underline{x}, \underline{x}+\underline{y}, \underline{z}, t). \tag{71}$$

It is in this pseudo-image plane $\underline{u}$ that we try to separate the various isoplanatic regions. The effect of the impulse response function H in (70) is to give a spreading or smearing of the function θ. This impulse response is a random process that depends upon frequency, time, and position coordinate $\underline{x}$, but more important, at present, it may also depend upon the angular coordinate $\underline{z}$. If the change in H with respect to the variable $\underline{z}$ is on a scale that is smaller than the image spreading described by the integral operation (70), any point $\underline{u}$ will be comprised of contributions from the object that have suffered different distortions. Thus, to be able to reduce the channel to the desired form, we must guarantee that the width of the impulse response H (in the coordinate $\underline{w}$ of Eq. 71) is less than the characteristic angular scale size or angular correlation distance Δz. The width of H can be estimated from the reciprocal width of its Fourier transform, h. We have previously stated that the phase and amplitude disturbances remain correlated over a distance Δx. Thus h will show no significant changes with $\underline{y}$ on a scale smaller than Δx, and the width of the impulse response is then roughly $\lambda/\Delta x$. The pseudo image $I(\underline{u})$ can then be broken into isoplanatic regions, over each of which the impulse response is invariant with $\underline{z}$, provided that

$$\frac{\lambda}{\Delta x\ \Delta z} < 1. \tag{72}$$

In radio-scatter communication there is an analogous condition in which the channel is said to be underspread, provided that the product of the frequency-dispersion bandwidth and the time spreading is less than one. We recognize that $1/\Delta z$ is the spatial frequency dispersion, and $\lambda/\Delta x$ is the angular spreading, so we appropriate the term under spread to describe the condition (72). We refer to the converse situation as the overspread channel.

In the rest of this report we shall consider only the underspread condition.

2.4 MEASUREMENT OF THE MUTUAL-COHERENCE PROCESS

We have shown that a sufficient set of statistics can be extracted from the received field through sample measurements of the mutual-coherence process

$$\Gamma_v(\underline{x}, \underline{x}+\underline{y}, t) = \langle E_v(\underline{x}, t)\, \overset{*}{E}_v(\underline{x}+\underline{y}, t)\rangle, \tag{73}$$

in which the angular brackets represent a local integration over the optical correlation bandwidth Δv, the correlation time ΔT, and the correlation area Δx^2 within the field of view, Ω. These sampling parameters are dependent primarily upon corresponding correlation properties of the turbulence-induced amplitude and phase disturbances.

We now turn to the physical measurement of these sufficient statistics. At low frequencies (radio frequencies) the coherence of an electromagnetic field is determined by analogue correlation of the voltages induced on two antennas. At optical frequencies, however, such direct measurements are precluded, and instead the phenomena of wave interference are used. The magnitude and the phase of the mutual-coherence process are determined from the degree of constructive or destructive interference obtained when the fields at points $\underline{x}$ and $\underline{x}+\underline{y}$ are added.

Just about all interferometers exploit this basic principle, and differ only in the way in which the fields are added together; that is, in the various forms of temporal and spatial modulation which are introduced so that the interference effect can be distinguished. We shall describe several of the interferometer types that seem suitable for sampling the coherence process in the required manner. We assume that the incident light has been already filtered to the correlation bandwidth Δv.

2.4.1 Simple Interferometer

Let us consider the simplest scheme for measuring field coherence. From such an understanding we can then better appreciate more complicated systems. Probably the most basic configuration is the one sketched in Fig. 8, in which the fields from the two arms of the interferometer are superimposed by means of the mirrors and beam splitter.

One of the mirrors is usually tilted slightly by a small angle so that a spatially varying phase, $2\pi\underline{u}\cdot\underline{y}/\lambda$, exists between the two superimposed field patterns.

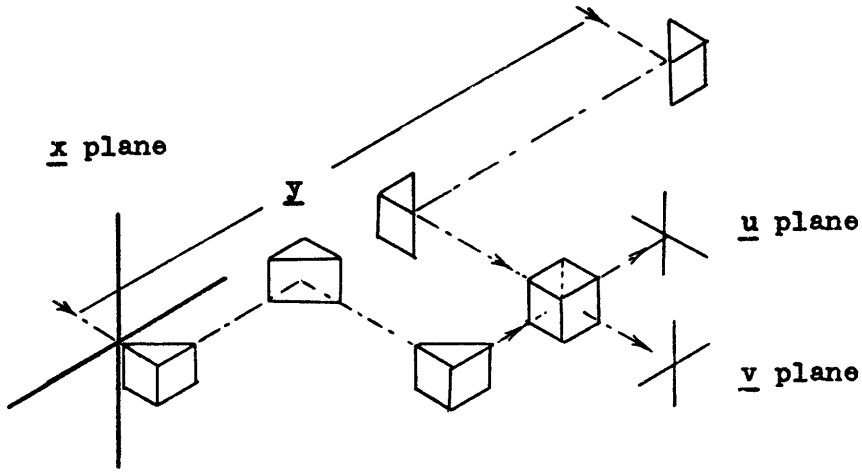

Fig. 8. Simple interferometer.

The intensity of the total light in either the $\underline{u}$ or $\underline{v}$ plane has the form

$$I(\underline{u},t) = \frac{1}{2}\overline{\left| E_v(\underline{x}=\underline{u},t) + E_v(\underline{x}'=\underline{u}+\underline{y})\, e^{+j2\pi \underline{u}\cdot\underline{y}/\lambda} \right|^2}$$

$$= \frac{1}{2}\Gamma_v(\underline{u},\underline{u},t) + \frac{1}{2}\Gamma_v(\underline{u}+\underline{y},\underline{u}+\underline{y},t) + \left|\Gamma_v(\underline{u},\underline{u}+\underline{y},t)\right| \cos\left[2\pi \underline{u}\cdot\underline{y}/\lambda + \phi(\underline{u},\underline{u}+\underline{y},t)\right], \qquad (74)$$

where $\phi(\underline{u},\underline{u}+\underline{y},t)$ is the phase angle of the complex mutual coherence, and factors of 1/2 are due to the energy division by the beam splitter. By measuring the amplitude and spatial phase of the fringes, we obtain the corresponding mutual-coherence measurement.

The usual way of extracting the amplitude and phase of the fringes is to correlate the spatial pattern with both sine and cosine patterns of the same spatial frequency. A direct electrical analogue signal can be obtained by scanning a mosaic of photoelectric detectors. This can be an array of separate elements so connected as to give the appropriate correlations, or it can be an internally scanned detector such as an image orthicon or vidicon tube. This scanning can be done later if a fast exposure photograph is taken of the fringes (exposure time less than the correlation time ΔT).

There are also several inexpensive electromechanical means of determining the spatial phase and amplitude of the fringes. One can simply scan the fringes with a moving pinhole in front of the detector surface, and thereby generate a time-variant electrical output from which the phase and amplitude can be determined. This is an inefficient means, however, since most of the available light energy is wasted. A more efficient scanning mechanism incorporates a glass plate having alternate parallel opaque and transparent rulings with spacing matched to that of the fringes, as shown schematically in Fig. 9.

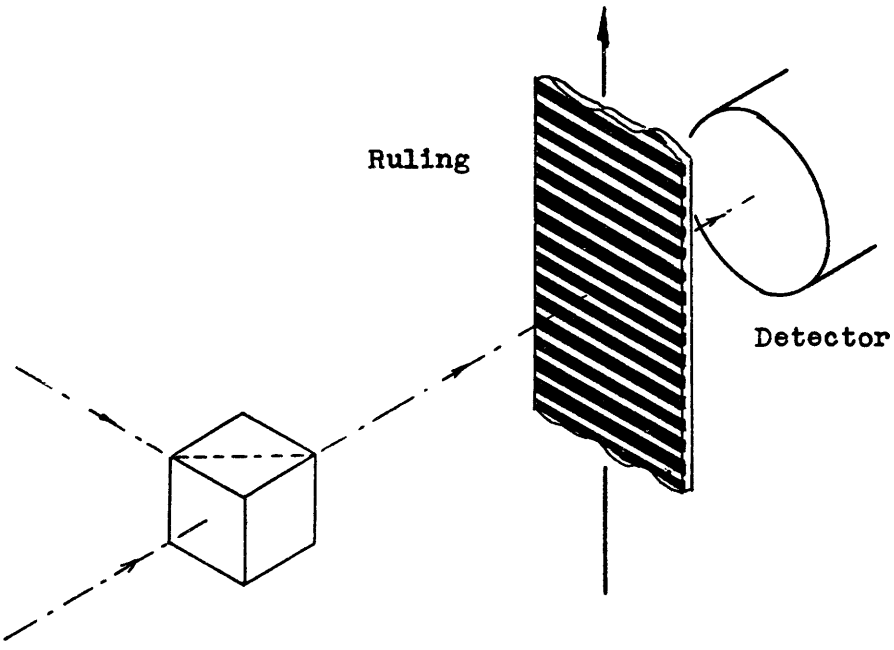

Fig. 9. Fringe scanner.

When the plate is moved uniformly in a direction perpendicular to the rulings and the fringes, the transmitted light gives a periodic detector output signal. The phase and amplitude of this electrical signal are the same as those of the fringes.

The variation in transmittance on the plate need not be exactly sinusoidal, indeed a square wave is fine. The higher spatial harmonics in the ruling pattern only correlate with higher spatial frequency components in the fringe pattern. If such components exist in the fringe pattern, their effect in the detector output can be suppressed by electrical filtering, since they appear as corresponding high-frequency terms in the output signal.

Ramsey and Kobler[16] have cleverly employed this fringe-scanning principle by using a rotating disk with radially ruled lines. When the fringes are confined to a small area, the rulings appear essentially parallel. A somewhat similar device was employed in our measurements (see Section IV). An inexpensive Ronchi ruling (a glass plate with parallel opaque and transparent lines) was moved back and forth in reciprocating fashion to scan the fringes.

2. 4. 2 Fresnel Biprism

Another way of implementing the same basic interferometer of Fig. 8 (but avoiding the mirrors and beam splitters) is by means of a Fresnel biprism whose operation is indicated in Fig. 10.

The light incident on the top half of the prism is deflected downward by an angle γ,

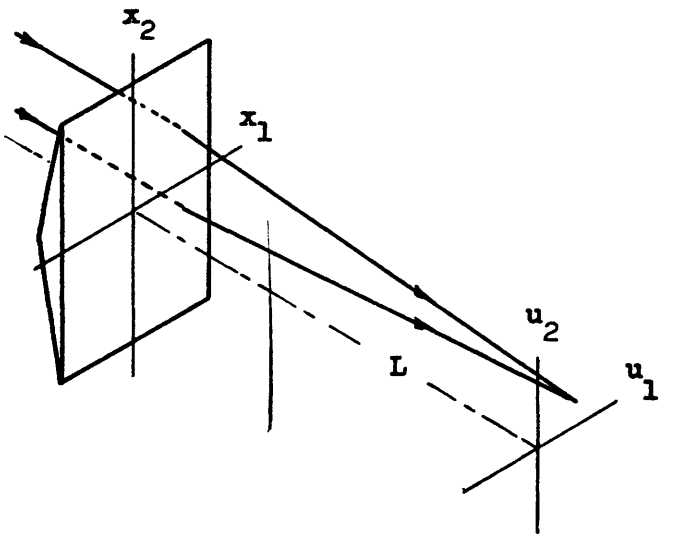

Fig. 10. Fresnel biprism.

and that incident on the bottom half deflected upward by the same angle. Over a plane L units behind the prism, the intensity is

$$I(u,t) = \Gamma_v(\underline{x},\underline{x},t) + \Gamma_v(\underline{x}',\underline{x}',t) + 2\left|\Gamma_v(\underline{x},\underline{x}',t)\right| \cos\left(2\pi u_2 \sin\gamma/\lambda + \phi(\underline{x},\underline{x}',t)\right), \quad (75)$$

where

$$\underline{x} = u_1, u_2 + L\tan\gamma \quad (76)$$

and

$$\underline{x}' = u_1, u_2 - L\tan\gamma. \quad (77)$$

When the angle γ is small we can approximate both tan γ and sin γ by γ.

Fringes appear in the u_1 direction, and these fringes have the same phase and amplitude as those of the mutual-coherence process. The displacement in the measurement is related to the distance L between the prism and the recording, and the effective displacement is

$$\underline{y} = (0, 2L\tan\gamma/\lambda). \quad (78)$$

Moving farther back from the prism yields a larger value of spatial frequency, and we have the advantage that the fringe spacing remains the same, thereby simplifying the scanning device. By also rotating the prism, all values of $\underline{y}$ can be considered.

As we have mentioned, the mutual-coherence process should be sampled in a number of dimensions. Presumably, the correlated optical frequency bands can be isolated with a set of bandpass interference filters, and each detector output can be sampled appropriately in time. Isolation of the measurements to the aperture correlation areas can

be realized by locally integrating the fringe patterns, thereby sampling with a different detector element for each correlation area.

2.4.3 Lloyd's Mirror

The Fresnel biprism samples the coherence function in $\underline{x}$, but without movement of the prism yields only a single value of $\underline{y}$. A device which can sample the coherence

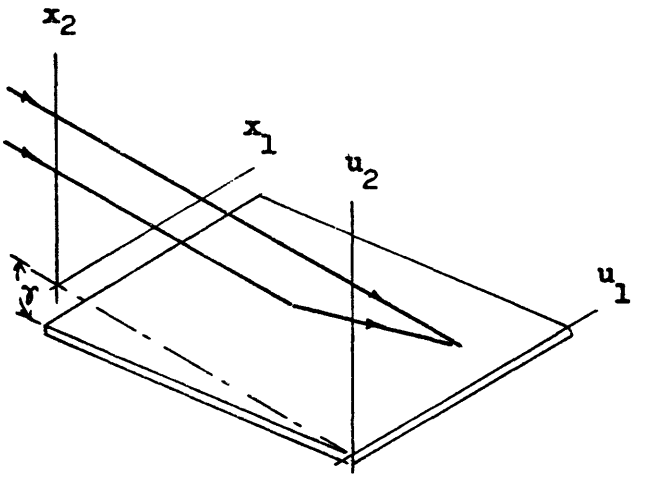

Fig. 11. Lloyd's mirror.

process in the x_1 aperture dimension and the y_2 displacement dimension is the Lloyd's mirror arrangement shown in Fig. 11. The mirror is placed at an angle γ to the incoming radiation. The intensity of the field on the $\underline{u}$ plane then is

$$I_v(\underline{u},t) = \left| E_v(x_1=u_1, x_2=u_2, t) + E(x_1=u_1, x_2=u_2-2u_2\cos\gamma, t)\, \exp(j2\pi(2u_2\sin\gamma)/\lambda) \right|^2. \quad (79)$$

The local interference fringes at (u_1, u_2) then give us the mutual-coherence measurement

$$\Gamma[\underline{x}=u_1, u_2, \underline{x}+\underline{y}=u_1, u_2(1-2\cos\gamma)]. \quad (80)$$

That is, the displacement is

$$\underline{y} = (0, -2u_2\cos\gamma). \quad (81)$$

If additional mirrors and prisms are used, the intensity on the measurement plane $\underline{u}$ can be made to take the form

$$I_v(\underline{u},t) = \left| E_v(\underline{x}=\underline{u}, t) + E_v(\underline{x}=-\underline{u}, t)\, e^{j2\pi\underline{\gamma}\cdot\underline{u}/\lambda} \right|^2 \quad (82)$$

and the fringe producing term is

$$2\left|\Gamma_v(\underline{x}=\underline{u}, \underline{x}+\underline{y}=-\underline{u}, t)\right| \cos\left[2\pi \underline{y}\cdot \underline{u}/\lambda + \phi(\underline{x}=\underline{u}, \underline{x}+y=-\underline{u}, t)\right]. \tag{83}$$

The local phase and amplitude of this term yield the mutual coherence for all values of displacement as $\underline{y} = -2\underline{u}/\lambda$. It should be noted that each value $\underline{y}$ is sampled with a separate pair of aperture points.

All of these interferometer configurations can be modified by employing a time jitter in one of the paths; for example, by twisting or moving a mirror. The phase and amplitude of the field coherence can then be obtained from the temporal phase and amplitude of each detector output, rather than by spatially scanning fringes.

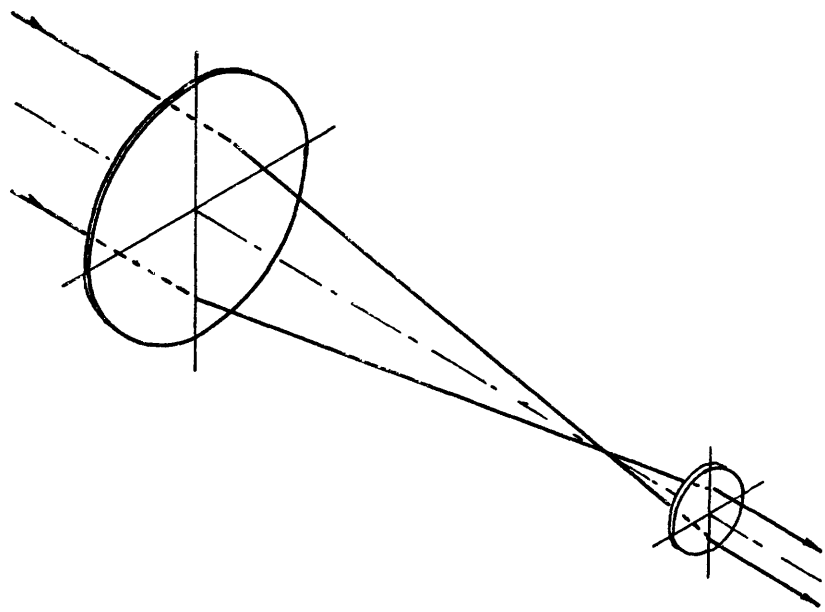

Fig. 12. Aperture reduction.

One might not necessarily see these various interferometers in just the form described. By various clever uses of special prisms and mirrors, more practically useful devices can be constructed that still exploit the same basic ideas.

It should be pointed out that the prisms and mirrors used in these schemes need not be as large as the actual receiving aperture because the field size can be conveniently reduced by means of an objective lens (or mirror) and a lens of shorter focal length (see Fig. 12). The field scale is then reduced by the ratio of the focal lengths of the elements.

2.4.4 The Lens as an Interferometer

We recall that the mutual-coherence process can be determined by looking at the Fourier transform of the image formed by a simple lens (see Fig. 13).

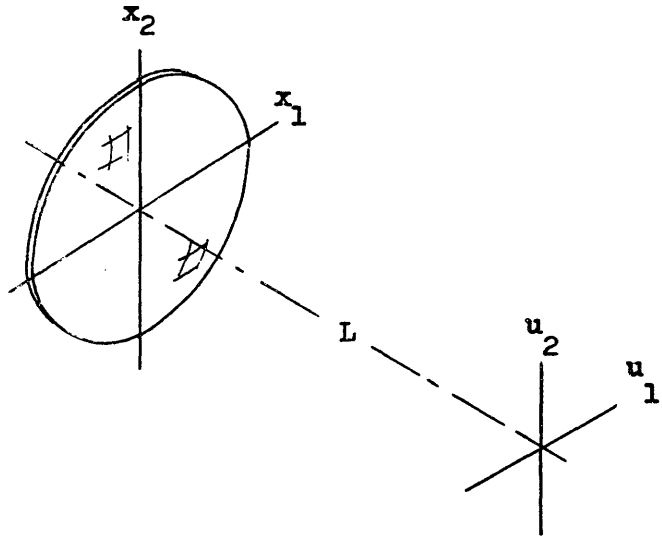

Fig. 13. Lens geometry.

The field over the focal plane of an aberration-free lens is closely approximated by the relationship

$$E_v(\underline{u}, t) = \frac{1}{\lambda L} \int d\underline{x}\, w(\underline{x})\, E_v(\underline{x}, t)\, e^{-j2\pi \underline{u} \cdot \underline{x}/\lambda L}, \tag{84}$$

where $w(\underline{x})$ is the transmittance function for the lens and may be possibly complex (phase-shading). The intensity of the focal plane field is

$$I_v(\underline{u}, t) = \frac{\Delta v}{(\lambda L)^2} \int d\underline{x} \int d\underline{x}'\, w(\underline{x})\, \overset{*}{w}(\underline{x}')\, \Gamma_v(\underline{x}, \underline{x}', t)\, e^{-j2\pi \underline{u} \cdot (\underline{x}-\underline{x}')/\lambda L}, \tag{85}$$

where Γ_v is the coherence function measured per unit optical bandwidth, and the factor Δv accounts for the integration across the correlation bandwidth.

The spatial Fourier transform of this image (with a sign reversal employed to account for the image inversion), is simply

$$\mathcal{I}_v(\underline{k}, t) = d\underline{u}\, I(\underline{u}, t)\, e^{+j2\pi \underline{k} \cdot \underline{u}/L}$$

$$= \Delta v \int d\underline{x}\, w(\underline{x})\, \overset{*}{w}(\underline{x}-\lambda \underline{k})\, \Gamma_v(\underline{x}, \underline{x}-\lambda \underline{k}, t). \tag{86}$$

In the normal use of a lens the integration on $\underline{x}$ extends over the full aperture. We can localize the measurements of coherence by an appropriate choice of transmittance function $w(\underline{x})$. Suppose, for example, that we mask the lens except for two small holes,

each of area Δx^2 and separated by some distance $\underline{y}$ (see Fig. 14). With Δx^2 matched to the correlation area of the atmospheric disturbances, (86) can then be rewritten

$$\mathcal{J}_v(\underline{k}, t) = \Delta v\ \Gamma_v(\underline{x}_o, \underline{x}_o - \lambda\underline{k}, t) \int w(\underline{x})\ \overset{*}{w}(\underline{x} - \lambda\underline{k})\ d\underline{x}. \tag{87}$$

The function defined by the integral in expression (87) determines the values of displacement and corresponding spatial frequencies which can be extracted from the image

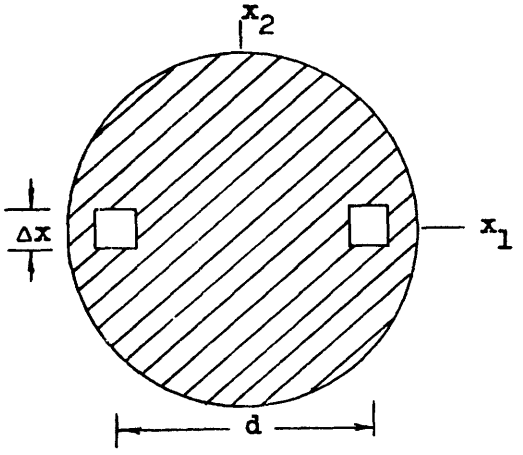

Fig. 14. Aperture mask.

transform $\mathcal{J}$. We denote this integral as a transfer function $H_M(\underline{k})$, which is determined in exactly the same way as the ordinary diffraction-limited MTF (see section 1. 2. 2).

$$H_M(\underline{k}) = \int w(\underline{x})\ \overset{*}{w}(\underline{x} + \lambda\underline{k})\ d\underline{x}. \tag{88}$$

Figure 15 shows the form of the transfer function for the two-hole mask. We have used square holes in this example to simplify the evaluation of $H_M(\underline{k})$.

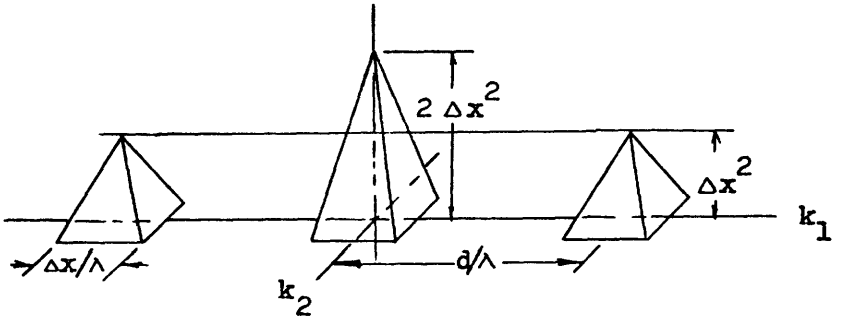

Fig. 15. Transfer function.

Besides localizing the coherence process in the $\underline{x}$ variable to a single correlation area, a receiver should also integrate Γ over a range of displacement values. This operation is mathematically equivalent to restricting the angular field of view to just the region of the object, to exclude as much of the background as possible. We do this in the focal plane by inserting a field stop, another mask with a small hole matched to the image.

When a telescope is used in this manner it is commonly referred to as a Michelson stellar interferometer (see Born and Wolf[17]) which is used in the measurement of star diameters. The spacing between the openings in the mask is increased until the fringes disappear. At this point the wave-front coherence has dropped, thereby indicating that we have passed the uppermost significant spatial frequencies in the object, and from such knowledge we can deduce the approximate dimensions of the object.

Spatial frequencies greater than those admitted by the aperture of the lens can be sampled by using mirrors to extend the baseline (see Fig. 16).

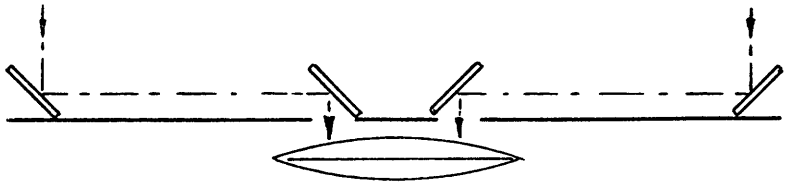

Fig. 16. Baseline extension.

Changing the spacing of the outermost mirrors is a convenient way to sweep across the spatial-frequency spectrum, since the fringe spacing remains constant in the focal plane.

Finally, we might say a word regarding the practical significance of the underspread condition (section 2.3.3). When the holes in the mask have the characteristic dimension Δx, the resultant diffraction effects spread the image in the focal plane to an apparent angular width of approximately $\lambda/\Delta x$. That is, neither the amplitude nor phase of the fringe pattern can change on a scale finer than this. Thus if we are to resolve the angular correlation region, we require $\lambda/\Delta x < \Delta z$.

2.5 NOISE IN THE MEASUREMENT OF MUTUAL COHERENCE

We have just considered various interferometer schemes for sampling mutual coherence. We want to sample the mutual-coherence process in all of the relevant variables—time, optical frequency, aperture space and displacement – in order to retain all of the statistically relevant information contained in the incident field. Such a sampling should give us maximum use of the spatial and temporal channel diversity. We have considered several schemes for sampling the coherence function. Our object now is to study the additional disturbances that the quantum nature of radiation introduces into the

interferometer measurements. We shall have then completed the channel modelling, and can go on to the performance of optimum processing schemes for parameter estimation.

Let us look at the statistical behavior of the measurement noise that arises because the basic principle of energy detection is a counting of photons whose arrival is stochastic in nature. If the intensity of the radiation is very low and we employ a detector with a large bandwidth, then individual photons (or more properly photoelectrons) can be resolved. Usually, however, the detector current represents an integration of a large number of such current pulses. Let us suppose that the detector has a minimum integration or resolving time, τ. We now ask for the statistical behavior of the detector output, still conditioned on knowledge of the intensity of the object and the amplitude and phase disturbances of the atmosphere (a, b). The detectors should be chosen to have a resolving time less than the correlation time of the turbulence.

There are two random phenomena that yield uncertainty in the detector output. The first is the random photon-detection process, the second is the Gaussian nature of the incident radiation.

Let us subdivide our resolution period τ into small intervals $\delta_1, \delta_2 \ldots \delta_N$ $(N=\tau/\delta)$, where δ is shorter than the coherence time of the incident field. If we condition on knowledge of this field, the corresponding counts $c_1, c_2 \ldots c_N$ are independent, Poisson-distributed, random variables with a mean and variance

$$\bar{c}_i = \overline{(c_i - \bar{c}_i)^2} = g\,\delta\,\Delta u^2 |E_i|^2, \tag{89}$$

where

Δu^2 is the area of the detector

$|E_i|^2$ is the instantaneous power flux density of the incident field

and

$$g = \frac{q}{vh} \quad \begin{matrix} \text{(quantum efficiency)} \\ \text{(frequency} \times \text{Planck's constant)}, \end{matrix} \tag{90}$$

where g is in counts/Joule.

The total count in the period τ then is

$$c = \sum_{i=1}^{N} c_i. \tag{91}$$

Averaging over the Gaussian statistics gives a mean count of

$$\bar{\bar{c}} = g\delta\Delta u^2 \sum_{i=1}^{N} \overline{|E_i|^2}$$

$$= g\tau\Delta u^2 I, \tag{92}$$

where I is the average power flux density (the double bar is used to indicate averages over the two random phenomena). This average count then represents the signal component in the output. The variation from this average count we call the noise, and it has variance

$$\overline{\overline{(c-\bar{\bar{c}})^2}} = g^2\delta^2\Delta u^4 \sum_{i=1}^{N}\sum_{j=1}^{N} \overline{|E(t_i)\overset{*}{E}(t_j)|^2} + g\tau\Delta u^2 I. \tag{93}$$

Under the assumption that the resolving period τ is many times longer than the correlation time of the incident process, one of the summations in (93) can be extended to $+\infty$ without significant error, and we obtain

$$\overline{\overline{(c-\bar{\bar{c}})^2}} = g^2\tau\Delta u^4 \int_0^{+\infty} |\Gamma(t)|^2\, dt + g\tau\Delta u^2 I, \tag{94}$$

where $\Gamma(t)$ is the stationary temporal coherence function for the field. We can define a coherence time τ_c for the process as

$$\tau_c = \frac{\int_0^{+\infty} |\Gamma(t)|^2\, dt}{I^2}, \quad \text{where} \quad I^2 = |\Gamma(O)|^2. \tag{95}$$

We thus obtain

$$\overline{\overline{(c-\bar{\bar{c}})^2}} = g\tau\Delta u^2 I + g^2\tau^2\Delta u^4 I^2(\tau_c/\tau), \tag{96}$$

where

$$\bar{\bar{c}} = g\tau\Delta u^2 I. \tag{97}$$

We see that the noise variance comes from two independent effects. There is first the shot-noise term $g\tau\Delta u^2 I$. It would have the same value if the field were constant, rather than random. The second term, $g^2\tau^2\Delta u^4 I^2(\tau_c/\tau)$, results from the residual uncertainty in the sample average intensity when approximately τ/τ_c independent samples are considered. Generally, τ/τ_c is extremely large (easily of the order of a million). Thus this "photon-bunching" term is usually insignificant in comparison with the shot-noise term. The effect is really the same phenomenon as that in the classical

approach when we considered the variance between the sample-average and ensemble-average coherence functions.

Let us now examine the correlation of the noise for a pair of observations. Consider a pair of fields $E_1(t)$ and $E_2(t)$ related by a temporal crosscorrelation function $\Gamma_{1,2}$. Each of these fields is detected on separate counters giving counts

$$c = c_1 + c_2 + \cdots\cdots c_N$$

$$c' = c'_1 + c'_2 + \cdots\cdots c'_N, \tag{98}$$

where the resolving period has again been subdivided. We want to consider the correlation

$$\overline{(c-\bar{c})(c'-\bar{c}')} = \overline{\left[\sum_{i=1}^{N} [c_i] - g\tau\Delta u^2 I_1\right]\left[\sum_{j=1}^{N} [c'_j] - g\tau\Delta u^2 I_2\right]}$$

$$= g\delta^2(\Delta u)^4 \sum_{i=1}^{N}\sum_{j=1}^{N} |\Gamma_{1,2}(t_i - t_j)|^2. \tag{99}$$

Now, again extending one pair of the summation limits to $+\infty$ and defining a correlation time between the two processes as

$$\tau_c = \frac{\int_0^{+\infty} |\Gamma_{1,2}(t)|^2 \, dt}{|\Gamma_{1,2}(O)|^2}, \tag{100}$$

we obtain

$$\overline{(c-\bar{c})(c'-\bar{c}')} = g^2\Delta u^4 \tau^2 |\Gamma_{1,2}(O)|^2 (\tau_c/\tau). \tag{101}$$

This crosscorrelation term for the noises is purely a "photon-bunching" effect, shot-noise components being independent. When there is no coherence between the fields the correlation between the noises is strictly zero. This is the case when the two time intervals are disjoint and each is much larger than the coherence time of the radiation. It matters not whether we consider two different detectors or the same detector.

When we have field coherence there is some noise correlation but, since this correlation is of the same order as the "photon-bunching" term in the variance function, it is generally quite insignificant.

We can, therefore, for the most part of the succeeding analysis, disregard all but the shot-noise term. The other term does have significance in the Hanbury Brown and Twiss intensity interferometer, which will be briefly considered in Section III. With this

technique, field coherence can be deduced from the correlation of intensities, because of the "photon-bunching" term. This, however, would require a very large detector bandwidth in order to be practical.

The fact that the dominant shot-noise components are uncorrelated for disjoint observation times and disjoint detector areas, simplifies considerably the analysis of the noise in our coherence measurements.

Consider the result of correlating an intensity fringe pattern $I(\underline{u})$ incident on an array of detectors with spatial frequency $\cos(2\pi\underline{k}\cdot\underline{u})$. The result of this operation we denote

$$S_c \propto \int I(\underline{u}) \cos(2\pi\underline{k}\cdot\underline{u})\, d\underline{u}. \tag{102}$$

We determine S_c as

$$S_c = \sum_i c_i \cos(2\pi\underline{k}\cdot\underline{u}_i), \tag{103}$$

where we have denoted by c_i the photoelectron count from the detector element at

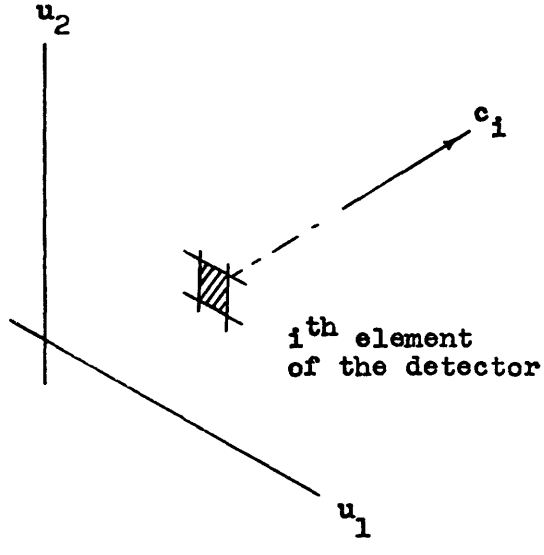

Fig. 17. Detection array.

point $\underline{u}_i$ (see Fig. 17).

From Eq. 92, it follows that

$$\bar{S}_c = \sum_i \bar{c}_i \cos(2\pi\underline{k}\cdot\underline{u}_i)$$

$$= g\Delta T \sum_i I(\underline{u}_i) \cos(2\pi\underline{k}\cdot\underline{u}_i)\, \Delta u^2, \tag{104}$$

where the integration time is now ΔT, the correlation time of the atmospheric disturbances. We represent the averaging by a single overbar, as it is no longer necessary to distinguish the two imbedded random processes (the Gaussian radiation and the Poisson photodetection process). The summation in (104) can be replaced by an integration (under the assumption that the detector elements are small), and we obtain

$$\bar{S}_c = g\Delta T \int I(\underline{u}) \cos (2\pi \underline{k} \cdot \underline{u})\, du. \tag{105}$$

In terms of $\mathscr{I}(k)$, the spatial Fourier transform of the pattern, $\bar{S}_c$ becomes

$$\bar{S}_c = g\Delta T \, \mathrm{Re}\,[\mathscr{I}(k)]. \tag{106}$$

Likewise, when we correlate against $\sin (2\pi \underline{k} \cdot \underline{u})$ to obtain the quadrature component

$$S_s \propto \int I(\underline{u}) \sin 2\pi \underline{k} \cdot \underline{u})\, du, \tag{107}$$

we obtain

$$\bar{S}_s = g\Delta T \, \mathrm{Im}\,[\mathscr{I}(\underline{k})]. \tag{108}$$

The effect of the shot noise resulting from the random emission of photoelectrons gives two zero-mean corresponding noise variables n_c and n_s. The mean-square value of each of these is the same, and is obtained as

$$\overline{n_c^2} = \overline{(s_c - \bar{S}_c)^2}$$

$$= \sum_i \sum_j \overline{(c_i - \bar{c}_i)(c_j - \bar{c}_j)} \cos (2\pi \underline{k} \cdot \underline{u}_i) \cos (2\pi \underline{k} \cdot \underline{u}_j). \tag{109}$$

From Eq. 101, we found that the covariance of the counts on disjoint detectors is due entirely to the "photon bunching," that is, to the statistical structure of the received radiation, and is negligible for the relatively long integration times employed. Thus (109) reduces to

$$\overline{n_c^2} = \sum_i \overline{(c_i - \bar{c}_i)^2} \cos^2 (2\pi \underline{k} \cdot \underline{u}_i) \tag{110}$$

which, with the aid of (96) (retaining only the shot term), becomes

$$\overline{n_c^2} = g\Delta T \int I(\underline{u}) \cos^2 (2\pi \underline{k} \cdot \underline{u})\, du. \tag{111}$$

Similarly, the noise on the quadrature component is

$$n_s^2 = g\Delta T \int I(\underline{u}) \sin^2 (2\pi \underline{k} \cdot \underline{u})\, du. \tag{112}$$

These can be rewritten

$$n_c^2 = \frac{g\Delta T}{2} [\mathscr{I}(O) + \mathrm{Re}\ \mathscr{I}(2\underline{k})] \tag{113}$$

and

$$n_s^2 = \frac{g\Delta T}{2} [\mathscr{I}(O) - \mathrm{Re}\ \mathscr{I}(2\underline{k})]. \tag{114}$$

In the case of the simple interferometer forms (sections 2.4.1 and 2.4.2) the fringe pattern does not contain any component at the double frequency $2\underline{k}$. Moreover, in the case of a lens with a two-hole mask, the double frequency is usually beyond the limit of the MTF (Fig. 15). Thus, we can drop the second term in (113) and (114), which leaves

$$\overline{n_c^2} = \overline{n_s^2} = \frac{g\Delta T}{2}\ \mathscr{I}(O). \tag{115}$$

When the double-frequency component is absent, it also turns out that n_c and n_s are uncorrelated.

We now apply the results of Eqs. 106, 108, and 115 to the simple interferometers or the masked lens. The squared magnitude of the mean complex signal $\bar{S} = \bar{S}_c + j\bar{S}_s$ is

$$|\bar{S}|^2 = g^2\, \Delta T^2\, \Delta v^2\, \Delta x^4\, |\Theta_v(\underline{k})|\, e^{2[a_v(\underline{x}, t)+a_v(\underline{x}-\lambda\underline{k}, t)]}. \tag{116}$$

Similarly, the mean-square value of the magnitude of the complex noise component n is

$$\overline{|n|^2} = g\Delta T\, \Delta v\, \Delta x^2 \left[\Theta_v(O)\, e^{2a_v(\underline{x}, t)} + N_v \Omega\right] \left[\Theta_v\, e^{2a_v(\underline{x}-\lambda\underline{k}t)} + N_v \Omega\right]. \tag{117}$$

The variance of the shot-noise variable is dependent upon both the background radiation N_v, the object radiation Θ_v, and the atmospheric fading $a_v(\underline{x}, t)$. When we come to study performance limitations, we shall simplify the analysis by supposing that N_v is sufficiently large that it is the dominant component in the noise variance. This then removes the dependence of the noise variance on the atmospheric process and the object. Furthermore, we assume in Section III that the noise variable n represents an average over a sufficient number of counts that a Gaussian approximation is valid.

The signal-to-noise ratio then is

$$\frac{|\bar{S}|^2}{|n|^2} = \frac{g\Delta T\ \Delta v\ \Delta x^2}{\Omega N_v} |\Theta_v(\underline{k})|^2 \exp\{2[a_v(\underline{x}, t)+a_v(\underline{x}-\lambda\underline{k}, t)]\}. \tag{118}$$

This signal-to-noise ratio was calculated for a scheme in which a spatial fringe pattern is formed. If we use a moving mirror to obtain a periodic detector signal, the signal-to-noise ratio in the coherence measurement will be exactly the same. Scanning the fringes with the ruling device of section 2.4.1 does result in a slight loss in signal-to-noise ratio. Some of the light energy is blocked by the opaque regions, which results in a loss of a little more than a factor of two in signal-to-noise ratio.

2.6 COMMENTS

The results of section 2.5 give the signal-to-noise ratio for the measurement of the mutual-coherence process, isolated to a single correlation time ΔT, correlation bandwidth Δv, pair of correlation areas Δx^2, and field of view Ω. In order to retain all information in the received phenomenon (at least in the classical sense), we should simultaneously sample the mutual-coherence process for all such available frequency bands, time intervals, pairs of correlation areas, and spatial frequencies. Conceptually at least, simultaneous sampling in frequency could be done by first diverting the light into a number of channels, one for each frequency band, with the use of some system of lossless interference filters. There would be no loss in the signal-to-noise ratio given by Eq. 118. There is no trouble in sampling all time intervals.

It is in sampling over aperture position and displacement (spatial frequency) that trouble arises. First, however, consider the displacement as fixed. The field incident upon a particular correlation area should then be interfered only with the fields through two other such areas. If this is done by using different interferometers, the signal-to-noise ratio is then reduced by a factor of two, because of the necessary energy division.

This is not too serious; however, when we try to sample over the full range of spatial frequencies we encounter problems. Now we must interfere the field on a particular correlation area with those on all other areas. If we have M areas, we might use beam splitters to funnel the energy to M-1 additional interferometers. Unfortunately, the light energy is then split M ways, with a subsequent M-fold decrease in signal-to-noise ratio on each interferometer measurement.

The problem is more subtle than this, in that we can devise schemes of introducing a spatially varying frequency shift to the incident field, using systems of moving mirrors, etc. There is no division of the light energy, and indeed only a single detector need be employed. The coherence at various values of both position and displacement show up as orthogonal frequencies in the spectrum of the detector output. In terms of our noise model (section 2.5), this means that the signal component of the detector

output is unchanged from a system using only a single pair of correlation areas. Unfortunately, the noise takes an M-fold increase because the total energy incident on the detector is now M times as large. Thus, no matter how ingenious we try to be, it appears that we are faced with the fundamental problem of compromising between a small set of spatial frequency samples with minimum noise and a large set with much higher noise.

In Section III we shall consider the limitations on the best possible strategies of estimating the phase and amplitude of the Fourier transform of the object pattern, using the data from a particular set of measurements. After understanding what can be done with a particular set of measurements, we can determine the most reasonable compromises for selecting a sampling scheme.

III. PERFORMANCE LIMITATIONS AND SIGNAL-PROCESSING TECHNIQUES

We have determined the statistically sufficient set of measurements that a receiver should perform upon the atmospherically distorted incident field to retain all relevant information for optimal reconstruction of the image. We shall now explore the manner in which these measured values should be processed to form the image estimate. First, we determine the best possible performance by means of the Cramer-Rao (C-R) inequality which lower-bounds the variance of any unbiased estimate. Second, we demonstrate receiver structures that either attain this lower limit or approach it asymptotically. Finally, we discuss various practical realizations of these structures.

We have shown that sufficient field measurements are obtained by a bank of parallel interferometers that measure the mutual coherence process, which is defined as

$$\Gamma_v(\underline{x}, \underline{x}+\underline{y}, t) = \langle E_v(\underline{x}, t)\overset{*}{E}_v(\underline{x}+\underline{y}, t)\rangle. \tag{119}$$

The sample averaging denoted by angular brackets is a local integration, or smoothing of the mutual coherence function, where

- v the optical frequency is integrated over the optical correlation bandwidth Δv
- t the time is integrated over the correlation period Δt
- $\underline{x}$ the aperture coordinate is integrated over the correlation region $(\Delta x)^2$
- $\underline{y}$ the displacement variable is integrated over a correlation region $(\Delta y)^2$, equivalently a restriction of the field of view to a solid angular region $\Omega = (\lambda/\Delta y)^2$.

These correlation regions, for the most part, are the corresponding correlation regions for the phase and amplitude disturbances induced by the turbulent atmosphere. Because of the smoothing, the mutual-coherence process can be sampled in v, t, $\underline{x}$, and $\underline{y}$ (with a sampling grain equal to the foremention correlation regions), rather than being retained as a continuous function.

Under the isoplanatic condition, these samples are related to the object, the atmospheric disturbances, and the shot noise as

$$\hat{\Gamma}_v(\underline{x}, \underline{x}+\underline{y}, t) = \Delta T \Delta v (\Delta x)^2 \, \Theta_v(\underline{y}/\lambda) \, \exp\{a_v(\underline{x}, t)+a_v(\underline{x}+\underline{y}, t)+j[b_v(\underline{x}, t)-b_v(\underline{x}+\underline{y}, t)]\}$$

$$+ N_v \Delta T \Delta v (\Delta x)^2 \, \Omega \delta_{\underline{0}, \underline{y}} + n_{v, t, \underline{x}, \underline{y}}, \tag{119a}$$

where

$\Theta_v(\underline{k})$ is the spatial Fourier transform of the intensity pattern of the object about optical frequency v

$\tilde{N}$ is the background radiation level

$a_v(\underline{x}, t)$ is the atmospherically induced log amplitude disturbance

$b_v(\underline{x}, t)$ is the atmospherically induced phase disturbance

$n_{v,t,\underline{x},\underline{y}}$ is the complex shot-noise variable.

We assume that a and b are jointly Gaussian processes, and that the $n_{v,t,\underline{x},\underline{y}}$ are independent complex Gaussian-noise variables. For ease of analysis, we suppose that the total received energy (mutual coherence process at zero displacement) is dominated by the background radiation. The variance of the shot-noise variables, which depends upon the total received energy, is then essentially independent of both the object and the atmospheric disturbances.

An estimate of the object may be either a full restoration of the intensity pattern or simply an estimate of a small set of parameters, perhaps the outline shape or dimensions of the object. In the case of a full restoration we need to know all of the complex values of $\Theta_v(\underline{k})$, whereas in the case of parameter estimates a few values may suffice. Indeed, we are often satisfied with only the magnitude of the transform at a few points. For example, in estimating the diameter of an object, one is often satisfied to determine the spatial frequency at which the magnitude of the spatial transform drops to some prescribed fraction of the zero-frequency component.

It is useful to separate the possible estimation problems into two categories, those that require only the amplitude of the spatial Fourier transform, and those that require both the amplitude and the phase.

Consider the estimation of the magnitude or phase of a particular $\Theta_v(\underline{k})$, and let us look at just the samples of Γ_v for displacement $\underline{y} = \lambda\underline{k}$. Furthermore, assume that these samples extend only over time. We shall now find the lower bounds to the variance for any estimate, and then demonstrate the receiver structures that approach these limits. With this understanding of the elementary form of the problem, we then consider the general case for which we may have available extra information in additional aperture coordinate, displacement, and optical-frequency samples.

We make one further approximation in order to shorten the problem, and treat the successive samples as being statistically independent. For the shot-noise components this is certainly valid, as the observation times are disjoint. It would be presumptuous, however, to suppose that atmospheric disturbances are independent, just because the samples are separated by the correlation time ΔT. In general we expect some smoothly decreasing degree of dependence as the separation between samples is increased.

Nevertheless, from our experience we believe that the results obtained under the independence assumption will usually reflect the behavior of the channel with sufficient accuracy for engineering considerations. The effect of the actual intersample dependence can usually be taken into account with

1. An effective signal-to-noise ratio which may be somewhat greater than that of each sample.

2. An effective number of independent samples that may be somewhat less than the value that we shall use, $N = T/\Delta T$ (T being the total duration of the observation).

For convenience, we denote the successive time samples of Γ_v as

$$r_i = \Gamma_v(\underline{x}, \underline{x}+\lambda\underline{k}, t_i)$$

$$= A^{1/2}\, e^{j\phi}\, e^{a_i+jb_i} + n_i, \tag{120}$$

where

$$A^{1/2} = \left|\Theta_v(\underline{k})\right|\, e^{2\bar{a}_v}$$

$$\phi = \text{phase angle of } \Theta_v(\underline{k})$$

$$a_i = a_v(\underline{x}, t_i) + a_v(\underline{x}+\lambda\underline{k}, t_i) - 2\bar{a}_v$$

$$b_i = b_v(\underline{x}, t_i) - b_v(\underline{x}+\lambda\underline{k}, t_i)$$

$$n_i = n_{v, t_i, \underline{x}, x+\lambda\underline{k}}. \tag{121}$$

Let us normalize the noise samples so that each component (real and imaginary) has unit variance

$$E[\mathrm{Re}\,(n_i)]^2 = E[\mathrm{Im}\,(n_i)]^2 = 1. \tag{122}$$

The parameter A is thus proportional to the squared magnitude of the spatial Fourier transform component. With the normalization of the noise, A is a measure of the average signal-to-noise ratio in the output samples.

In the succeeding analysis we frequently encounter the ensemble average values of e^{na_i} and e^{jnb_i}, which we denote as D_n and B_n (n an integer). Under the Gaussian assumption

$$D_n = \overline{e^{na}} = e^{n^2\sigma_a^2/2}$$

$$B_n = \overline{e^{njb}} = e^{-n^2\sigma_b^2/2}, \tag{123}$$

where σ_a^2 and σ_b^2 are the mean-square values of the log amplitude and phase disturbances. The mean values of $a_v(\underline{x}, t)$ were subtracted in the definition of a (Eq. 121), and absorbed into the definition of A in order that a_i have zero mean.

3.1 LOWER BOUND TO THE VARIANCE OF ANY UNBIASED AMPLITUDE ESTIMATE

The Cramer-Rao inequality gives as the smallest possible variance of any unbiased estimate $\hat{A}$.[13]

$$\text{Variance } \hat{A} \geq \frac{1}{E_r\left[\frac{\partial}{\partial A} \ln p(r_1, r_2 \ldots r_N/A, \phi)\right]^2}, \tag{124}$$

or equivalently

$$\text{Variance } \hat{A} \geq \frac{-1}{E_r\left[\frac{\partial^2}{\partial A^2} \ln p(r_1, r_2 \ldots r_N/A, \phi)\right]}, \tag{125}$$

where the expectation (denoted by the operator E_r) extends over the random variables r_i. The spatial phase ϕ is regarded as a known parameter. With N independent samples, this inequality becomes

$$\text{Variance } \hat{A} \geq \frac{1}{\sum_{i=1}^{N} E_r\left[\frac{\partial}{\partial A} \ln p(r_i/A, \phi)\right]^2} \tag{126}$$

or

$$\text{Variance } \hat{A} \geq \frac{-1}{\sum_{i=1}^{N} E_r\left[\frac{\partial^2}{\partial A^2} \ln p(r_i/A, \phi)\right]}. \tag{127}$$

The problem encountered in directly evaluating the C-R inequality is the complicated form of the conditional probability resulting from the mixture of normal and log-normal forms. We are forced to take a piecemeal approach to the evaluation, using different approximating techniques over various ranges of the parameter A.

Consider, first, the two asymptotic cases of very large, and very small values of A.

3.1.1 Very Strong Signal

When A is very large, we completely disregard the shot-noise component, thereby making each r_i a complex log-normal random variable. Taking the logarithm of each sample then reduces the problem to the familiar one of constant signal in added Gaussian noise. Application of the C-R inequality then yields

$$\frac{\text{Variance } \hat{A}}{A^2} \geq \frac{4\sigma_a^2}{N}. \tag{128}$$

3.1.2 Very Weak Signal

The opposite extreme of very poor signal-to-noise ratio is harder to work out. In Appendix B we derive an asymptotic expansion of the right-hand side of the inequality of (126). Under the condition that the phase variance is large ($B_n \ll 1$), we obtain the small-signal approximation

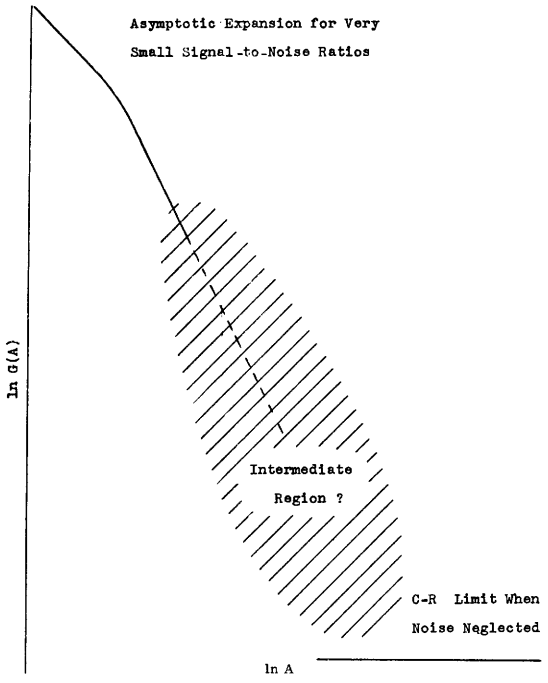

Fig. 18. Cramer-Rao lower bound for $\hat{A}$.

$$\frac{\text{Variance } \hat{A}}{A^2} \geq \frac{4}{N\left(D_1^2 B_1^2 A + D_2^2 A^2\right)}, \tag{129}$$

where only the first two significant terms of the power-series expansion of the denominator have been retained.

If we suppose that N (the number of independent observations) is the same in all cases, we can write

$$\frac{\text{Variance } \hat{A}}{A^2} \geq \frac{G(A)}{N},$$

where the function G(A) provides a convenient means of comparing the performance limitations. The general form of G(A) for the two extreme ranges of A is shown in Fig. 18 (log-log scales are employed).

The first result (inequality (128)) is valid for all values of A, but is not useful except for A large, as it reflects only the limitation caused by the turbulence, and ignores the effect of shot noise.

The other extreme case (inequality (129)), shows a variance which decreases inversely as A in the limit of small A. For larger values of A such that $A > D_1^2 B_1^2 / D_2^2$, the function changes to an inverse quadratic in A. It turns out that this is the essential behavior over a very large range of A, but does not necessarily follow from (128) because we simply ignored the higher order terms in the expansion.

3.1.3 Intermediate Signal

We fill in the intermediate region of the bound in two more steps.

a. Uniform Phase and Constant Amplitude Approximation

The continuation of the low-signal form (129) to higher values of A is obtained by the following approximation. First, we suppose that there is no fading and replace the term e^{a_i} in Eq. 120 by the factor $D_2^{1/2}$. This ensures that the same mean-square value of the signal component is retained. Furthermore, we suppose that the phase probability density is uniform over the closed interval 0 to 2π, which would seem to be reasonable when the variance of the phase is large. The C-R inequality can then be approximated as (see Appendix B).

$$\frac{\text{Variance } \hat{A}}{A^2} \geq \frac{16}{N\left[8D_2^2A^2+8D_2^3A^3+D_2^4A^4\right]}. \tag{130}$$

Only when the signal-to-noise ratio is quite large ($A > 1/D_2$) do the third- and fourth-order denominator terms give a significant contribution. Thus over a large range of A, the inequality (130) can be reduced simply to

$$\frac{\text{Variance } \hat{A}}{A^2} \geq \frac{2}{ND_2^2A^2}. \tag{131}$$

This inverse quadratic behavior is almost the same as that given by the second term of (129) (except for a factor of two). Indeed, we expect that (129) is the more accurate, since one of the approximations for (130) was the elimination of the fading.

The implications of the uniform-phase approximation must also be considered. We note that the expression (130) does not tend to a 1/A form when the signal is very weak, as predicted by the expansion of (129). The uniform-phase approximation is the root of this anomaly. It comes about because the mean component of each r_i is destroyed under a uniform-phase approximation. As we shall see eventually, the optimum receiver in the limit of very small values of A is one that treats this small mean value as a known signal in an added, zero-mean background, and ignores any information contained in the rest of the sample.

Admittedly, the uniform-phase approximation does not give a rigorous lower bound to the problem. It is our opinion, however, that the true Gaussian nature of the phase has an appreciable effect only when the signal is very weak and when the very small mean component in the signal can be exploited.

For larger values of A the cubic and fourth-order terms become significant, and the utility of the bound is reduced. Rather than worry too much about these terms, we turn instead to the last step in the bounding procedure.

b. Known Phase and Amplitude Approximation

A strict lower bound can also be obtained if we assume that both a_i and b_i are known to the receiver a priori but are still random. We then have a case of signal

in added Gaussian noise. The C-R inequality is easily evaluated to give

$$\frac{\text{Variance } \hat{A}}{A^2} \geq \frac{4}{A \sum_{i=1}^{N} e^{2a_i}}$$

which when averaged over a_i yields

$$\frac{\text{Variance } \hat{A}}{A^2} \geq \frac{4}{NAD_2}, \tag{132}$$

where we have exploited the well-known result that for a positive random variable x, $\overline{(1/x)} \geq (1/\bar{x})$.

The four pieces that approximate the C-R lower bound are summarized in Table 1. The form of this bound is sketched in Fig. 19. We divide the A axis into four regions. Beginning in region 1 where the signal level is very high, the performance is independent of the signal-to-noise ratio A. When A is somewhat smaller, the variance varies inversely as A (region 2). At still lower values (region 3) the behavior is an inverse quadratic. Finally, in region 4 the signal is extremely small, and the variance follows inversely as A.

3.2 RECEIVER STRUCTURES FOR AMPLITUDE ESTIMATION

Let us now look at various receiver structures that we can use in order to actually achieve performance either as good as or almost as good as the lower limits specified by the C-R inequality. We shall assume that the receiver has enough a priori knowledge regarding A to know the general region of operation (strong signal, intermediate signal or low signal).

3.2.1 Fringe-Tracking Receiver for Strong Signals

The first receiver to consider is the one that tracks the fringes in the interferometer. That is, it is able to obtain accurate measurements of the spatial amplitude and phase of the fringes in each coherence interval ΔT, without shot noise significantly distorting the result.

The log amplitude and phase of the complex samples r_i are conveniently expressed as the two complex components of $\ln r_i$.

The maximum-likelihood estimate for A follows immediately as

$$\hat{A}_{ML} = \exp\left[(2/N) \sum_{i=1}^{N} \text{Re } (\ln r_i)\right]. \tag{133}$$

This maximum-likelihood estimate for A has a bias

$$\overline{\hat{A}_{ML}} - A = A\left(e^{2\sigma_a^2/N} - 1\right). \tag{134}$$

When N is large, the bias becomes negligible. Moreover, we can remove the bias completely simply by dividing the estimate by $\left(e^{2\sigma_a^2/N} - 1\right)$, but the estimate is no longer maximum-likelihood.

The fractional mean-square error in the maximum-likelihood estimate is

$$\frac{\overline{[\hat{A}_{ML}-A]^2}}{A^2} = \left(1 - 2e^{2\sigma_a^2/N} + e^{8\sigma_a^2/N}\right). \tag{135}$$

When N is large enough that the error is small, 10% or less, the exponentials can be expanded to first order, and we have

$$\frac{\overline{[\hat{A}_{ML}-A]^2}}{A^2} \approx \frac{4\sigma_a^2}{N}. \tag{136}$$

This is identical to the C-R lower limit (128), and thus this amplitude estimate is said to be asymptotically efficient with N.

With noise present, the performance of the fringe-tracking receiver is naturally degraded. As long as the noise is small, we can approximate

$$\ln\left[1 + \frac{n}{A^{1/2}\, e^{a+j(b+\phi)}}\right] \approx nA^{-1/2}\, e^{-a-j(b+\phi)}. \tag{137}$$

The phase term $e^{-j(b+\phi)}$ only rotates the noise coordinates, and can be ignored, as far as the performance goes.

Each complex component of $\ln r_i$ then has an additional random-noise variable

$$\bar{A}^{1/2}\, e^{-a_i}\, \mathrm{Re}\,(n_i)$$

and

$$\bar{A}^{1/2}\, e^{-a_i}\, \mathrm{Im}\,(n_i). \tag{138}$$

These are uncorrelated with the phase and amplitude disturbances, and provided the error in the estimate is small (N sufficiently large), the resulting error is

$$\frac{\overline{[\hat{A}-A]^2}}{A^2} = \frac{4\left[\sigma_a^2 + D_{2/A}\right]}{N}. \tag{139}$$

The linear approximation to the logarithm holds only when n_i is quite small. Indeed, if $|n_i| \geq A^{1/2}\, e^{a_i}$, the second-order term exceeds the first-order term in the series

expansion (137), and the linear approximation is not justified.

The nonlinear noise effects are not nearly as disastrous as in the phase estimation problems, but a bias will be introduced into the estimate, and the performance will not be as good as that for the next receiver structure.

3.2.2 Square-Law Receiver

If we sample-average the squared magnitudes of the samples r_i, the ensemble average of the result is

$$\overline{R} = \overline{\frac{1}{N}\sum_{i=1}^{N} |r_i|^2} = AD_2 + 2, \tag{140}$$

where the factor 2 is a bias arising from the noise energy. An estimate

$$\hat{A} = \frac{\frac{1}{N}\sum_{1}^{N} |r_i|^2 - 2}{D_2} \tag{141}$$

is then unbiased, and has a fractional mean-square error of

$$\frac{\overline{[\hat{A}-A]^2}}{A^2} = \frac{1}{N}\left[\frac{D_4 - D_2^2}{D_2^2} + \frac{4}{D_2 A} + \frac{4}{D_2^2 A^2}\right]. \tag{142}$$

When the signal is very strong, $A > 4\left(D_4 - D_2^2\right)/D_2^2$. The error is independent of the signal strength and is approximately

$$\frac{\overline{[\hat{A}-A]^2}}{A^2} \approx \frac{1}{N}\left[\frac{D_4 - D_2^2}{D_2^2}\right] = \frac{1}{N}\left(e^{4\sigma_a^2} - 1\right). \tag{143}$$

The corresponding C-R limit is $4\sigma_a^2/N$. Thus the square-law receiver is in general not efficient whenever the signal level is high (region 1). In the case of very slight fading $\left(\sigma_a^2 \text{ small}\right)$ a first-order expansion of the exponential suffices, and we find that

$$\frac{\overline{[\hat{A}-A]^2}}{A^2} \approx \frac{4\sigma_a^2}{N}, \tag{144}$$

which is the same as that given by the C-R inequality in region 1.

When the signal is somewhat weaker, the inverse linear term dominates the error expression, and we have

$$\frac{\overline{[\hat{A}-A]^2}}{A^2} \approx \frac{1}{N}\left[\frac{4}{AD_2}\right] \qquad D_2 < A < 4\left[\frac{D_4 - D_2^2}{D_2^2}\right]. \tag{145}$$

This is identical to the limit given by the inequality (132), and the square-law receiver is thus efficient in region 2.

When A is very small, the fractional mean-square error behaves as

$$\frac{\overline{[\hat{A}-A]^2}}{A^2} \approx \frac{1}{N}\left[\frac{4}{A^2D_2^2}\right] \qquad A < D_2^{-1}. \tag{146}$$

This can be compared with approximations (130) and (132) for the C-R limits in region 3

$$\frac{1}{N}\left[\frac{4}{A^2D_2^2}\right] \qquad \text{(second term of asymptotic expansion)}$$

and

$$\frac{1}{N}\left[\frac{2}{A^2D_4}\right] \qquad \text{(a constant, b uniform, 0 to } 2\pi\text{)}.$$

If we suppose that the first limit (130) is the more accurate, we find that this square-law receiver can actually do as well as could ever by expected in region 3.

3.2.3 Crosscorrelation Receiver

We can make a slight modification to the square-law receiver which avoids the problem of noise bias. The bias must be subtracted from the sample average of the squared magnitude of the samples before we obtain the estimate $\hat{A}$. This number would either be known a priori or would need to be estimated, but by going to a crosscorrelation form of the receiver we can eliminate the average noise energy in the output. Suppose that the fringes formed in the interferometer are measured by two detectors. We then get pairs of samples which have an identical signal component but independent shot-noise variables. In a crosscorrelation of these samples, the noise products then tend to zero. Because of the energy division, the signal levels and the variance of the shot noise are half the value for a single detector. Normalizing to unit variance of the noise components yields sample pairs of the form

$$r_i = \frac{A^{1/2}\, e^{a_i + j(b_i+\phi)}}{\sqrt{2}} + n_i$$

$$v_i = \frac{A^{1/2}\, e^{a_i + j(b_i+\phi)}}{\sqrt{2}} + m_i. \tag{147}$$

The ensemble average of the sample crosscorrelation product is

$$\overline{\frac{1}{N}\sum_{i=1}^{N} r_i v_i^*} = \frac{AD_2}{2}, \tag{148}$$

and thus an unbiased estimate can be obtained as

$$\hat{A} = \frac{2}{D_2}\frac{1}{N}\sum_{i=1}^{N} r_i v_i^*. \tag{149}$$

The fractional mean-square error in such an estimate is

$$\frac{\overline{[\hat{A}-A]^2}}{A^2} = \frac{1}{N}\left[\frac{D_4 - D_2^2}{D_2^2} + \frac{8}{AD_2} + \frac{16}{A^2 D_2^2}\right]. \tag{150}$$

As should be expected, when the signal level is very high the variance in the estimate is the same as with the square-law receiver. In the two other regions the behavior is functionally the same as for the square-law receiver, but we suffer a penalty, in that A must be twice as large in order to achieve the same results. That is, we forfeit a factor of 2 (3 dB) in the effective incident light flux. Nevertheless, when the signal-to-noise ratio is poor one is vulnerable to a gross error with the square-law receiver, unless the noise bias is known very closely.

3.2.4 Signal Integrator

In order to attain the very small signal performance predicted by the C-R inequality of (129), we must employ one final receiver form. This is a receiver that considers the residual mean component in each sample r_i as a known signal imbedded in a zero-mean random disturbance. If we form a sample average of the r_i, we obtain a random variable R that has an ensemble-average value

$$\begin{aligned}\overline{R} &= \frac{1}{N}\sum_{i=1}^{N}\overline{r_i} \\ &= A^{1/2} e^{j\phi} D_1 B_1.\end{aligned} \tag{151}$$

An estimate $\hat{A}$ can then be formed as

$$\hat{A} = \frac{1}{D_1^2 B_1^2}\left|\frac{1}{N}\sum_{i=1}^{N} r_i\right|^2. \tag{152}$$

The ensemble average of this estimate is

$$\overline{\hat{A}} = A\left[1 + \frac{1}{N}\left[\frac{D_2}{B_1^2 D_1^2} - 1\right]\right] + \frac{2}{ND_1^2B_1^2}. \tag{153}$$

A bias exists in the estimate, but it tends to zero with increasing N. Moreover, it can be removed by first subtracting the noise contribution $2/ND_1^2B_1^2$, and then dividing by $1 + (1/N)\left(D_2/B_1^2D_1^2 - 1\right)$.

The evaluation of the mean-square error, though straightforward, is extremely tedious. After going through considerable algebraic manipulations, and elimination of higher order terms of 1/N which are negligible when the final error is small, we obtain

$$\frac{\overline{[\hat{A}-A]^2}}{A^2} \approx \frac{1}{N}\left[\frac{4}{AD_1^2B_1^2} + \frac{2D_2}{D_1^2B_1^2} + \frac{2D_2B_2}{D_1^2B_1^2} - 4\right]. \tag{154}$$

Moreover, in cases of practical interest, B_1 and B_2 are both very small, and the expression reduces to

$$\frac{\overline{[\hat{A}-A]^2}}{A^2} \approx \frac{1}{N}\left[\frac{4}{AD_1^2B_1^2} + \frac{2D_2}{D_1^2B_1^2}\right]. \tag{155}$$

For very small values of A the second term is negligible, and

$$\frac{\overline{[\hat{A}-A]^2}}{A^2} \approx \frac{1}{N}\frac{4}{AD_1^2B_1^2} \qquad A < \frac{2}{D_2}, \tag{156}$$

which is identical to the asymptotic result for the C-R inequality (region 4).

Throughout the range $A > D_1^2B_1^2/D_2^2$ the integrating receiver is suboptimum, and indeed when $A > 2/D_2$ the performance tends to saturate at

$$\frac{\overline{[\hat{A}-A]^2}}{A^2} \approx \frac{1}{N}\frac{2D_2}{D_1^2B_1^2}. \tag{157}$$

This is far greater than the saturation values for both the fringe-tracking receiver (Eq. 136) and the square-law or crosscorrelator receiver (Eq. 143). The integrator receiver considers only the small mean component as useful signal, and regards all the rest as noise. Even when the shot noise is absent, the tremendous difference between this mean component and the rest of the signal creates a very small effective "signal-to-noise ratio."

Although the integrating receiver is inferior at the high values of A, it is interesting to note that as the signal becomes weaker, we eventually reach a point where the linear behavior of the variance with respect to A triumphs over the noise-enhancement

Table 1. Cramer-Rao lower bound to variance of $\hat{A}$.

CRAMER - RAO LOWER BOUND Variance $\hat{A}/A^2 \geq (1/N)\, G(A)$	
REGION 1 noise = 0 strict lower bound for all A	$G_1(A) = 4\sigma_a^2$
REGION 2 a,b, known strict lower bound for all A	$G_2(A) = \dfrac{4}{AD_2}$
REGION 3 a constant b uniform approximation to bound	$G_3(A) = \dfrac{16}{8D_2^2A^2+8D_2^3A^3+D_2^4A^4}$
REGION 4 signal very weak asymptotic approximation	$G_4(A) = \dfrac{4}{D_1^2 B_1^2 A + D_2^2 A^2}$

Table 2. Receiver characteristics for $\hat{A}$.

RECEIVER CHARACTERISTICS $\overline{[\hat{A} - A]^2}/A^2 = (1/N)\tilde{G}(A)$	
$\tilde{G}_1(A) = 4\left[\sigma_a^2 + D_2/A\right]$	FRINGE TRACKER weak noise
$\tilde{G}_2(A) = \dfrac{D_4-D_2^2}{D_2^2} + \dfrac{4}{AD_2} + \dfrac{4}{A^2D_2^2}$	SQUARE LAW noise power known apriori
$\tilde{G}_3(A) = \dfrac{D_4-D_2^2}{D_2^2} + \dfrac{8}{AD_2} + \dfrac{16}{A^2D_2^2}$	CROSS-CORRELATOR no knowledge of noise
$\tilde{G}_4(A) = \dfrac{4}{AD_1^2B_1^2} + \dfrac{2D_2}{D_1^2B_1^2}$	INTEGRATOR

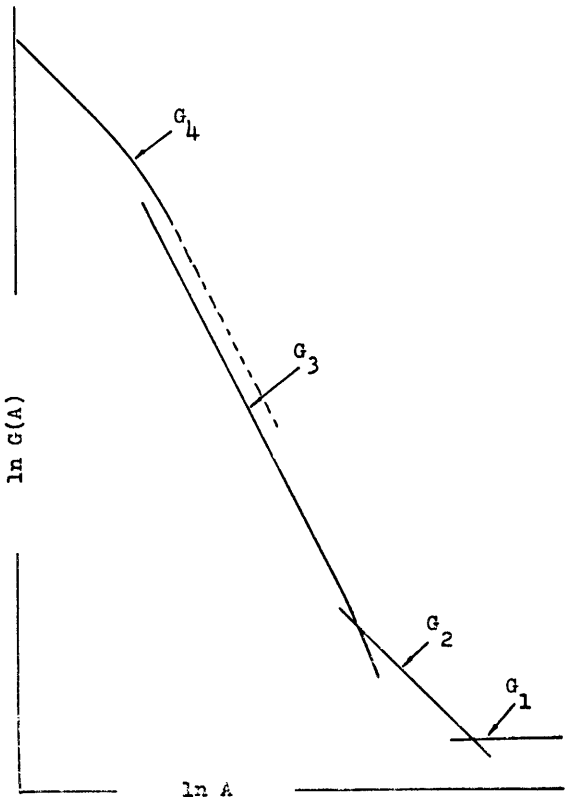

Fig. 19. C-R lower bound for $\hat{A}$.

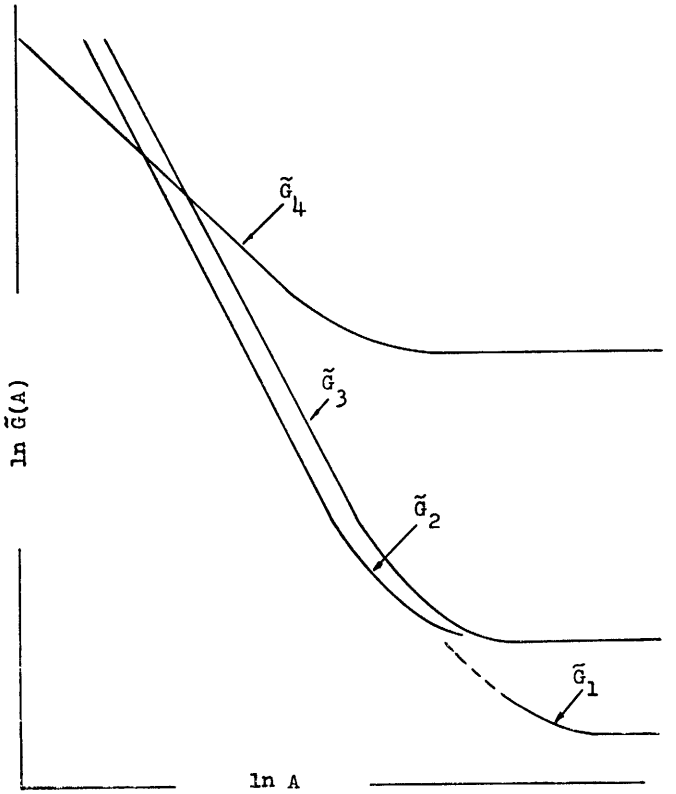

Fig. 20. Receiver characteristics.

characteristic of the square-law operation.

The performance results for the three receiver forms are summarized in Table 2, and can be compared with the Cramer-Rao lower limits of Table 1. The general functional forms of the various error expressions are plotted in Fig. 20.

3.3 LOWER BOUND TO THE VARIANCE OF ANY UNBIASED PHASE ESTIMATE

In an almost identical manner, we can derive a lower bound to the variance in the phase estimate ϕ.

3.3.1 Strong Signal

When the signal is very strong, we can discard the noise terms and thus obtain the lower bound in region 1.

$$\text{Variance } \hat{\phi} \geq \frac{\sigma_b^2}{N}. \tag{158}$$

3.3.2 Very Weak Signal

At the other extreme of very weak signal (region 4) we again make an expansion of the right-hand side of the C-R inequality where the parameter A is now considered to be known. Thus the asymptotic form of the lower bound becomes (Appendix B, section B.3)

$$\text{Variance } \hat{\phi} \geq \frac{1}{N A D_1^2 B_1^2}. \tag{159}$$

3.3.3 Intermediate Signal Level: Known Channel Phase and Amplitude Approximation

The intermediate region 2 can likewise be evaluated in a manner similar to that used in the amplitude-estimation problem. We assume that a and b are known to the receiver. Conditional on this knowledge, the C-R inequality is simply

$$\text{Variance } \hat{\phi} \geq \frac{1}{\sum_{i=1}^{N} A e^{2a_i}}. \tag{160}$$

An average over the a_i then yields

$$\text{Variance } \hat{\phi} \geq \frac{1}{NAD_2}. \tag{161}$$

The intermediate behavior in region 3 is the most difficult to obtain. We strongly

suspect that when the phase variance is large there is a severe threshold effect. That is, there seems to be little intermediate region. Provided the signal dominates the noise, a relatively good phase estimate is possible. As soon as the noise is dominant, however, only the residual mean component of the signal is of use in phase estimation, and we operate in region 4 with the much larger variance given by (159).

3.3.4 Noisy Phase Reference and Constant Amplitude

We can derive a lower bound to the variance in the estimate of the phase difference between two signals that suffer the same atmospheric disturbance but have independent added noises. This bound will be useful later when we consider a procedure that forms a phase estimate by sequentially estimating the phase difference between pairs of neighboring spatial frequencies.

Let us suppose that in addition to the samples r_i we are also given a set of noisy phase reference samples v_i of the form

$$v_i = A^{1/2} e^{a_i + jb_i} + m_i, \tag{162}$$

where m_i is an independent noise voltage having the same mean-square value as n_i. The phase ϕ is then the phase that would exist between the samples r_i and v_i in the absence of the noise voltages. As in section 3.1.2 we shall let b_i be uniformly distributed, and suppose that there is no fading replacing e^{a_i} by $D_2^{1/2}$.

In Appendix B (sec. B.4) we show that the error in the differential phase estimate is

$$\text{Variance } \hat{\phi} \geq \frac{8}{N\left(4D_2^2A^2 + 4D_2^3A^3 + D_2^4A^4\right)}. \tag{163}$$

The results of the last four discussions are summarized in Table 3, and the form of the bound is sketched in Fig. 21.

As in the amplitude estimation case, the dependence upon the signal strength A is divided into four regions. When A is very small, the dependence is inverse with A, reflecting the fact that the receiver considers only the mean component in the samples. At higher values of A, we find that the performance is under-bounded by an inverse quadratic form. This form was obtained by assuming that a noisy phase reference signal was available. When we consider receiver structures, we shall find that such a signal is obtained by using a second interferometer tuned to a slightly different spatial frequency, but occupying almost the same two aperture correlation areas. The error in estimating the phase difference between the two spatial frequencies then follows the form of this quadratic portion of the bound when we use a crosscorrelation type of receiver.

As we shall see eventually, the bound in region 2 reflects the behavior of a receiver that tracks the phase of the fringes and in which the noise is so weak that it simply adds

linearly to the phase-tracking signal. Finally, in region 1 we have the performance of a receiver that extracts a perfect phase measurement so that the only disturbance that must be overcome is the random fluctuations in this phase caused by the atmosphere.

3.4 RECEIVER STRUCTURES FOR PHASE ESTIMATION

Almost the same three receiver structures that were found to be optimum in the amplitude estimation problem apply also to phase estimation; that is, a fringe tracker when the signal strength is high, a crosscorrelator for intermediate signal levels, and an integrator when the signal strength is very weak.

3.4.1 Fringe Tracker

When the noise is small the instantaneous phase of the fringes can be accurately measured, and a phase estimate formed as

$$\hat{\phi} = \frac{1}{N} \sum_{i=1}^{N} \text{Im } (\ln r_i). \tag{164}$$

When the noise is completely negligible, this estimate is, in fact, maximum-likelihood, and has a mean-square error

$$[\hat{\phi}-\phi]^2 = \frac{\sigma_b^2}{N}. \tag{165}$$

This is the same as the C-R limit of (158). As long as the noise is weak and a linear expansion of the logarithmic term is justified, the variance of an estimate based on noisy measurements is

$$[\hat{\phi}-\phi]^2 = \frac{1}{N}\left[\sigma_b^2 + \frac{D_2}{A}\right], \tag{166}$$

where, as in the amplitude estimation problem, we have assumed that N is sufficiently large that the error is already small (10% or less).

The effect of the nonlinear interactions of the noise are much more serious in the phase-estimation problem than in amplitude estimation. In order to exploit the zero-mean behavior of the phase disturbance, the phase cannot be measured in simply a modulo 2π representation; rather, the full value must be retained. If an instantaneous noise sample is larger than the signal component, the phasor r_i may appear to encircle the origin, and an anomalous jump of 2π rad may appear in the output phase-tracking voltage. This anomaly generates a gross error in the final phase estimate, as much as π rad if it occurs near the middle of the record.

For this reason, the phase-tracking system is reliable only when the signal-to-noise ratio is above a threshold value. This is familiar in communication engineering as the

anomaly problem inherent in nonlinear modulation; for example, the "click" problem in frequency and phase modulation.

3.4.2 Integrator Receiver

At the other extreme of very small signal strength, we again find that a receiver that considers only the mean component in the signal is optimum, and we form our estimate as

$$\hat{\phi} = \text{Phase}\left(\frac{1}{N}\sum_{i=1}^{N} r_i\right). \tag{167}$$

When the ensemble average value of the r_i and the measured average are fairly close (N large), the phase error is approximately

$$[\hat{\phi}-\phi] \approx \frac{\left|\frac{1}{N}\sum_{i=1}^{N} r_i - \bar{r}\right|}{r} \tag{168}$$

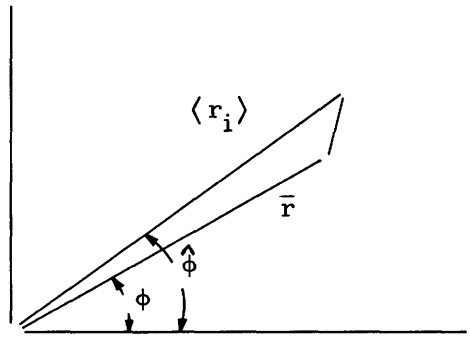

The mean-square value then is

$$\overline{[\hat{\phi}-\phi]^2} \approx \frac{1}{N}\left[\frac{D_2 - B_1^2 D_1^2}{B_1^2 D_1^2} + \frac{2}{AB_1^2 D_1^2}\right]. \tag{169}$$

Again, under the assumption that σ_b^2 is large, (169) becomes simply

$$\overline{[\phi-\phi]^2} \approx \frac{1}{N}\left[\frac{D_2}{B_1^2 D_1^2} + \frac{2}{AB_1^2 D_1^2}\right]. \tag{170}$$

When the signal is weak we obtain

$$\overline{[\hat{\phi}-\phi]^2} \approx \frac{1}{N} \frac{2}{AB_1^2 D_1^2}, \qquad A < \frac{2}{D_2}. \tag{171}$$

This differs by only a factor of 2 from the C-R limit (159). Our approximation probability overestimates the phase error by just this factor of 2, since only one of the orthogonal components of the difference $(1/N) \sum_{i=1}^{N} r_i - \overline{r_i}$ contributes to the phase error. Thus it appears that for small values of A, the integrator is asymptotically efficient with increasing N.

At high values of A ($A > 2/D_2$), when the shot-noise becomes insignificant the error saturates as

$$\overline{[\phi-\phi]^2} = \frac{1}{N} \frac{D_2}{D_1^2 B_1^2}. \tag{172}$$

This is much larger than the saturation level for the phase-tracking system which achieves the C-R limit. This is due to the zero-mean component which remains in the signal and acts just as if it were a large noise voltage.

3.4.3 Crosscorrelator Receiver

Between the threshold values of A, below which the fringe tracker flounders, and the very small values of A where we know an integrator is optimum, is the last region that we must study. We know from our C-R limit that nothing better than $1/A^2$ behavior will be possible. To even obtain this bound, we had to assume that an additional noisy phase reference signal was available and, with only the output of a single interferometer available, it would seem impossible to find anything better than the integrator receiver, once the signal level drops below the threshold value.

It seems inconceivable, however, that we would ever want an estimate of the phase of only a single spatial Fourier component in the object. Certainly, if we attempt to reconstruct a full picture we need all of the Fourier components. It is then reasonable to suppose that we would have available the outputs of a number of interferometers tuned to different spatial frequencies.

Suppose then that we look at two simultaneous sets of samples r_i and v_i of the form

$$r_i = A_1^{1/2} e^{j\phi_1} e^{a_i + jb_i} + n_i$$

$$v_i = A_2^{1/2} e^{j\phi_2} e^{c_i + jd_i} + m_i, \tag{173}$$

where n_i and m_i are independent shot-noise terms (independent because of orthogonality of different spatial frequencies). We shall assume that the atmospheric disturbances $a_i + jb_i$ and $c_i + jd_i$ are partially correlated. That is, the two interferometers share part

of the same aperture space. If we now crosscorrelate the two sets of data, we obtain a random variable R with an ensemble average value

$$\overline{R} = \frac{1}{N}\sum_{i=1}^{N} \overline{r_i \overset{*}{v}_i} = A_1^{1/2} A_2^{1/2} \left[\overline{e^{a_i + c_i}\, e^{j(b_i - d_i)}}\right] e^{j(\phi_1 - \phi_2)}. \tag{174}$$

This average complex crosscorrelation has a phase that is simply the phase difference between the two spatial frequency components. An estimate of this phase difference $\Delta_{1,2} = \phi_1 - \phi_2$ can be made:

$$\hat{\Delta}_{1,2} = \text{Phase of } \frac{1}{N}\sum_{i=1}^{N} r_i \overset{*}{v}_i. \tag{175}$$

When N is large (error is small) we approximate the error in the same manner as in section 3.4.2 and obtain

$$\overline{\epsilon_{1,2}^2} = \overline{[\hat{\Delta}_{1,2} - \Delta_{1,2}]^2} \approx \frac{\overline{(R - \overline{R})^2}}{(\overline{R})^2}. \tag{176}$$

This is the same technique that was used to estimate the error in the integrator receiver, and we find that

$$\overline{\epsilon_{1,2}^2} = \frac{1}{N}\left[\frac{\overset{*}{D}_2}{\overset{*}{D}_1^2 \overset{*}{B}_1^2} - 1 + \frac{2\overset{*}{D}_2 (A_1 + A_2)}{\overset{*}{D}_1^2 \overset{*}{B}_1^2 A_1 A_2} + \frac{4}{\overset{*}{D}_1^2 \overset{*}{B}_1^2 A_1 A_2}\right] \tag{177}$$

where

$$\overset{*}{D}_n = \overline{e^{n(a_i + c_i)}}$$

and (178)

$$\overset{*}{B}_n = \overline{e^{jn(b_i - d_i)}}$$

If we regard $\sqrt{A_1 A_2}$ as the effective signal strength, we can see again that there are essentially three different behavioral domains. When the signal strength is very large, noise is negligible, and the phase error goes as

$$[\epsilon_{1,2}]^2 = \frac{1}{N}\left[\frac{\overset{*}{D}_2}{\overset{*}{D}_1^2\overset{*}{B}_1^2} - 1\right]. \tag{179}$$

If the phases b_i and d_i are uncorrelated, their difference will be large and the denominator term $\overset{*}{B}_1$ will be extremely small. The phase estimate is then very poor, even when noise is absent, and it is of the same order as for the integrator receiver (172). Only the mean components of r_i and v_i are used by the receiver.

If, however, we choose two neighboring spatial frequencies, the aperture displacements are almost the same, and we can use almost the same pair of aperture openings. The phase disturbances b_i and d_i will now be strongly correlated. Thus $\overset{*}{B}_1$ will be of the order of unity, and the phase variance will be much smaller. (See sketch below.)

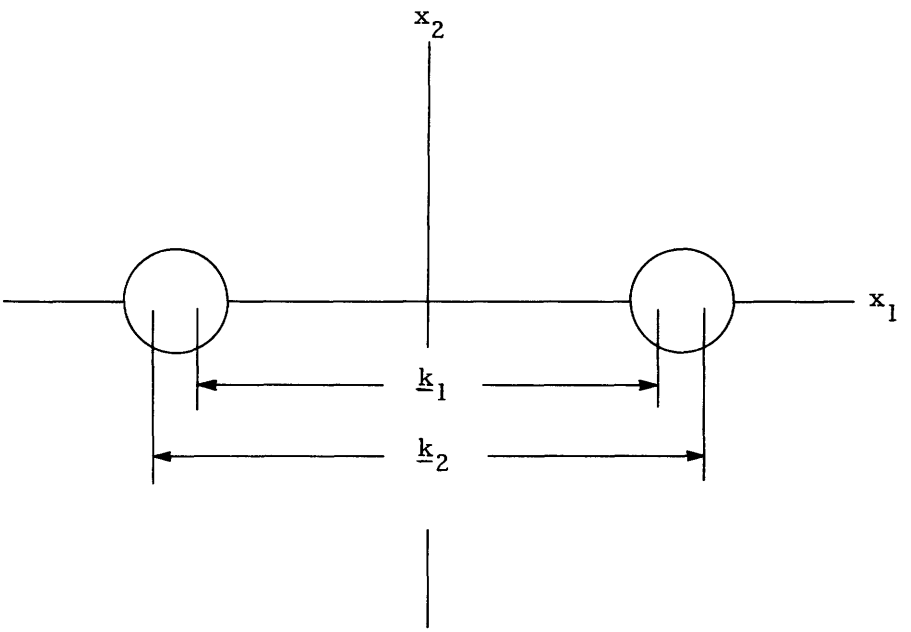

At somewhat lower values of effective signal strength the noise begins to influence the result, and the behavior is inversely with signal strength (assuming $A_1 \approx A_2$), and we have

$$\overline{[\epsilon_{1,2}]^2} = \frac{1}{N}\,\frac{2\overset{*}{D}_2(A_1+A_2)}{\overset{*}{D}_1^2\overset{*}{B}_1^2 A_1 A_2}. \tag{180}$$

Finally, when the signal strength is very weak, we have an inverse quadratic behavior

$$\overline{[\epsilon_{1,2}]^2} = \frac{1}{N} \frac{4}{D_1^{*2} B_1^{*2} A_1 A_2}. \tag{181}$$

When the phases b_i and d_i are strongly correlated the result is similar to that predicted by the C-R inequality (163).

Thus far, however, we have only considered the estimation of the phase difference between pairs of spatial frequencies. We can generate the absolute phase of the transform by an iterative procedure. Starting with the zero-frequency component (which must always have a zero phase), we make a set of differential phase estimates between pairs of neighboring spatial frequencies. These differential estimates are then summed to give the composite estimate. That is,

$$\text{Phase } \Theta_v(\underline{k}) = \hat{\phi}_v(\underline{k}) = \Delta_{0,1} + \Delta_{1,2} + \Delta_{2,3} \cdots + \Delta_{M-1,M}, \tag{182}$$

where M is the total number of iterations.

Everywhere but in region 1, the errors in these estimates are due primarily to the shot-noise terms, and hence all the differential errors ϵ_{ij} will be uncorrelated. The total mean-square error is the sum of all of the mean-square differential errors given by Eq. 178. That is,

$$\overline{[\hat{\phi}_v(\underline{k}) - \phi_v(\underline{k})]^2} = \sum_{m=1}^{M} \overline{[\epsilon_{m-1,m}]^2}. \tag{183}$$

If we assume that all successive spatial frequency pairs are separated by the same amount, the amplitude and phase correlation terms will all be about the same. Furthermore, if the amplitude spectrum of the spatial transform is fairly uniform (all A_m about the same), the successive errors will be of the same order, and the resultant phase error in $\Theta_v(\underline{k})$ will go as $M\overline{[\epsilon]^2}$, where M is proportional to the magnitude of $\underline{k}$, and is given by

$$M = \frac{\lambda k}{\Delta d}, \tag{184}$$

where Δd is the difference in displacement for neighboring interferometers.

There will be some best choice for the interspatial frequency spacing Δd. When we choose a very small value of Δd, then the phase disturbances will be strongly correlated, but M will be large. Likewise, if we use a course spacing, M will be small, but the differential errors will be large.

The mean-square errors for the three receiver forms, fringe tracker, crosscorrelator, and integrator are summarized in Table 4 and the functional form is sketched in Fig. 22. The general conclusion is that when the noise is negligible, a fringe tracker is optimum and achieves the Cramer-Rao limit. At the other extreme, very weak signal,

Table 3. Cramer-Rao lower bound to variance $\hat{\phi}$.

CRAMER - RAO LOWER BOUND Variance $\hat{\phi} \geq (1/N)\ G(A)$	
REGION 1 noise = 0 strict lower bound for all A	$G_1(A) = \sigma_b^2$
REGION 2 a,b known strict lower bound for all A	$G_2(A) = \dfrac{1}{AD_2}$
REGION 3 a known b uniform noisy reference	$G_3(A) = \dfrac{8}{4D_2^2A^2 + 4D_2^3A^3 + D_2^4A^4}$
REGION 4 weak signal asymptotic approximation	$G_4(A) = \dfrac{1}{D_1^2 B_1^2 A}$

Table 4. Receiver characteristics for $\hat{\phi}$.

RECEIVER CHARACTERISTICS $\overline{[\phi - \phi]^2} = (1/N)\ G(A)$	
$\tilde{G}_1(A) = \sigma_b^2 + D_2/A$	FRINGE TRACKER strong signal only
$\tilde{G}_2(A) = \dfrac{D_2^*}{D_1^{*2}B_1^{*2}} - 1 + \dfrac{4D_2^*}{AD_1^{*2}B_1^{*2}} + \dfrac{4}{A^2D_1^{*2}B_1^{*2}}$	CROSS-CORRELATOR differential phase estimate $A_1 = A_2 = A$
$\tilde{G}_3(A) \approx M\ G_2(A)$	COMPOSITE PHASE ESTIMATE M iterations where $M \sim \lvert\underline{k}\rvert$
$\tilde{G}_4(A) = \dfrac{1}{AD_1^2B_1^2} + \dfrac{D_2}{D_1^2B_1^2}$	INTEGRATOR

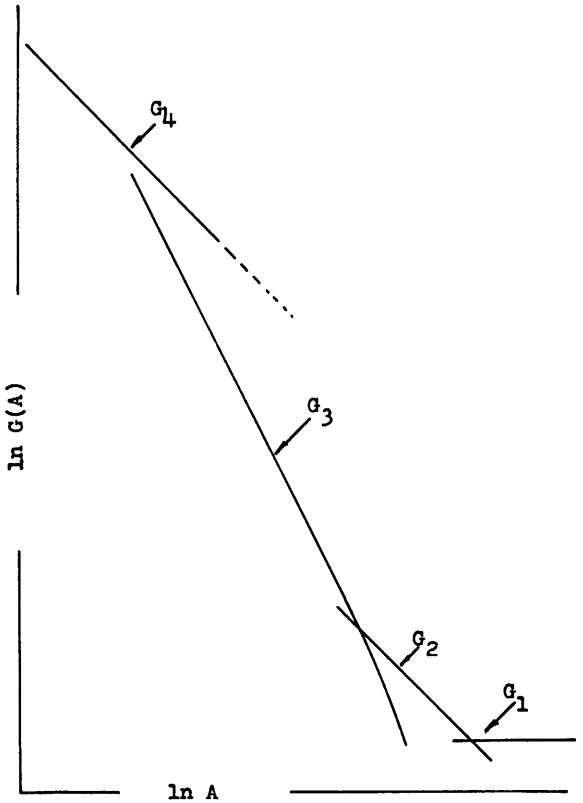

Fig. 21. C-R lower bound for $\hat{\phi}$.

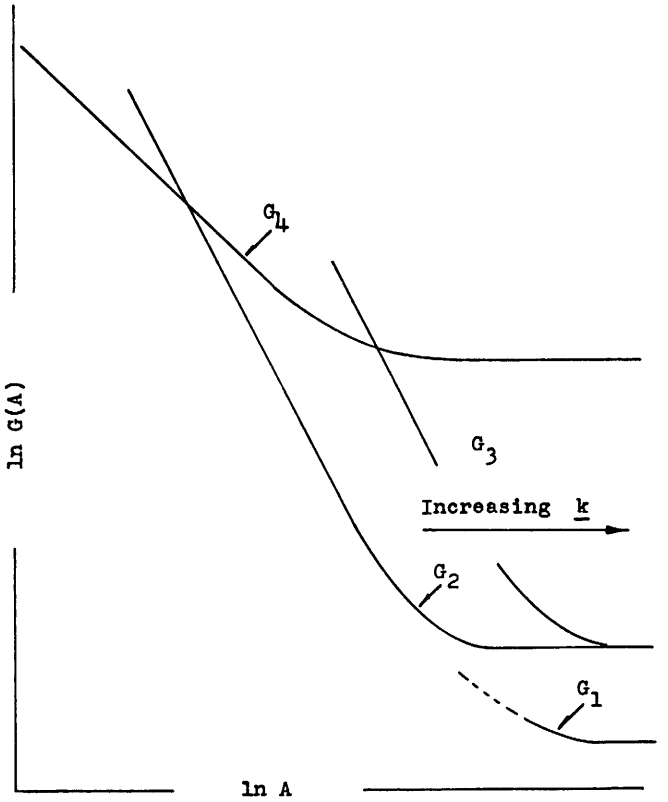

Fig. 22. Receiver characteristics.

the integrator receiver is asymptotically efficient. In the intermediate region the crosscorrelator receiver is best. Note, however, that increasing values of spatial frequency tend to shift this section of the performance curve upward, because of the increased number of iterations that are required. This tends to increase the value of A that determines the choice of the integrator or crosscorrelator receivers. Indeed, if $\lambda\underline{k}$ is large enough, it would appear that the crosscorrelator is no longer useful, and we use either the fringe tracker or integrator, depending upon the strength of the signal-to-noise ratio relative to the threshold value.

We should also note that the iteration technique may flounder when there is a gap in the spatial transform of the object.

3.5 INTERPRETATION OF RESULTS

3.5.1 Extension to Samples in Other Variables

We have dealt entirely with time samples of the mutual-coherence process. We now want to extend our results to the general case in which we have samples in other domains. When we have additional samples for aperture position, these samples are essentially independent, and should be treated in the same manner as the time samples. That is, we should simply integrate across both time and space when the signal level is very low, take square magnitudes and then integrate when the signal level is in the intermediate region, and average the phase and log amplitude when the signal-to-noise ratio is very high.

If we know that the object has essentially the same pattern over a broad range of wavelengths, or we want the color-averaged pattern, we treat the optical-frequency samples in the same manner.

If a full picture of the object is required, then we must estimate each spatial-frequency component from the corresponding displacement samples. The interdependence between samples of different spatial frequency can be exploited to some extent. For example, our iterative phase-estimation procedure uses such statistical dependencies. We also suspect that a similar crosscorrelation procedure would aid in estimating the amplitude of a weak spatial-frequency component if we have nearby a strong component that in effect could be used as a channel phase-reference signal.

3.5.2 Numerical Examples

Thus far, our results are still couched in the parameters A, B_n, and D_n. In order to assess the applicability of the estimating structures that we have obtained, we turn now to consider practical values of these parameters. Let us consider Fig. 20, which describes the mean-square error for various receiver forms in estimating the magnitude of the spatial transform. As an example, suppose the variances of the log-amplitude fading and the phase processes are $\sigma_a^2 \approx 0.5$ and $\sigma_b^2 \approx 50$ rad^2. These values were found typical for a horizontal 4.5 km path (see Section IV). With these values, the curve of

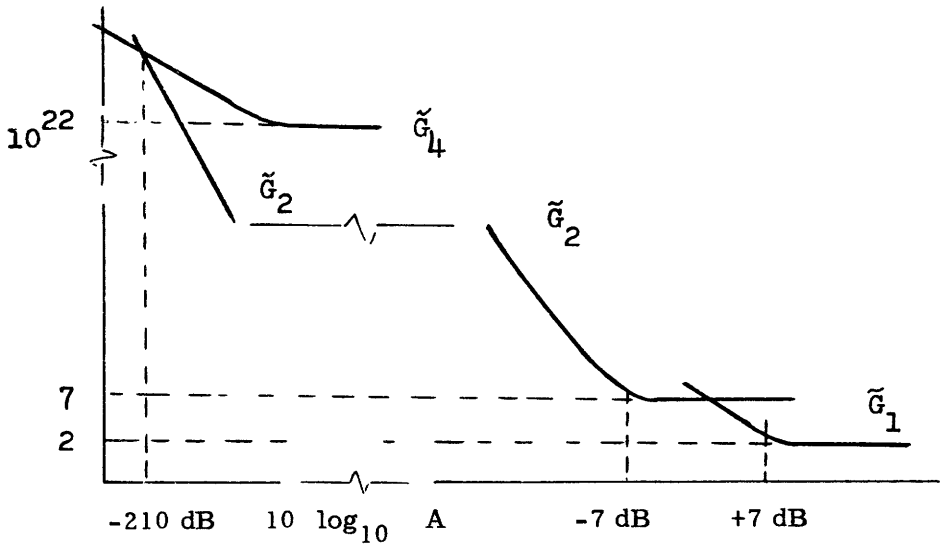

Fig. 23. Receiver characteristics.

Fig. 20 takes the form shown in Fig. 23.

The most immediate reaction to Fig. 23 is the extremely large range over which region 3 seems to apply. Over more than a 200-dB spread, it appears that square-law (or crosscorrelator) receivers would be best.

In order to appreciate this figure, we must have some idea of the order of magnitude of signal-to-noise ratio to be expected. Consider, for example, the Sun, which has an approximate intensity level of

$$1.8 \times 10^{-1} \text{ W/(cm)}^2 \text{ sterad A°}.$$

For typical atmospheric parameters, let us suppose

$$\Delta x^2 = 1 \text{ (cm)}^2 \quad (10^{-4} \text{ (m)}^2)$$

$$\Delta T = 1 \text{ msec} \quad (10^{-3} \text{ sec})$$

$$\Delta v = 50 \text{ A°}.$$

We would then have incident on our detector approximately 9×10^{-3} J/sterad. Since the energy per photon is approximately 10^{-19} J, this would be detected as 9×10^{-16} photons/sterad, and within just the diffraction-limited disk for a 1-cm aperture (0.25×10^{-12} sterad), the resultant photon count would be $\sim 2 \times 10^8$ photons.

For 10% quantum efficiency this becomes 10^7 photoelectrons. If the mean-square value of the fringes is approximately 10% of the average squared signal level, we end up with a signal-to-noise ratio of the order of 10^6, or 60 dB.

From Fig. 23 we see that this value falls in region 1, in which a fringe-tracking receiver would be best. For objects that reflect sunlight, such as the Moon, the

intensity level drops by a factor of $\sim 10^7$ (70 dB). Under the same conditions as before, this puts our signal-to-noise ratio down to approximately -10 dB, well within the region for the square-law receiver.

3.5.3 Comparison with Existing Techniques

We shall now discuss briefly the comparison of the preceding receiver structures with two existing techniques.

a. Long-Exposure Photography

The first of these is the technique of long-exposure photography followed by inverse filtering. This long-exposure technique is, in essence, an integration of the mutual-coherence process in both time and space over many correlation regions. Thus it is a realization of the receiver structure whose performance is denoted by $\tilde{G}_4$ in Figs. 20 and 22. As we can see from our recent results, for many objects this technique is quite inferior to the square-law and tracking receivers. It does possess many practical advantages, however, probably the most important being the ease of implementation. All of the integration can be done on a single plate, and many spatial frequencies can be detected simultaneously.

b. Hanbury Brown and Twiss Intensity Interferometry

Another technique for estimating the amplitude of the spatial-frequency components, is by correlating the intensity of the field at two points.[11,12] For Gaussian processes, the fourth- and second-order moments are conveniently related. Thus, from knowledge of the fourth-order moment, the second-order or mutual-coherence function can be determined. The main disadvantage with this technique is that large detector bandwidths are required if we are to recover any significant amount of the intensity fluctuation in the light. This detector bandwidth turns out to be the limiting factor, the bandwidth of the light itself being of less significance. It is interesting to compare the performance of this scheme with that for the square-law processor. Given that both schemes operate within the correlation bandwidth Δv, with aperture areas Δx^2, the ratio of mean-square errors turns out to be roughly

$$\frac{\overline{|\epsilon|^2}_{\text{square law}}}{\overline{|\epsilon|^2}_{\text{Brown and Twiss}}} \quad \frac{BW}{(\Delta v)^2},$$

where B is the bandwidth of the two detectors employed in the intensity correlation, and W is the bandwidth of the atmospheric fluctuations. Generally the product BW is much less than $(\Delta v)^2$, and the Brown and Twiss method would be inferior. We assumed, however, that the receiving areas were matched to the correlation area Δx^2. If the entire available aperture area is A, the signal-to-noise ratio in each detector output would be

increased by the factor $A/\Delta x^2$, with the result that the mean-square error for the Brown and Twiss method would be reduced by the factor $[\Delta x^2/A]^2$. On the other hand, with the square-law receiver, simply increasing the area does nothing to the mean-square error unless we employ parallel processing of the aperture samples. In this case, the error decreases by the factor $\Delta x^2/A$, which is the reciprocal of the number of essentially independent spatial samples. Thus the Brown and Twiss system is able to make more efficient use of the aperture. Nevertheless, because of the great disparity between $(\Delta v)^2$ and BW, the system still is inferior to square-law processing of the mutual-coherence samples unless the aperture is very large.

IV. CHANNEL MEASUREMENTS

An experimental investigation was conducted in order to measure some of the properties of the phase and amplitude disturbances induced by the turbulent atmosphere which play a part in the high-resolution imaging problem. The purpose of these measurements was not only to obtain channel data but, perhaps more important, to gain practical insight, appreciation, and respect for the turbulent atmosphere as a channel and for the problems of designing equipment for use on this channel. We now have the twofold purpose of (i) illustrating the nature of the atmospheric channel, and (ii) describing and discussing some of the ways in which the channel can be probed.

The optical path employed for most of this study was between The Museum of Science, in Boston, and the Harvard College Observatory, in Cambridge. The map in Fig. 24 shows the locations of these sites which are separated approximately 4.5 km. The light source was a Helium-Neon laser housed in a weathertight box located on the tower balcony of the museum as shown in Fig. 25. The transmitted light was collimated into a beam, 2 inches in diameter, having uniform phase and approximately Gaussian intensity profile. A small spotting telescope mounted at the rear of the laser was used in the initial alignment of the beam with the receiver. Precise pointing of the beam required persons at each end of the link equipped with radio telephones for communication.

Fastened to the top of the box there is a smaller case containing a mercury arc lamp of the kind used in street lighting. By placing various gratings in front of the lamp some of the qualitative effects of the turbulence upon image degradation were studied visually.

The roof of the Harvard College Observatory was the terminal point of our link. We were privileged to be able to make many of the visual and photographic observations with the famous 15-inch refracting telescope shown in Fig. 26. Although it is more than 100 years old, this telescope is still in excellent condition, and it is only the growth of the metropolitan area with subsequent deterioration of observing conditions which has reduced its usefulness for astronomical observing. This telescope is ideal for our purposes, as it has a large unobstructed aperture and long focal length. The advantage of long focal length is high magnification in the primary focal plane.

Because some of our experimental electronic measuring equipment was too bulky and awkward to use with the 15-inch telescope, an 8-inch reflector was mounted on a bench in an adjacent penthouse.

4.1 QUALITATIVE CHANNEL DESCRIPTION

4.1.1 Aperture Intensity Profile

The property of the disturbance that is most easily measured is the random intensity profile of the incident wave. In a plane that is a few centimeters ahead of the focal plane of the telescope, the field, although spherically converging, still retains the same

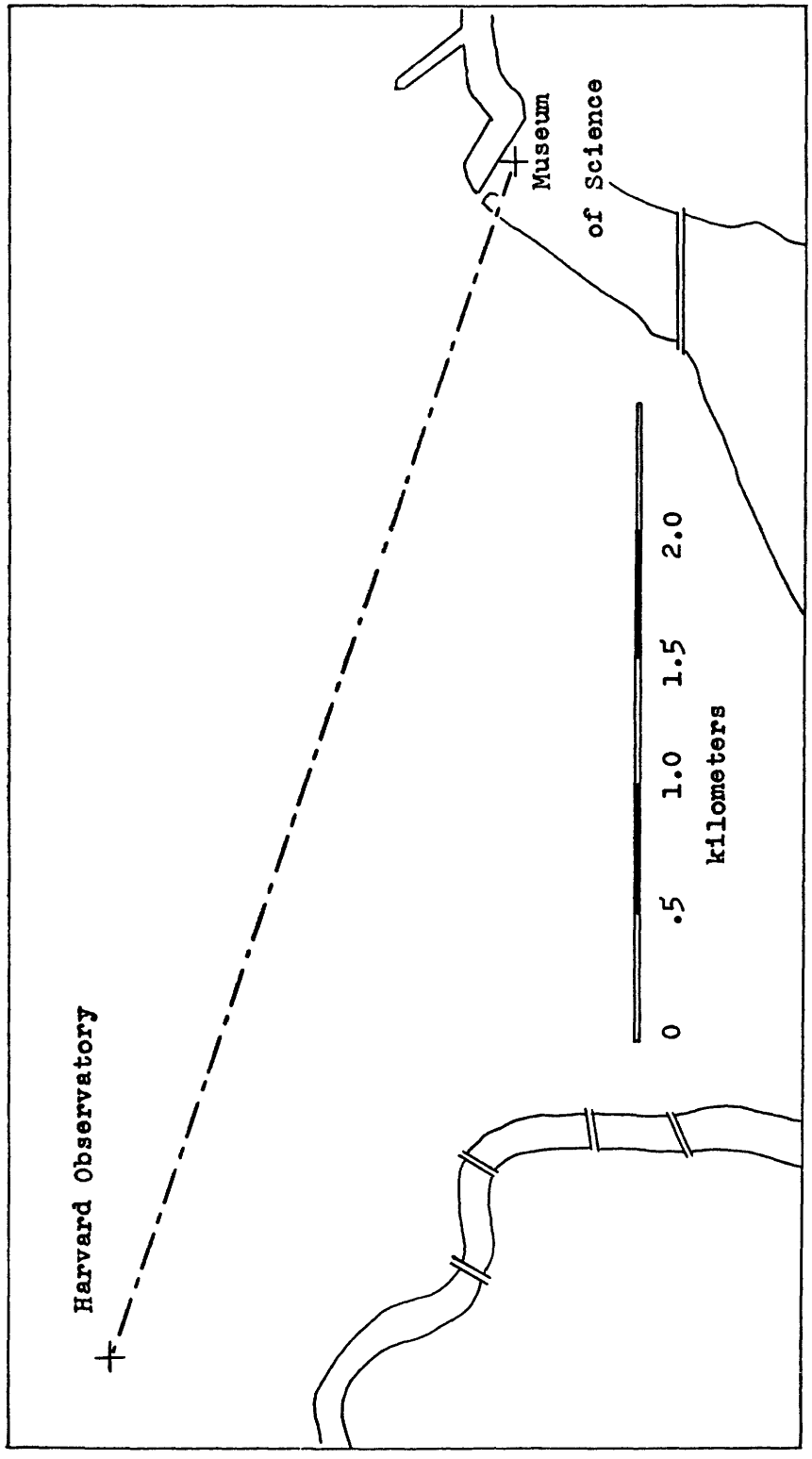

Fig. 24. Optical path.

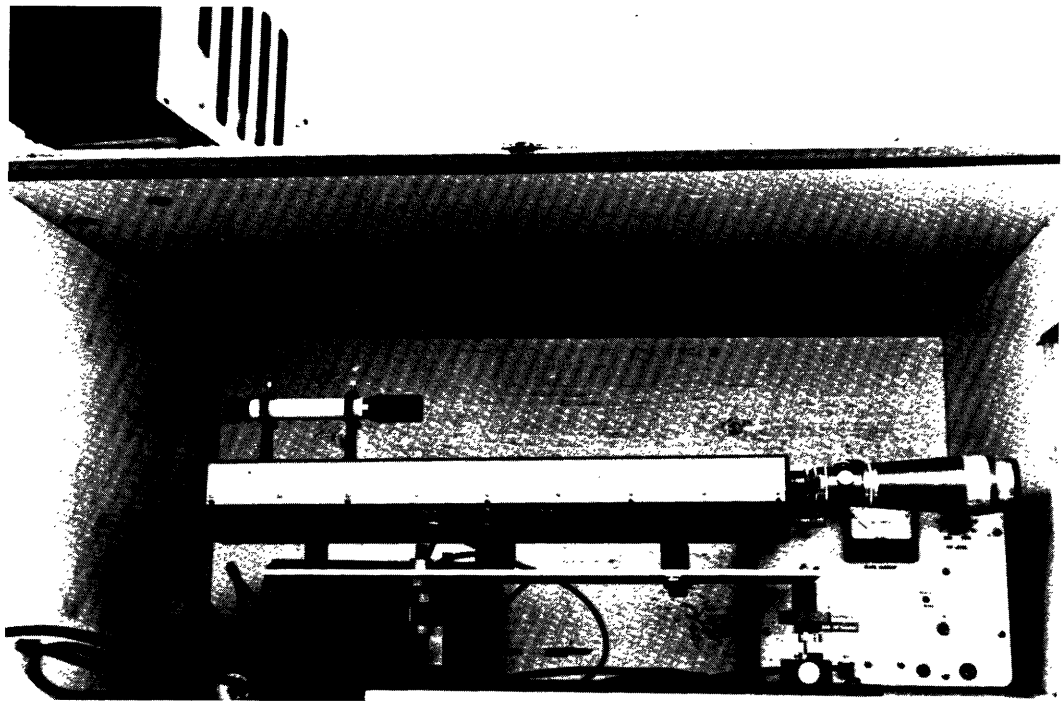

Fig. 25. Laser (0.6328 μ) atop The Museum of Science, Boston, Massachusetts.

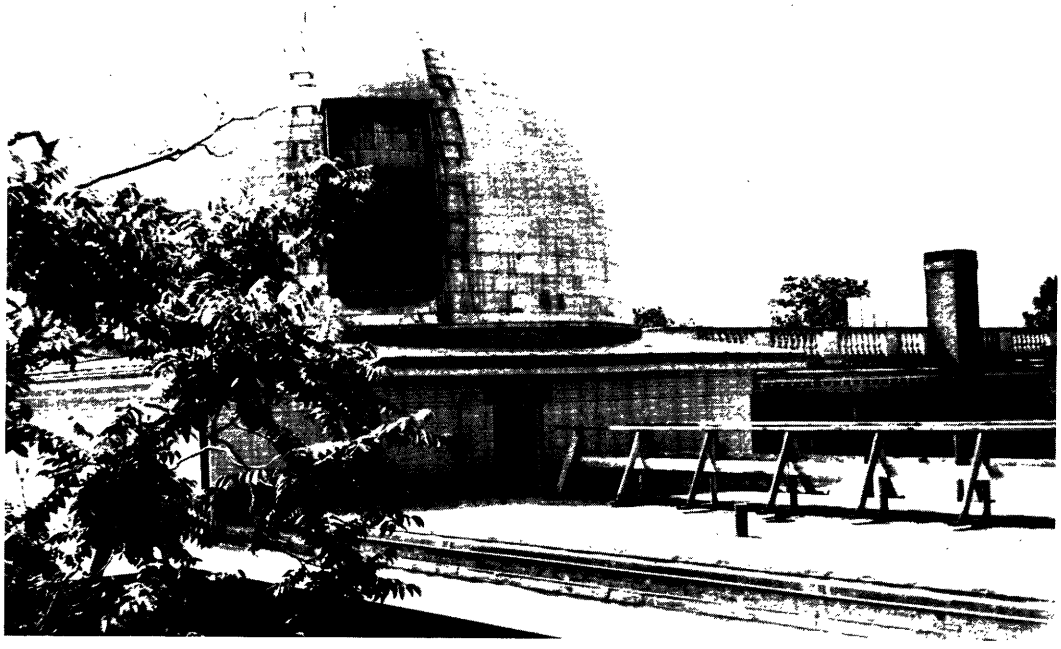

Fig. 26. 15-inch refractor at Harvard College Observatory, Cambridge, Massachusetts.

intensity profile that is incident on the objective. The linear scale is conveniently reduced, however. Either by placing the photographic film in this plane or using an additional lens to project this plane on the film, the spatial variations in the incident intensity are recorded. Figure 27 shows 8 successive frames taken in this manner with a 16-mm motion picture camera coupled to the 15-inch refractor. The aperture correlation region for the amplitude disturbance can be roughly estimated. In the example

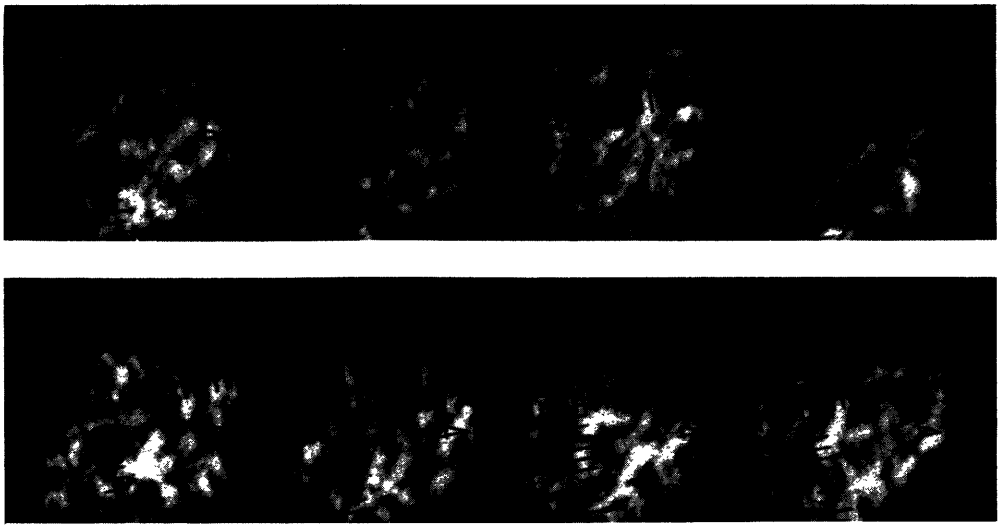

Fig. 27. Intensity profile across the 15-inch objective.

shown here it appears that intensity correlation is lost beyond approximately 1 inch. Some of the time behavior can also be studied with this motion-picture technique. When the film is run on a motion projector, the effect of the wind blowing the disturbances across the aperture is very marked. The hypothesis that the disturbances are "frozen" into the atmosphere does not hold indefinitely, and from the film it appeared that after 3 inches or so of movement across the aperture the structure had greatly decayed. Such joint time and space correlations of the wavefront intensity have been studied by J. E. Ehrenberg and the results have been published in his Master's thesis.[18]

4.1.2 Focal-Plane Patterns for Small Apertures

The patterns of Fig. 27 describe only the intensity variations of the field. For both digital communication and image-estimation systems, however, the phase of the process is usually of greater interest. Some of this phase information was deduced simply by varying the aperture size and observing the behavior of the focal-plane image. When we employ a circular aperture that is smaller than both the phase and amplitude correlation scales, the image in the focal plane is an almost perfect Airy pattern. That is, it is the true diffraction pattern from a circular aperture, showing a central disk with

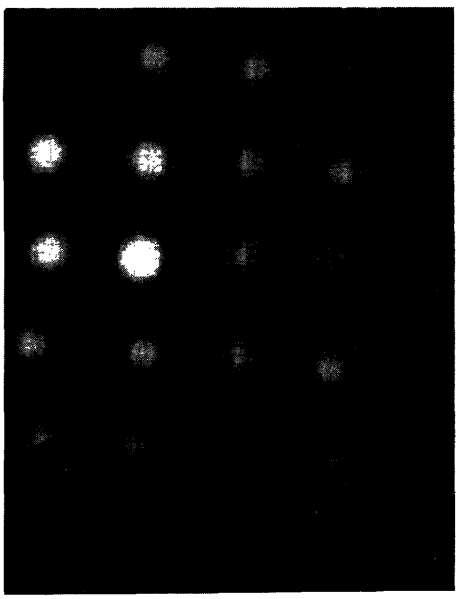

Fig. 28.

Focussed images, 0.5-inch diameter pupils.

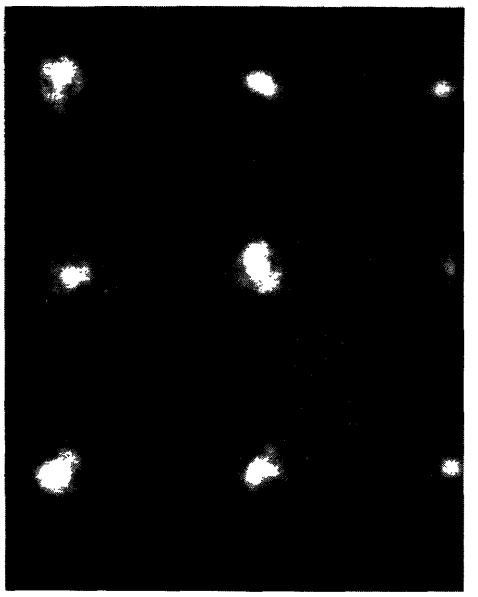

Fig. 29.

Focussed images, 1-inch diameter pupils.

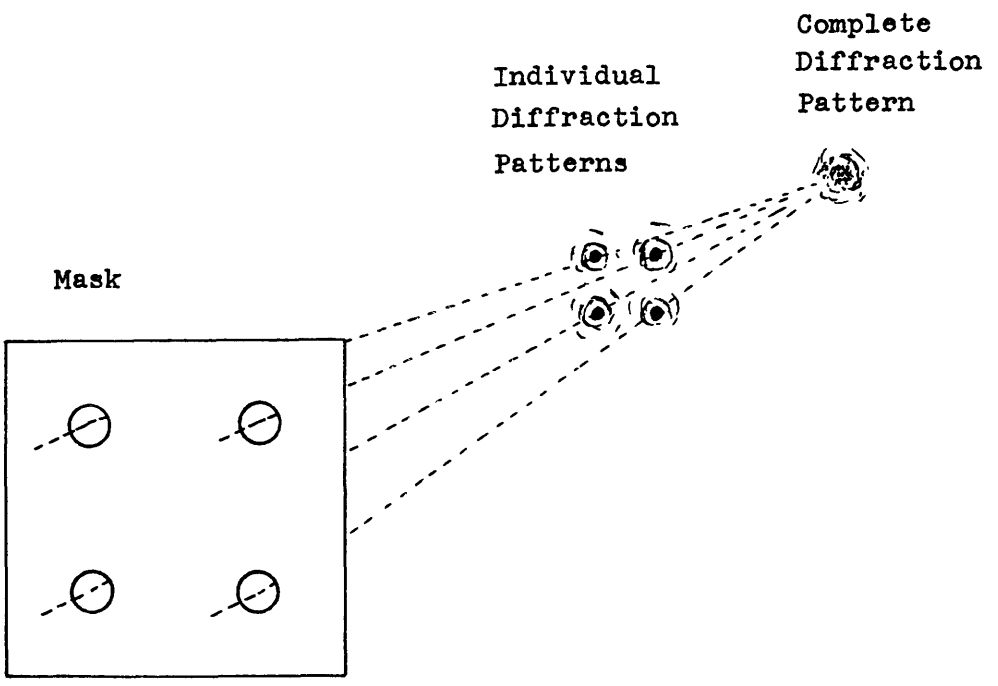

Fig. 30. Aperture sampling of the image.

a series of increasingly fainter concentric rings. The only effect of the turbulence is then a time-variant fluctuation in the over-all intensity of the pattern. Variations in the absolute phase of the wave are undetectable in such a recording, but are of no interest in the imaging problem. As the diameter of the aperture is slowly increased, the shape of the pattern remains, but the dimensions shrink because of the increased aperture size. The first noticeable effect as the correlation diameter is exceeded is a random motion of the Airy disk. This random motion can be related to the first-order or linear term in a Taylor's series expansion for the phase disturbance, and provides an almost complete description of the process when the aperture is small. Finally, when the aperture is made much larger than the correlation scale, the simple structure of the disturbance is lost, and a highly distorted image is formed.

Some of these effects can be seen in Figs. 28 and 29. These pictures were recorded on the same evening as the previous intensity measurements and were obtained in the following manner. A mask consisting of an array of small holes was placed over the objective. The focal-plane pattern, which comprises the diffraction pattern of this entire array, is not too informative. By observing the pattern just a bit forward of the true focal plane, however, we can resolve the focussed image of each aperture hole separately, as illustrated in Fig. 30.

Two sequences of motion-picture film were shot in this manner: First with 0.5-inch diameter holes on a 2 × 2 inch grid, and then with 1-inch diameter holes on a 4 × 4 inch grid. The first example (0.5-inch diameter holes) gave Airy disk patterns showing almost no discernible motion when the film strip was viewed with a projector. It would appear that over the area of these 0.5-inch diameter holes, the field remained quite coherent in both phase and amplitude. The second set of pictures, made with 1-inch diameter holes, showed appreciable motion, perhaps half the disk width which corresponds to a wavefront tilting of 15-20 μrad. These two sets of data illustrate the point brought out by Fried,[19] that random tilt is a very significant characteristic of the phase disturbance over a small aperture and that if this tilting or image motion can be tracked, the useful aperture can perhaps be increased approximately three times before the higher order disturbances significantly distort the image.

It is obvious, however, that even in the 1-inch diameter case, the tilting does not completely characterize the disturbance. Already there is some loss in the symmetry of the pattern, caused by either spatial variation in the intensity or the higher order phase disturbances. J. H. Shapiro has carried out an investigation of this problem, seeking simple models to characterize the disturbances over small apertures. His results are published in his Master's thesis.[20]

4.1.3 Focal-Plane Patterns for Large Apertures

When the full aperture of the telescope is employed, the focal-plane pattern no longer has a simple structure. Figure 31 is an example of the pattern resulting when the full aperture of the 8-inch reflector was used, and about all that can be said is that the

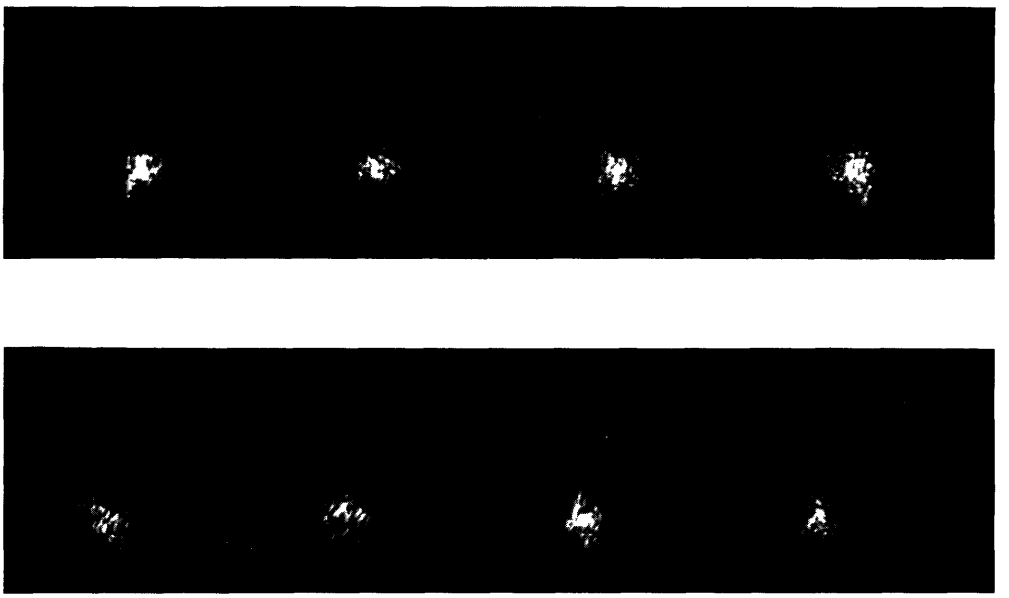

Fig. 31. Focussed image for full 8-inch objective.

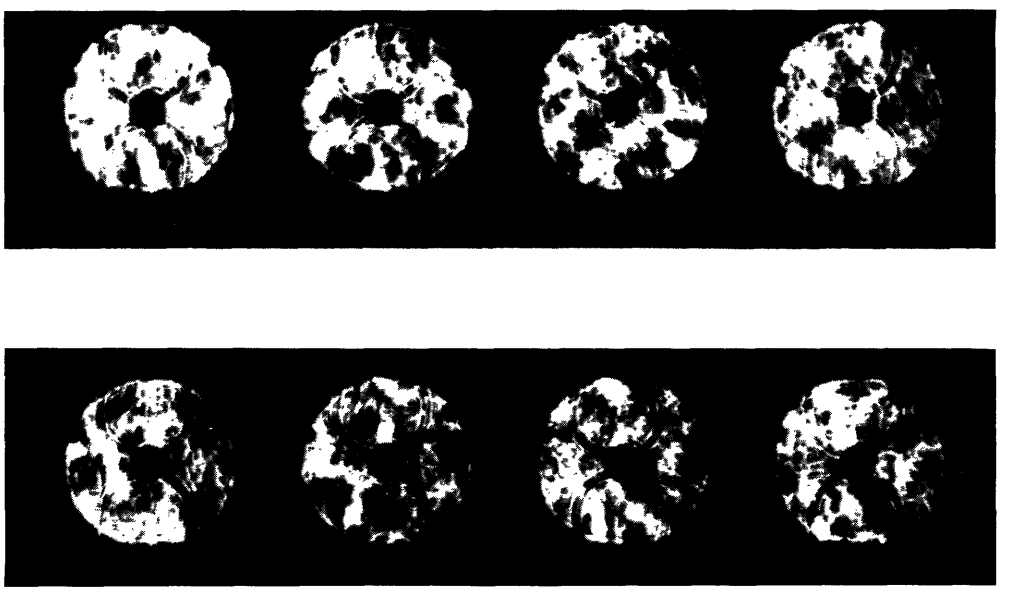

Fig. 32. Profile of intensity across 8-inch objective.

energy in the image is randomly distributed over approximately 40 μrad field of view.

The incident intensity profile over the aperture was also measured a few moments before, and a sequence of frames is shown in Fig. 32. The similarity of this intensity pattern with that of Fig. 27 suggests that conditions were somewhat the same on the two different nights. The dark disk in the center of each pattern and the rings on each side are simply the shadows of the secondary mirror and supporting structure.

4.1.4 Fresnel Biprism Measurements of Field Coherence

More information concerning the phase process can be obtained by using the Fresnel biprism form of interferometer described in Section II. This was set up with a motion picture camera as shown in Fig. 33.

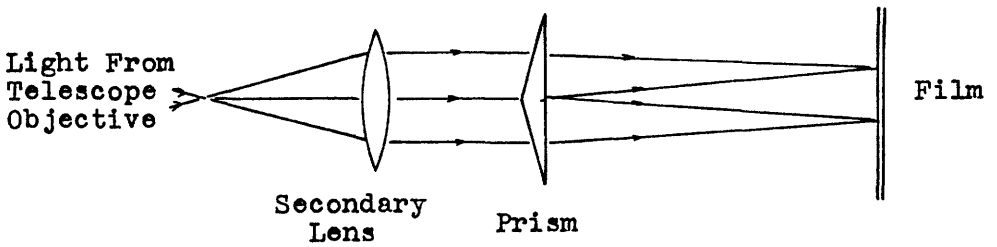

Fig. 33. Fresnel biprism arrangement.

Fringes are formed in the region where the two displaced halves of the aperture overlap. Recall that the spatial phase and intensity of these fringes is directly related to the phase and magnitude of the incident mutual coherence function. The distance between the prism and film determines the amount of overlap of the aperture sections, and hence the displacement variable of the coherence measurement. Examples of this technique are shown in Figs. 34 and 35, in which two different displacements of 2 inches and 4 inches were used. The fringes of interest run horizontally, and are the most closely spaced ones that are visible. The other coarser fringes result from diffraction from the boundaries of the aperture and the discontinuity in the prism.

If a uniform plane wave had been incident, the interference lines would have been absolutely straight. The presence of corrugations in the incident wavefront causes the fringes to wiggle, and a particular fringe line follows the locus of constant phase difference between points of given displacement.

Various forms of distortion can be deduced by the character of the fringe pattern. Uniform tilting of the wavefront across the entire aperture is undetectable, but can be discerned with other methods (see section 4.1.2). A differing tilt on the two areas that are interfered is observed as a local twisting, bunching or stretching of the fringes. One can obtain a spatially continuous measurement of the distortion by following along the fringes, whereas in the Airy disk method the disturbance is only coarsely sampled.

Admittedly, the distortion in the fringes is hard to see in these small prints. When the film is projected with high magnification onto a screen, however, twisting of the fringes is quite noticeable in both examples. When we compare these patterns with the interferogram for an undistorted incident wave, we find that the two sets of lines are

Fig. 34. Fresnel biprism pattern – 2-inch overlap.

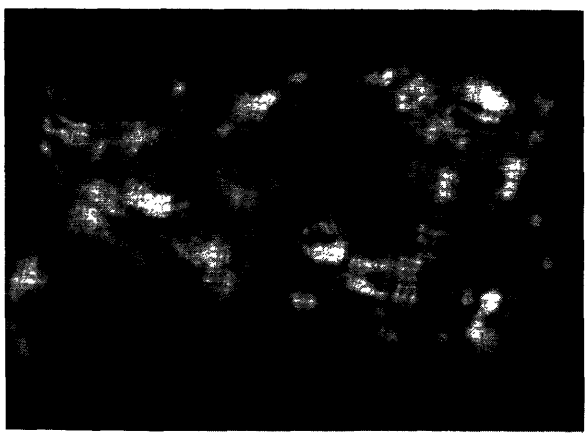

Fig. 35. Fresnel biprism pattern – 4-inch overlap.

correlated over distances of only 1 inch or so. The significance of this to image estimation is that there are areas whose fringes differ in phase by approximately π radians. These will tend to give a cancellation effect if the mutual-coherence function is integrated over an area larger than the correlation region. The average signal-to-shot-noise level will not improve if the integration area is increased beyond this value, but we lose some of the channel diversity that could be exploited if proper spatial sampling and one of the post processing schemes discussed in Section III were used.

The effect of the atmospheric fading on the mutual coherence is also brought out in these two pictures. We recall that if the amplitude on either of the points being interfered should fade, then the coherence function would fade, since it is the product of the fields. Thus the strongly fringed regions appear as clumps in the interferograms.

4.1.5 Full-Aperture Phase Mapping – Spatial Heterodyning

This Fresnel biprism technique yields relative measurements of the phase disturbance between points. Often it is desirable to have a full map of the absolute phase process. Probably the nicest picture that can be made of the phase across the aperture is obtained by beating the incident wave against a tilted, but otherwise uniform, plane wave of the same frequency. At optical wavelengths this reference wave must usually be

Fig. 36. Spatial heterodyne pattern.

obtained from the same source as the incident wave in order to retain temporal coherence. M. Tamny[21] has studied such a measurement technique, using a two-way path, reflecting the wave from a downrange mirror. Figure 36 is one of the pictures described in his Master's thesis, and shows the type of pattern to be expected. This was obtained over a relatively short path of a few hundred feet for which the amplitude disturbances are minimal. The phase disturbance across the aperture shows up in the twisting of the fringes.

4.2 QUANTITATIVE MEASUREMENTS OF PHASE AND AMPLITUDE – TWO-POINT COHERENCE MEASUREMENTS

This, then, is the extent of the photographic measurement techniques that were studied. They yield reasonably qualitative pictures of the turbulence-induced disturbances. The most important property of these disturbances with respect to image estimation is often the temporal variations in the field coherence between two points.

4.2.1 Description of Equipment

In order to obtain a more quantitative understanding of these properties, the equipment pictured in Fig. 37 was employed. Here we used the telescope as an interferometer, as described in Section II. The aperture was completely masked, except for two holes at the points where we wanted to measure the field coherence. The reach of the interferometer was extended by means of the mirrors (M) in Fig. 38. The diffraction pattern for this aperture mask is an Airy disk crossed by straight fringes, whose

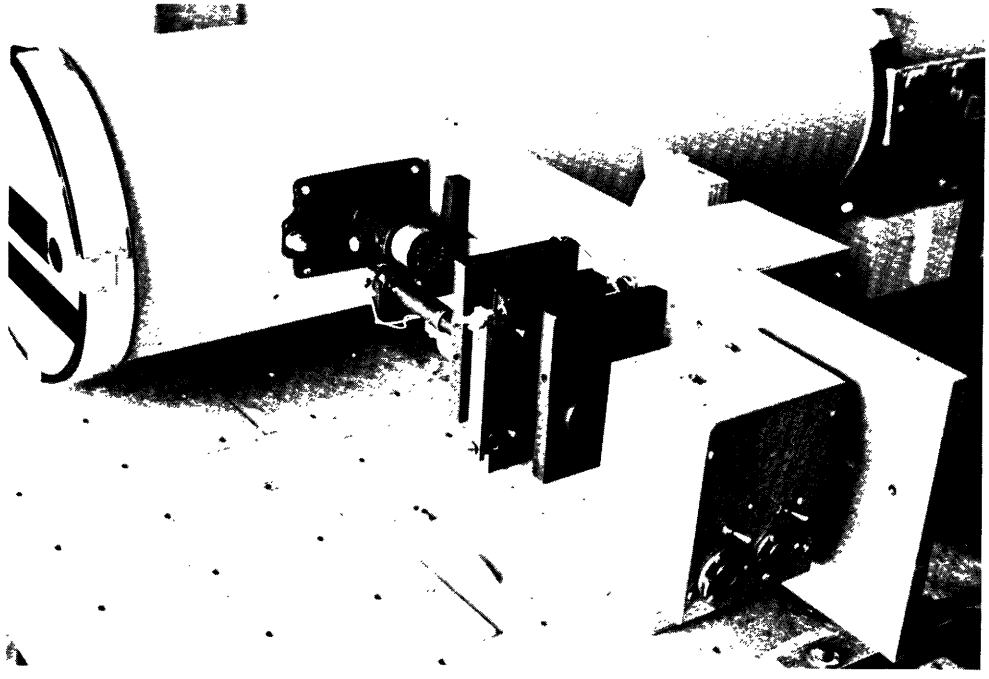

Fig. 37. 8-inch reflector with aperture mask and fringe scanner.

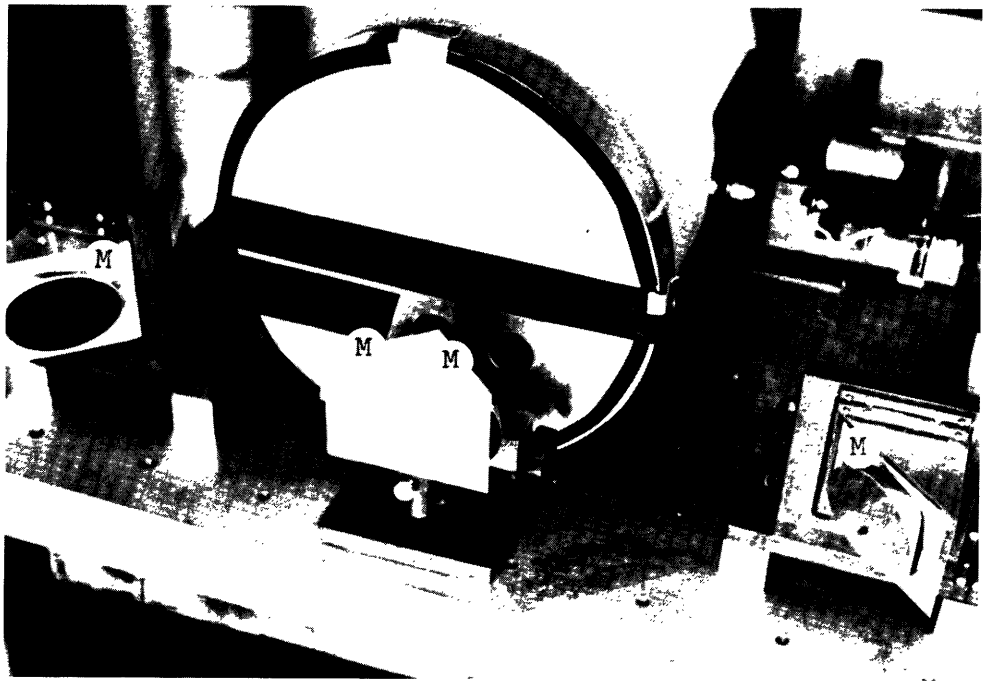

Fig. 38. Extension using mirrors.

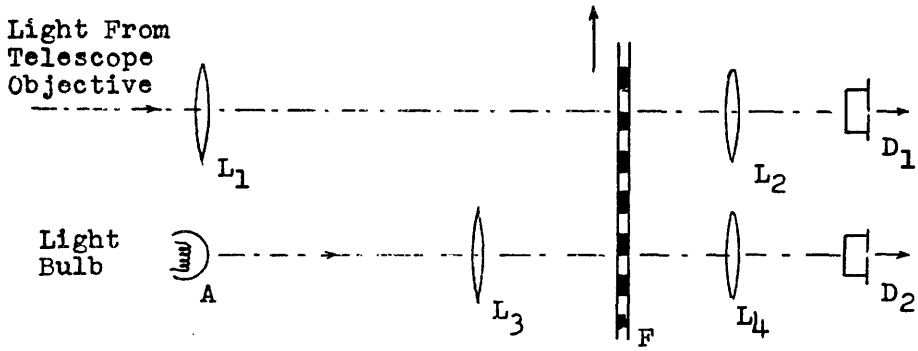

(a)

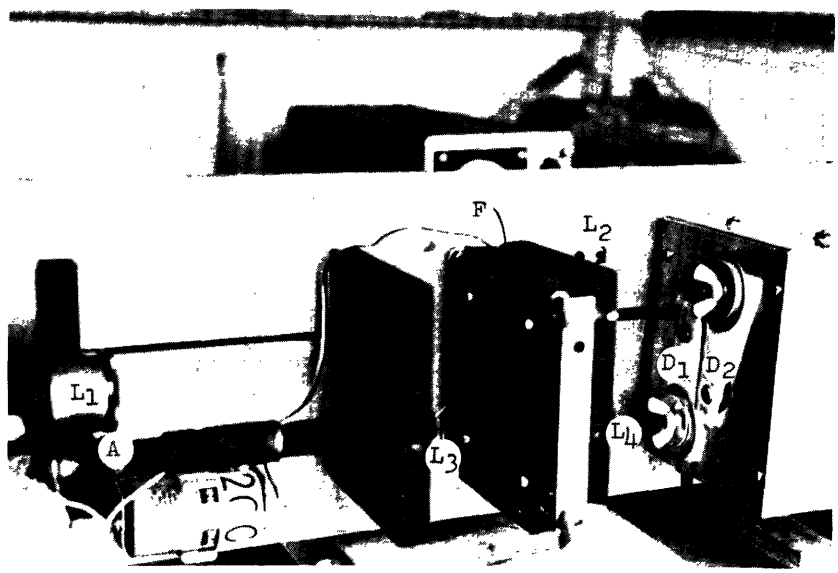

(b)

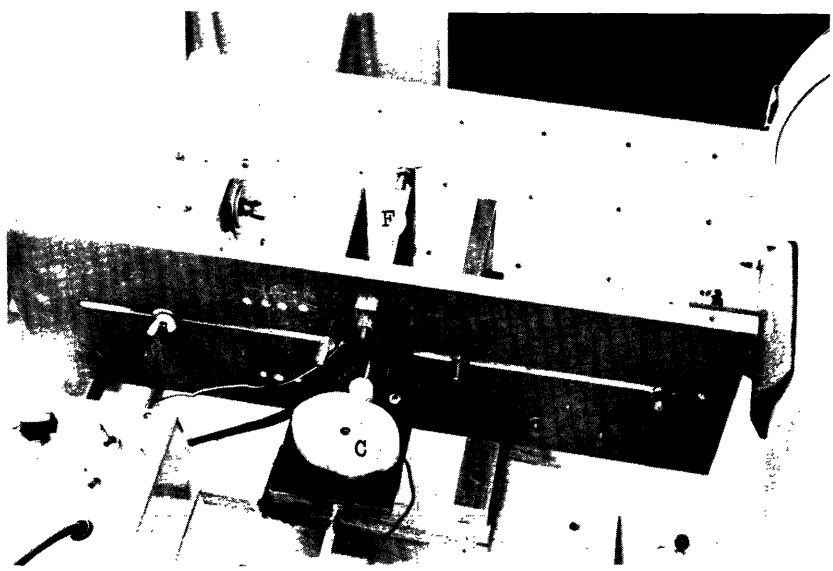

(c)

Fig. 39. (a) Fringe scanner diagram. (b) Fringe scanner – front view. (c) Fringe scanner – rear view.

spatial phase and amplitude correspond to the phase and magnitude of the field coherence function.

a. Fringe Scanner

These fringes were scanned with the device illustrated schematically in Fig. 39a and pictured in Fig. 39b and 39c.

The focal plane-field pattern was projected by lens L_1 onto the Ronchi ruling held by the sliding block F. This block was pushed back and forth by means of the motor, cam assembly C, and a return spring. As the Ronchi ruling moved back and forth the fringes were scanned by the lines in the ruling, and the transmitted light energy was focussed by lens L_2 onto the photodiode detector D_1. The signal from this detector consisted of: (i) a pair of low-frequency terms corresponding to the fluctuations in the total incident energy through each hole, and (ii) a periodic signal with phase and amplitude related to the phase and amplitude of the fringes. With the particular cam shown in the picture, the Ronchi ruling moved back and forth twice each second, a total travel of 2 inches per second. Since the Ronchi ruling contained 300 pairs of alternate opaque and transparent lines per inch, the mean frequency of the periodic output signal was 600 Hz.

Another cam, which moved the ruling at only half this speed, was made, and it reduced the carrier frequency to 300 Hz. It is always necessary, however, to use a carrier of high enough frequency to avoid aliasing the interference signal with high-frequency components in the baseband intensity fading signals. On the other hand, the higher frequency cams have the disadvantage that there is a shorter period between turn around moments for the ruling. When the ruling stops and starts to go in the other direction, it is usually impossible to retain the phase of the signal; thus, the useful observation interval is limited.

The actual phase of the fringes in the diffraction pattern was obtained by comparing the phase of the signal from D_1 with that of a reference signal generated by a small lamp A, lenses L_3 and L_4, and detector D_2. The lamp contained a small helically wound filament that was focussed onto another section of the Ronchi ruling, with the spacings on the helix matched to the lines on the ruling.

When the phases of these two signals were compared, the effect of variations in the velocity of the ruling cancelled out, and we obtained the phase disturbances that were due only to the atmosphere.

The block diagrams of the recording and processing instrumentation are shown in Fig. 40. Both of the signals were filtered to remove low-frequency components, and then recorded on a dual-track magnetic tape recroder. Comparison of the two signals was made later in the laboratory, by using a pair of demodulators to obtain the in-phase and quadrature components of the wave coherence function. These two voltages, together with the signal envelope, were then sampled, converted to digital form, and re-recorded for playback later into the TX-0 digital computer. With the computer we then calculated

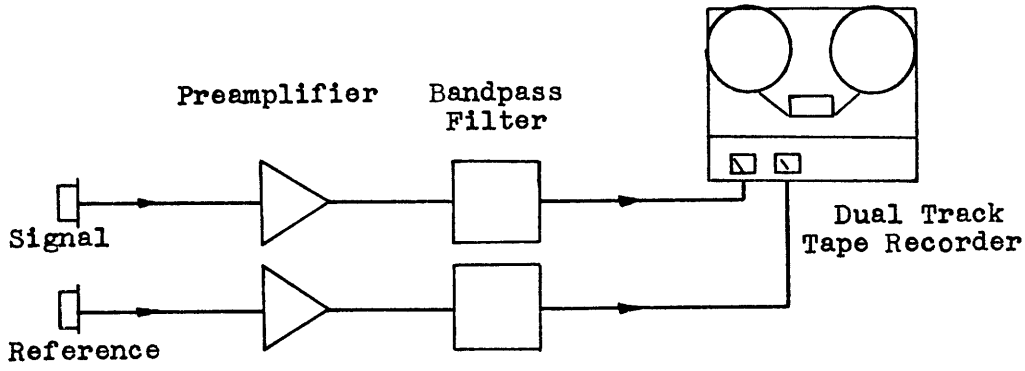

Data Recording

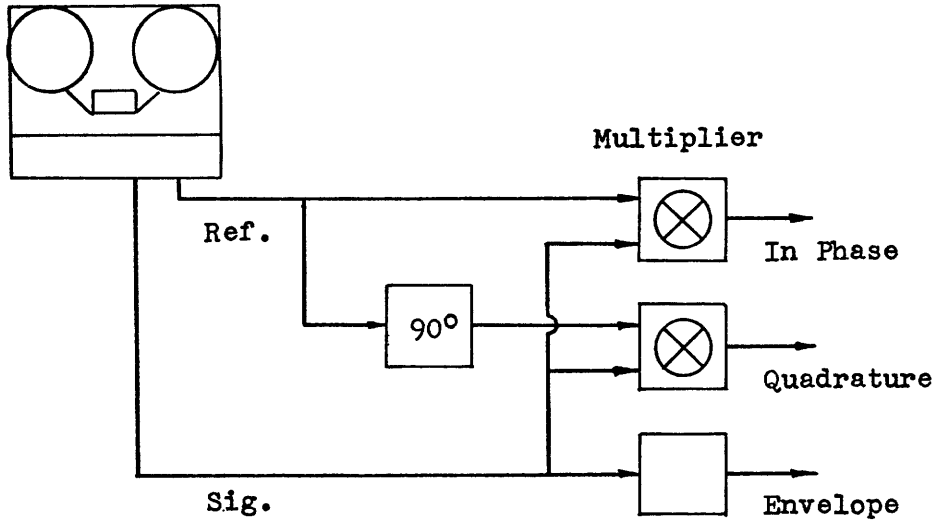

Phase Comparison

Fig. 40. Processing system.

the phase angle of the coherence process, and derived various statistical properties of the phase and amplitude disturbances in the wave coherence function.

b. Alignment

The procedure for adjustment of the scanning device was the following. The required projection distance between the lens L_1 and the Ronchi ruling was calculated, and final focussing adjustments were made by observing the output from D_1 and adjusting to obtain maximum amplitude in the periodic component. The scanning device was then tilted, or the aperture mask rotated, to obtain parallelism between the fringes and the lines on the ruling, again adjusting for a maximum signal amplitude. The photodetectors D_1 and D_2 were mounted on plates that could be moved about, so that the light beams that exit from L_2 and L_4 were centered on the small detecting surface of each diode.

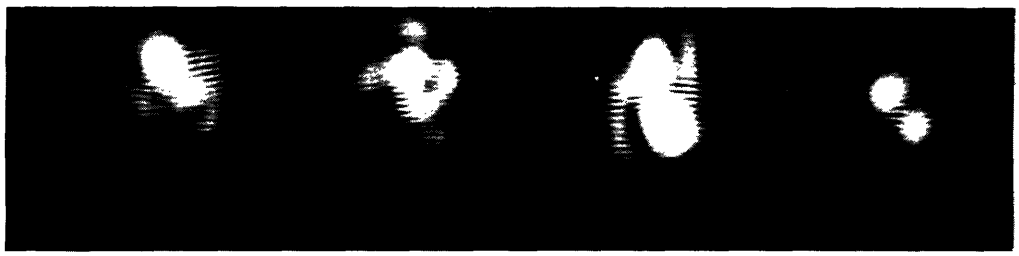

Fig. 41. Fringe pattern.

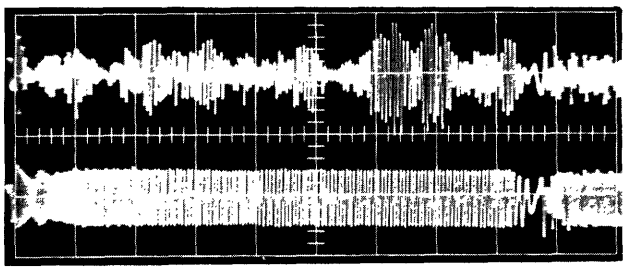

Fig. 42. Signal waveform (25 msec/cm).

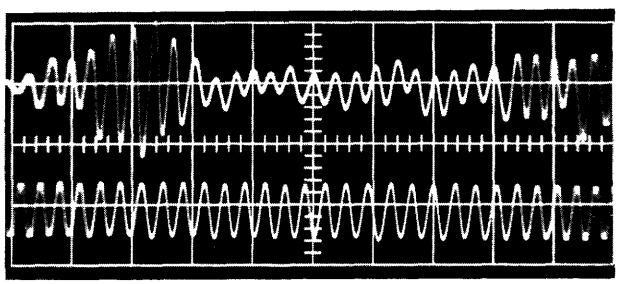

Fig. 43. Signal waveform (5 msec/cm).

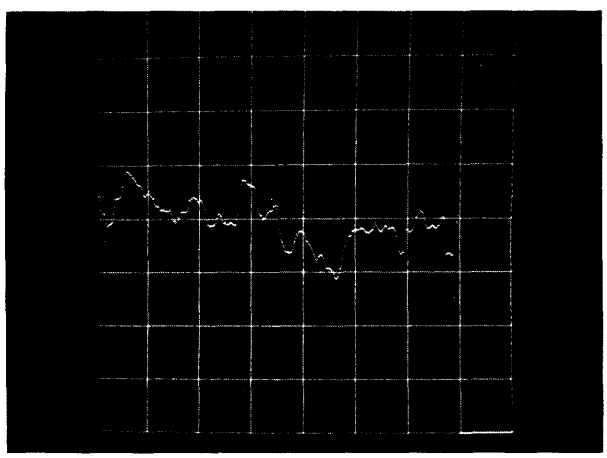

Fig. 44. Phase on TX-0 display.

Use of mirrors to extend the reach of the interferometer brings up further alignment problems. The telescope tube was first rotated so that one could look into the eyepiece (lens L_1). Without the center mirror in place, this eyepiece focussed to give a proper image of the source to the eye (virtual images at infinity with the two Airy disks appearing to completely overlap). With the center mirror installed and the mirror supports adjusted, the two Airy disks again overlapped in the same place. This established a proper relationship between the optical axis of each pair of mirrors and the telescope. The procedure for alignment of the scanning device was then as before.

c. Typical Output Signals

An example of the fringe pattern that was produced in the focal plane is shown in Fig. 41. The hole diameter should be so chosen that the field remains coherent across the area of the hole. That is, so that there is little noticeable movement of the Airy disk. In the example shown, we have intentionally made the hole diameter a bit larger than is advisable, in order to illustrate an important point. The Airy disks tend to separate if the holes are too large, because of differences in the local tilt or angle of arrival. The common area in which the fringes are generated will then vary randomly. In such case, fading in the mutual-coherence process results not only from the amplitude fading of the waves but also from the phase incoherence.

Figures 42 and 43 are typical of the waveforms recorded from the signal and reference detectors. Figure 42 has the longer horizontal sweep scale, and shows the interruptions in the reference signal occurring at the instants when the direction of the Ronchi ruling is reversed. These interruptions provided a convenient signal for triggering synchronization circuits in the processing equipment. Figure 43 shows a portion of the same record on an expanded scale. The fading that often occurs in the interference signal is well illustrated.

A typical plot of the phase of the process as calculated by the TX-0 computer is shown in Fig. 44.

4.2.2 Springtime Results – 4.5-km Path

The first results that we present were obtained on the Museum of Science-Harvard path, late in April 1968. Experiments were conducted on several evenings and the particular results presented here were representative of this set of experiments.

These particular recordings were taken on April 28th, 1968 between 1 a.m. and 3 a.m. under the weather conditions tabulated below.

air pressure	1017.0 mbar
temperature	48°F
dew point	38°F
wind bearing	330°
wind velocity	12 knots
velocity perpendicular to path	4 m/sec

Hole diameters of 0.5 inch were necessary in order to get within the correlation scale of the disturbances.

Recordings of the time-variant mutual-coherence process were made for a range of displacements, and the resultant data were processed for (i) the probability distribution function of the amplitude of the mutual-coherence process, and (ii) the probability density function and temporal and spatial structure functions of the phase of the mutual-coherence process.

a. Amplitude Statistics

The distribution function of the amplitude process is shown in Fig. 45 for displacements of 2, 4, and 6 inches. The results are plotted with log-normal probability coordinates. A log-normal distribution function then appears as a straight line on such a scale system. The three curves have been arbitrarily scaled in amplitude to separate them on the graph.

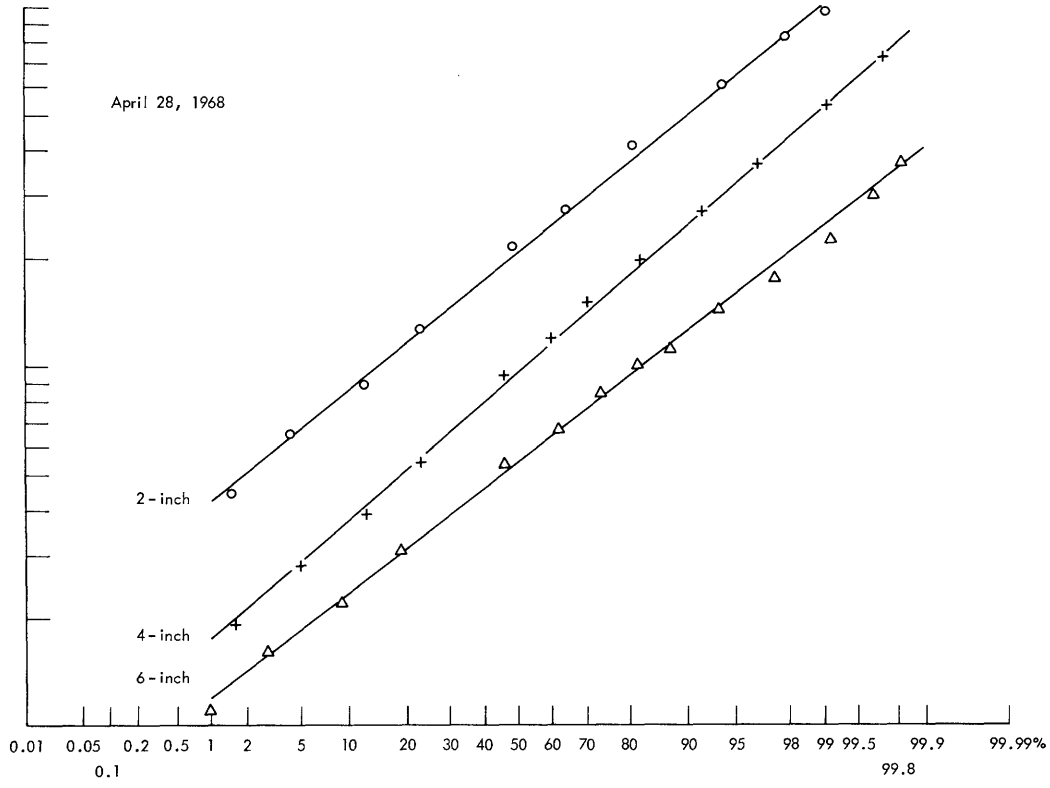

Fig. 45. Probability amplitude distribution function.

The first point to note is the fit of the data to straight lines which substantiates the hypothesis that the mutual-coherence process suffers log-normal fading in propagating through the atmosphere.

The severity of log-normal fading is described by the variance of the log amplitude.

This is the slope of the distribution function when plotted with the special coordinates. The standard deviation, σ, of the natural (rather than base 10) log amplitude of the coherence process is tabulated below.

Displacement	Standard Deviation
2 inches	$\sigma = 0.67$
4 inches	$\sigma = 0.71$
6 inches	$\sigma = 0.64$

b. Phase Statistics

Measurements of the phase process were conducted in the following manner. Each half-cycle of the Ronchi ruling was taken to constitute one record of the phase process. Depending upon which cam was used (300 Hz or 600 Hz) this record had a useful length of 500 or 250 msec. At the end of the record, the Ronchi ruling stops and reverses its motion, which makes it rather difficult to retain the continuous value of the phase across this interruption. Indeed, the change in direction of the ruling reverses the sign of the phase between the fringe and reference signals.

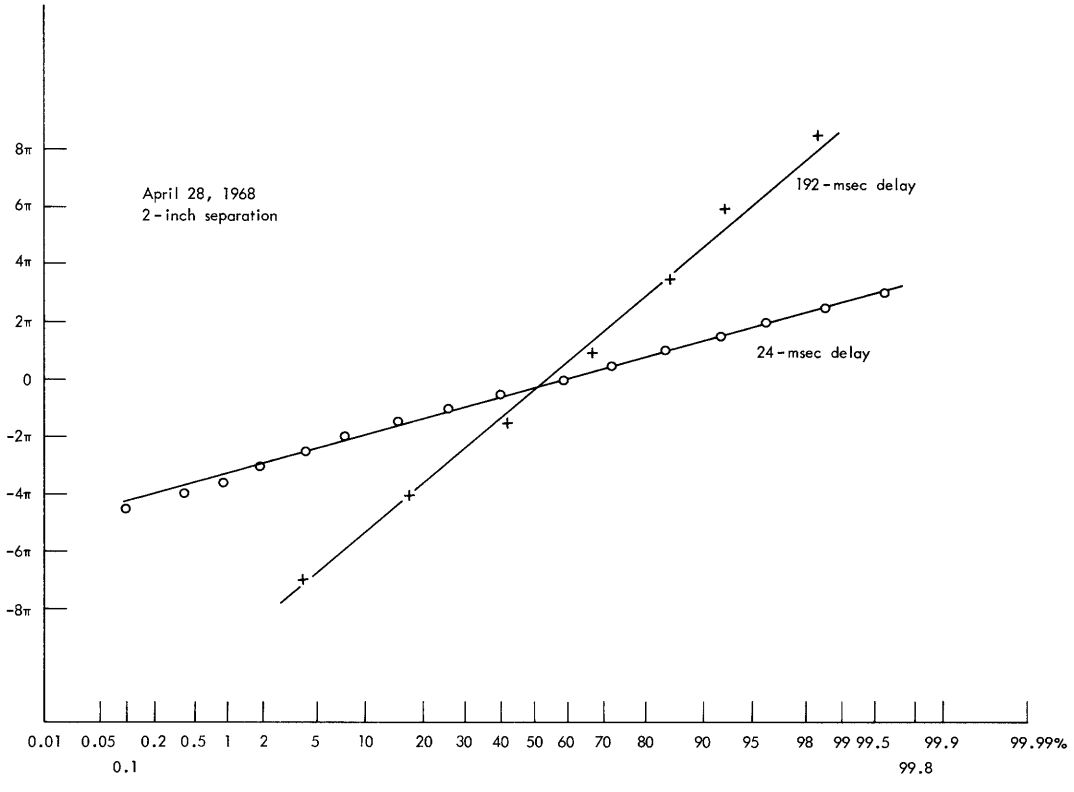

Fig. 46. Probability phase distribution function.

In processing each record, the computer arbitrarily set the phase of the first sample to a zero 2π modularity. From then until the end of the record the full (rather than 2π modulo) value of the phase was retained. The computer next calculated a set of phase differences between the initial sample and samples of increasing delay in the record. From a large number of records, the probability amplitude distribution function was then determined. A typical set of such data is plotted in Fig. 46. The scales were selected to yield a straight line for a Gaussian distribution function, and again the Gaussian hypothesis appears reasonable.

From the slopes of these curves we obtain the variance of the phase difference, and hence the temporal structure function of the phase of the mutual-coherence process. These functions appear in Fig. 47. We note that even with 4-msec delay the standard deviation in the phase difference is approximately 1 radian. By the end of the record, the variance of the phase difference appears to be saturating at approximately 12 radians. Assuming that when the structure function saturates the local variations in the phase

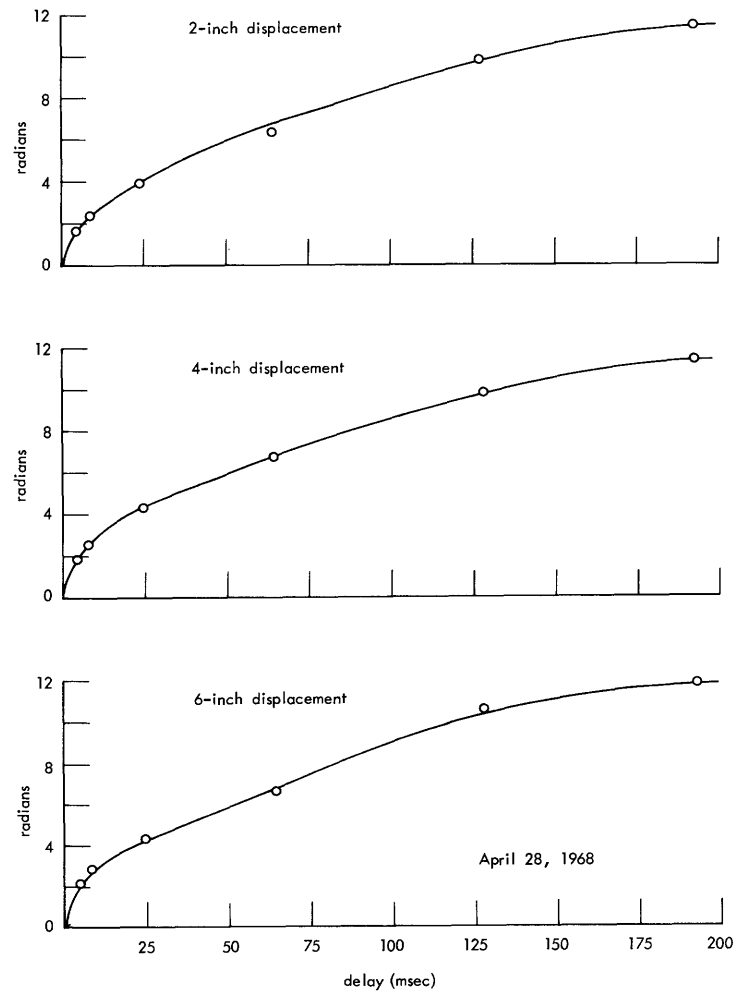

Fig. 47. Temporal phase-structure function.

process are uncorrelated, we can obtain the variance of the difference in phase between the two aperture points simply by dividing the saturated value by two. This method of estimating the phase variance has the advantage that the mean value of the phase, which is a function of the relative positions of the lamp filament and diffractions images, need not be considered. All three curves appear to saturate at about this same value of 12 rad, which implies that the standard deviation of the phase disturbance in the mutual-coherence process is $12/\sqrt{2} = 8.5$ rad for all three displacements.

It is interesting to note, in both the amplitude and phase measurements, an almost complete lack of dependence upon the displacement variable. Additional measurements that were made out to 18-inch displacements also showed this effect. This suggests that the spatial structure function of the amplitude and phase processes has saturated at displacements beyond even a very few inches, and hence that there is little correlation in the local wavefront disturbances.

As we have mentioned, the data recorded in this series of late April experiments all showed about the same behavior, as the weather conditions remained quite similar. Attempts to obtain phase measurements earlier in the year were not entirely successful, because of the extremely rapid fading which tended to alias the 600-Hz carrier of the coherence process.

4.2.3 Autumn Results – 4.5-km Path

We do have one other set of measurements that were obtained on this path, and show the channel in a much more temperate mood. These measurements were obtained on the evening of October 25th, 1967 under the following weather conditions.

air pressure	1012.1 mbar
temperature	57°F
dew point	55°F
wind bearing	130°
wind velocity	15 knots
velocity perpendicular to path	2.6 m/sec

The conditions on this evening were such that a 1-inch diameter aperture was within the correlation scale of the turbulence, a good indication that the atmosphere was more stable than in the springtime experiments.

Figure 48 shows the amplitude distribution function from which we find that $\sigma \approx 0.43$, and is a condition of considerably less severe fading than in the former examples.

The temporal phase-structure function is shown in Fig. 49. Here we find that the correlation time of the process is considerably longer than in the other measurements.

Furthermore the saturation value of 5 rad is only half that encountered in springtime.

These autumn measurements were made under conditions of somewhat less

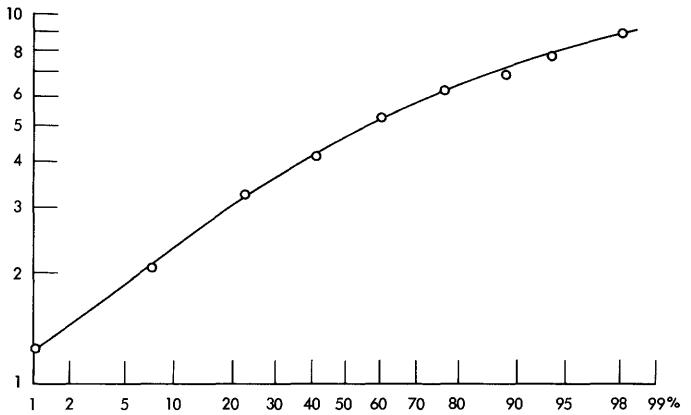

Fig. 48. Probability amplitude distribution function.

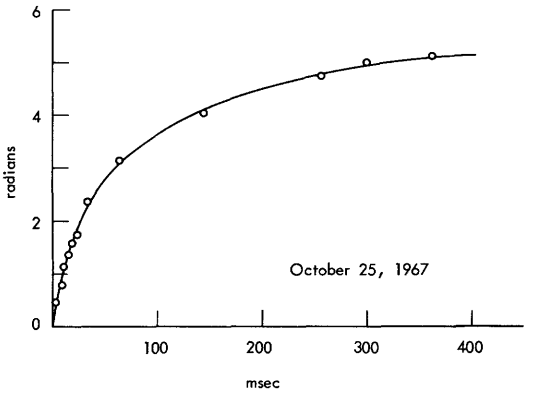

Fig. 49. Temporal phase-structure function.

crosswind and much higher humidity than the spring measurements. Although this may be the reason for some of the difference, the longer term climate difference may have had an influence.

4.2.4 100-m Roof Path

Some phase measurements were also conducted over a much shorter path (100 m) along the roof of M.I.T. Building 20, in order to look at some of the differences in the disturbances between long and short paths. These measurements were made on April 14th, 1968 under the following weather conditions.

air pressure	1018.5 mbar
temperature	45°F
dew point	27°F
wind bearing	070°
wind velocity	10 knots
velocity perpendicular to path	2.2 m/sec

Apertures of 0.5-inch diameter were selected to get within the correlation scale. The amplitude of the coherence signal showed little significant fading, because of the shortness of the path. The temporal phase-structure functions for these measurements are shown in Fig. 50. The notable feature of these measurements is the magnitudes of the

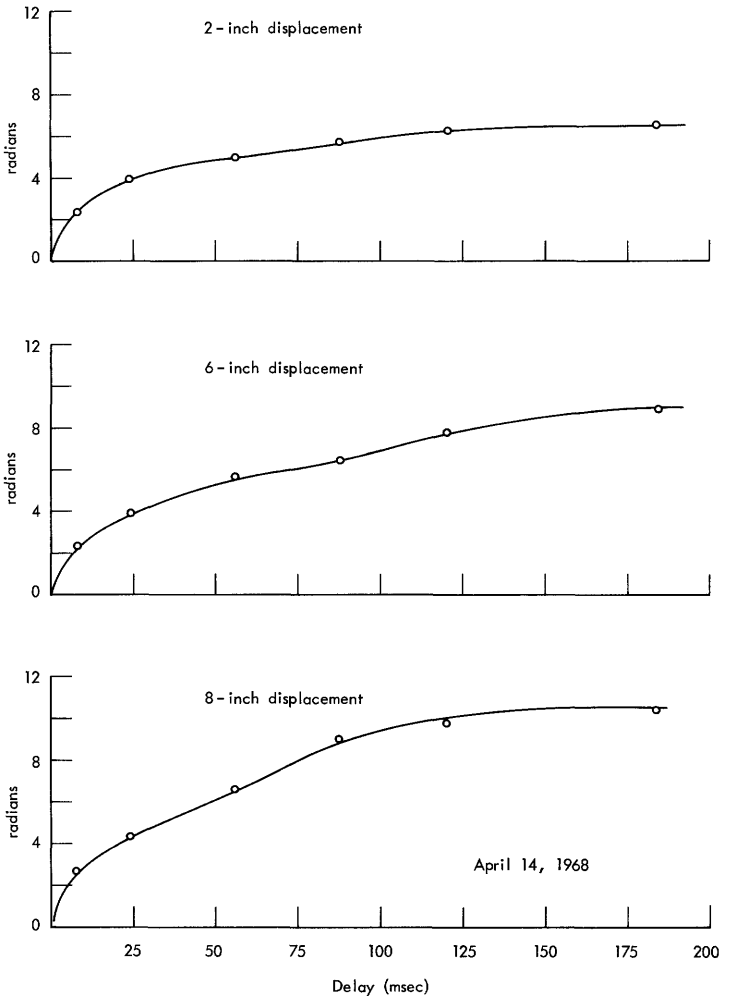

Fig. 50. Temporal phase-structure function.

phase variances which are almost the same as those presented in section 4.2.2, although the path length is much less than that between The Museum of Science and Harvard College Observatory. This seems to support the contention that the phase disturbances are generated by the nearby turbulence, while the amplitude disturbances are a phenomenon of the long atmospheric paths.

4.2.5 Laboratory Simulation

A final set of measurements was conducted in order to evaluate laboratory simulation of a turbulent atmospheric path (Fig. 51). The fringe scanner and a small telescope were mounted on one bench and the laser and collimator on another. In front of the telescope objective we placed a strong source of local heating, an electric hot plate. A fan was located 5 feet away from the hot plate (directed somewhat away from the objective) in order to stir up the air in the room. The actual locations of the hot plate and fan, and the position of the equipment in the room all tended to influence the severity of the turbulence. By adjustment of the various components, the amplitude of the

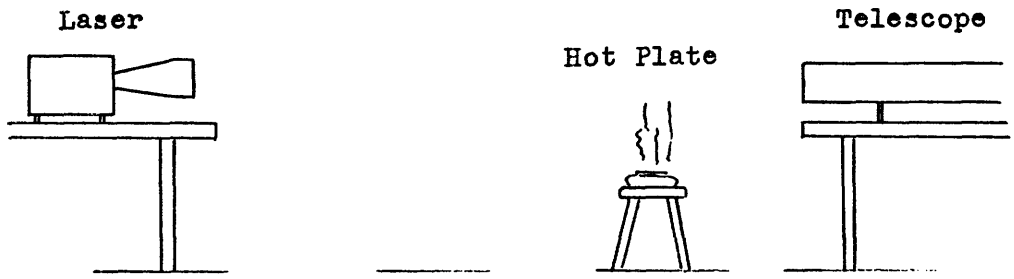

Fig. 51. Simulation of atmospheric turbulence.

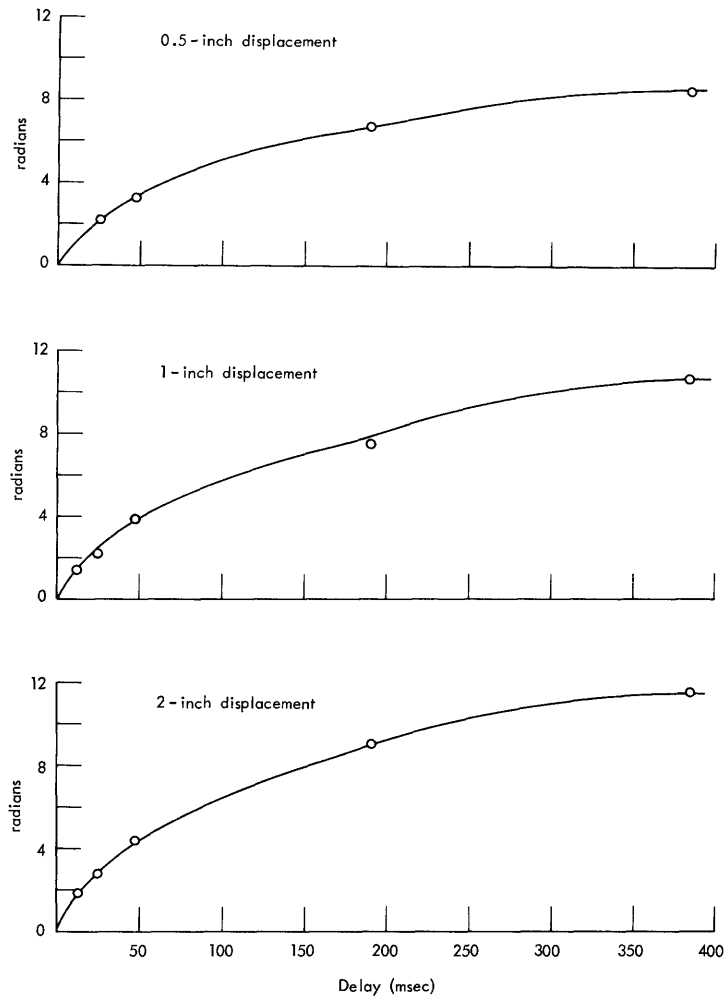

Fig. 52. Temporal phase-structure function.

mutual-coherence function can be made to undergo fading that is as severe as that encountered on the long atmospheric paths. In one particular example phase measurements were made using holes 1/8 inch in diameter. A set of temporal phase-structure functions is shown in Fig. 52. This shows much the same character as was obtained on paths through the atmosphere. The maximum variance in the phase is about the same

as obtained on the long path (springtime), although the correlation time seems to have about twice the former value. This last point can easily be taken into account in any simulation study.

Both of these laboratory measurements and the measurements made on the roof show only a small increase in the phase variance as the displacement is extended. This would all seem to suggest that the spatial structure function of the phase of the wavefront tends to saturate at just a very few correlation diameters. (By correlation diameter we mean the maximum aperture diameter for which a well-formed stationary Airy disk is observed.)

4.3 DISCUSSION OF RESULTS

As we have stated, our intention in this phase of the research was not to conduct an investigation in atmospheric physics but rather more to understand the general features of the turbulent atmosphere as a channel. The results obtained over the Museum of Science-Harvard College Observatory link are probably reasonably representative of the disturbances in the mutual-coherence function that are to be encountered over long horizontal paths, for example, as would be encountered in observing objects low on the horizon.

The results for the roof-top path are probably somewhat more representative of the shorter paths near zenith, although the channel may be a somewhat severe example, since it is a roof top with several ventilators and other sources of agitation.

We also demonstrated that a simple laboratory model can be used to give a reasonable simulation of the major effects of the turbulent atmosphere in distorting the received mutual-coherence process.

Finally, we would like to make a few comments on the coherence-measuring technique. It seems that the basic principle of scanning fringes is a good way to obtain the phase and amplitude processes. The actual scanning mechanism could be improved. The main problem that we encountered was inability to separate the interference signal from the baseband fading components when the fading was very rapid. The solution is to use a carrier of, perhaps, 2-3 kHz. With available Ronchi ruling line densities the reciprocating scanning techniques do not appear to be the best approach, however. A better approach may be to use a Ronchi ruling built into the rim of a scroll case which could be rotated at quite high speed. Another, and perhaps easier, approach would be to use a rotating disk consisting of lines ruled like the spokes on a wheel. If the diffraction pattern were confined to a small area near the periphery of the disk, the spokes would appear almost parallel, and the system would work just the same as for a conventional Ronchi ruling. A device of this latter form has been developed by Ramsey and Kobler[16] for monitoring the atmospheric seeing conditions. In all of these mechanical scanning techniques it appears necessary to maintain a reference signal such as the light-bulb arrangement used on our own scanner.

V. CONCLUSION

5.1 SUMMARY OF RESEARCH

The object of this work was to develop a reasonably thorough understanding of the limitations and possibilities of image estimation through the turbulent atmosphere. Although some approximations were unavoidably introduced to simplify the modelling procedure, we believe that the results still reflect the salient features of the general case.

We showed that if a receiver were given complete freedom in making field measurements, it could extract a sufficient set of data samples by determining the local mutual coherence of the incident radiation. That is, we found that the local mutual coherence of the field, rather than the instantaneous field function, constituted a statistically sufficient description of the process. Rather than extract a continuous record, a receiver may sample the process appropriately in the variables of frequency, time, position, and displacement (spatial frequency). We then studied the ways in which these coherence measurements are obtained and considered the unavoidable disturbances introduced by the detection device.

The resultant samples were then shown to be well modelled as random variables having Gaussian log-amplitude and phase caused by the atmosphere, and additive Gaussian noise components injected by the photodetection process. The extraction from these noisy coherence measurements of estimates of phase and amplitude of the spatial Fourier components in the object was next considered. Lower bounds to the variance of parameter estimates that could be expected from any unbiased processor were then found to fall into four general regions. When the signal strength is very high and the detector noise negligible, the variance is dependent only upon the severity of the turbulence. In this region a receiver that tracks the phase and log-amplitude distortion can achieve the lower bound. At lower signal levels the noise comes into play, and in region 2 it has a linear effect on the variance of both phase and amplitude estimates. This region is usually rather small, and lowering the signal-to-noise ratio brings us to region 3. Here the noise power acts quadratically on the variance of the amplitude estimate. A receiver that averages the square magnitude of the samples is almost optimum. The phase estimation problem, however, exhibits a threshold effect in this region. Once the noise is dominant in each sample there is no way to obtain good phase estimates with a sequence of samples at only one spatial frequency. If simultaneous measurements are available at neighboring spatial frequencies, estimates of the differential phase can be obtained whose variance has the quadratic form similar to that for amplitude estimation. Finally, when the signal-to-noise ratio is very poor, a fourth region may exist. Provided the object and receiver are rigidly secured, the variance may again increase only linearly with the noise power, but the only part of the signal that is really of use is the small residual mean component. The best receiver in this case is one that simply

integrates the coherence measurements.

The optimal techniques were then compared with various existing systems and some practical examples were considered.

The results of experimental channel studies were presented. Photographic measurements prove quite illustrative of the turbulent effects on the wave-front coherence. Spatial and temporal structure functions were also determined on both long and short optical paths and provide a more quantitative understanding of the severity of the disturbances encountered.

5.2 DESIGN PHILOSOPHY

From the examples presented, we are convinced that there is considerable merit in employing the more sophisticated data processing over the existing techniques. Indeed, it appears that a large class of problems will fall within regions 2 and 3, in which the square law and crosscorrelator receivers have truly significant gain over the integration technique.

Unfortunately, just as in channel coding and decoding, our enthusiasm for optimal signal processing is somewhat dampened when we come to practical realization. The receiver structures for regions 2 and 3 require an operation of the form: sample, square-law, and integration. This involved operation cannot be realized easily in an optical instrument as, for example, the simple integration of the mutual coherence by means of a long exposure photograph can be. Thus it appears that optimal processing, at least at present, requires additional off-line computing hardware. If, then, we are going to insist on recreating a full picture of the object, the sheer number of spatial frequencies to be estimated is very discouraging. On the other hand, high-fidelity pictures, though aesthetically pleasing, may often be a very expensive method of obtaining the actually desired information. For example, if all we really want to know are the general dimensions of the object, we can usually obtain these answers simply from an estimate of the roll-off characteristics of the magnitude of the spatial Fourier transform. Thus one of the fundamental engineering tasks is to distinctly define the estimating assignment. After clearly understanding what is the desired information and what in turn are the significant parameters of the spatial Fourier transform that must be determined, we can then turn to the hardware aspects of the problem.

Most likely we shall be unwilling to go to the expense of exploiting all of the available channel diversity, and we shall accept some sacrifice in performance for receiver cost reduction. The optical frequency diversity would probably first be discarded to avoid the expense of parallel sets of nonabsorption bandpass filters. Likewise we might be tempted to discard spatial diversity because each independent spatial sample requires a distinct detector element. Time diversity is likely to be the most attractive to exploit.

The choice of detecting element is also a prime consideration. Photography has been an attractive medium for image recording, primarily because of the large spatial information capacity. For our applications, however, a direct photoelectric detector

such as a photomultiplier is probably more suitable, because of the increased quantum efficiency and dynamic range.

Because of the number of correlation products and averages that must be computed, and the need to avoid any systematic biases, it appears that off-line digital processing would not only be cheaper but more reliable than analogue schemes.

5.3 SUGGESTIONS FOR FURTHER RESEARCH

The basic aspects of the imaging problem are now sufficiently well developed that the emphasis should next be placed on applying the techniques of signal processing to problems of actual practical interest. This will require convincing experimental demonstrations of the merits of more sophisticated processing over existing techniques.

Some of the desirable experimental research is possible over the Museum of Science-Harvard Observatory path. As we have mentioned, a mercury arc lamp with various spatial frequency gratings was used to some extent, but our work with this was primarily heuristic. It would be very worth while to continue an experimental verification of our results with the use of such a system. One should, however, replace the present lamp with a direct-current model in order to eliminate the annoying 120-Hz fluctuations.

In terms of channel measurements there is, of course, much more that can be done. Even the lowly phase-structure measurements should be examined further, probably with smaller separations than the minimum of 2 inches that we employed so that the saturation characteristics might be better understood. Undoubtedly, the disappearance of the 5/3 behavior in our measurements will be disconcerting to some, and it would be desirable to obtain confirmation (or perhaps denial) by an independent observer. In conducting additional phase structure function measurements, we suggest that a better fringe scanner be used so that measurements can also be taken at times of more rapid amplitude fading than we could study.

Other important aspects of the problem which also deserve study, both experimentally and theoretically, are the angular and optical frequency dependencies of the atmospheric disturbances. A good physical understanding of just when the channel is underspread or overspread would be valuable. Indeed the whole problem of the overspread channel, that is, when the angular correlation scale is too small to be resolved by a lens matched to a coherence area, has been left untouched.

Recently developed lasers operating simultaneously on several wavelengths would be very useful tools for studying the optical frequency correlation properties of the disturbances.

Our analysis of the problem was primarily classical, and as is the case when tackling a problem that is basically quantum in nature, we run into the difficulty that strict system optimization is somewhat of a cut-and-try proposition, since, as observers, we inevitably affect the experiment. A strict quantum-theory approach might prove quite worthwhile, especially if it could indicate directly the best measurement operator to employ.

Finally, if all of these suggestions are exhausted, the problem of making the processors more practically attractive will probably always be open. It has been twenty years since Claude E. Shannon showed the tremendous merits of channel coding, and still the problems of efficient decoder design persist.

Appendix A

(Section II)

A.1 ERROR BETWEEN SAMPLE AND ENSEMBLE AVERAGES OF MUTUAL COHERENCE

The mean-square error in the sample average mutual coherence is

$$\overline{|\epsilon|^2} = \overline{|\hat{\Gamma}_v(\underline{x},\underline{x}',t) - \overline{\hat{\Gamma}_v(\underline{x},\underline{x}',t)}|^2}$$

$$= \overline{|\hat{\Gamma}_v(\underline{x},\underline{x}',t)|^2} - |\overline{\hat{\Gamma}_v(\underline{x},\underline{x}',t)}|^2. \qquad \text{(A. 1)}$$

The first term is

$$\overline{|\hat{\Gamma}_v(\underline{x},\underline{x}',t)|^2} = \Delta x^4 \int_{\Delta T} dt \int_{\Delta T} dt' \; \overline{E_v(\underline{x},t)\, \overset{*}{E}_v(\underline{x}',t)\, \overset{*}{E}_v(\underline{x},t')\, E_v(\underline{x}',t')}. \qquad \text{(A. 2)}$$

The fourth-order expectation can be reduced, since the process $E_v(\underline{x},t)$ is Gaussian, and we are therefore able to rewrite (A. 2)

$$\overline{|\hat{\Gamma}_v(\underline{x},\underline{x}',t)|^2} = R_1 + R_2 + R_3, \qquad \text{(A. 3)}$$

where

$$R_1 = \Delta x^4 \int_{\Delta T} dt \int_{\Delta T} dt' \; \overline{E_v(\underline{x},t)\, \overset{*}{E}_v(\underline{x}',t)}\; \overline{\overset{*}{E}_v(\underline{x},t')\, E_v(\underline{x}',t')}$$

$$R_2 = \Delta x^4 \int_{\Delta T} dt \int_{\Delta T} dt' \; \overline{E_v(\underline{x},t)\, E_v(\underline{x}',t')}\; \overline{\overset{*}{E}_v(\underline{x}',t)\, \overset{*}{E}_v(\underline{x},t')}$$

$$R_3 = \Delta x^4 \int_{\Delta T} dt \int_{\Delta T} dt' \; \overline{E_v(\underline{x},t)\, \overset{*}{E}_v(\underline{x},t')}\; \overline{\overset{*}{E}_v(\underline{x}',t)\, E_v(\underline{x}',t')}. \qquad \text{(A. 4)}$$

The first term in expression (A.4) is simply $|\overline{\hat{\Gamma}_v(\underline{x},\underline{x}',t)}|^2$, which conveniently cancels with the second term of (A. 1). The middle term has zero expectation, because of the uniform distribution of the phase angle of each radiation process. Only the final term remains.

We now revert to the Fourier series

$$E_v(\underline{x},t) = \frac{1}{\Delta T^{1/2}} \sum_{m=Mq}^{M(q+1)-1} E_{n,m}(\underline{x})\, e^{-j2\pi mt/\Delta T} \qquad n\Delta T \leq t \leq (n+1)\Delta T \qquad \text{(A. 5)}$$

and exploit the following properties:

1. different optical frequency components are uncorrelated
2. $e^{-j2\pi mt/\Delta T}$ and $e^{+j2\pi m't/\Delta T}$ are orthogonal over the ΔT interval when $m \neq m'$

to find

$$\overline{|\epsilon|^2} = \Delta x^4 \sum_{m=Mq}^{M(q+1)-1} \overline{|E_{n,m}(\underline{x})|^2}\ \overline{|E_{n,m}(\underline{x}')|^2}. \tag{A.6}$$

Upon setting $M = \Delta T\ \Delta v$ and rewriting $\overline{|E_{n,m}(\underline{x})|^2}$ in terms of the object and noise power, we obtain

$$\overline{|\epsilon|^2} = \Delta T\ \Delta v\ \Delta x^4 \left[\circledcirc_v(O)\, e^{2a_v(\underline{x}, t)} + N_v \Omega \right] \left[\circledcirc_v(O)\, e^{2a_v(x', t)} + N_v \Omega \right]. \tag{A.7}$$

APPENDIX B

(Section III)

B.1 ASYMPTOTIC EXPANSION OF C-R INEQUALITY FOR SMALL VALUES OF A

We expand the right-hand side of Eq. 122 in a power series in A and retain only the lowest order terms. The condition of probability $p(r/A, \phi)$ is written

$$p(r/A, \phi) = \frac{1}{2\pi} \left\langle e^{-\frac{1}{2}\left[|r|^2 + A e^{2a} - 2|r| A^{1/2} \cos(b+\phi-\theta)\right]} \right\rangle_{a,b}, \tag{B.1}$$

where $r = |r| e^{j\theta}$ and $\langle \ \rangle_{a,b}$ denotes the averaging over the atmospheric functions a_i and b_i. Setting $A^{1/2} = x$, we have

$$\text{Variance } A = \frac{4A}{N E\left[\frac{\partial}{\partial x} \ln p(r/x, \phi)\right]^2}, \tag{B.2}$$

where

$$\frac{\partial}{\partial x} \ln p(r/x, \phi) = \frac{\left\langle |r| e^a \cos(b+\phi-\theta)\, e^{x|r| e^a \cos(b+\phi-\theta) - x^2 e^{2a}/2} \right\rangle_{a,b}}{\left\langle e^{x|r| e^a \cos(b+\phi-\theta) - x^2 e^{2a}/2} \right\rangle_{a,b}}. \tag{B.3}$$

We now expand expression (B.3) as a ratio of power series in x as

$$\frac{\partial}{\partial x} \ln p(r/x, \phi) = \frac{\gamma_o + \gamma_1 x + \gamma_2 x^2 \cdots}{1 + \delta_1 x + \delta_2 x^2 \cdots} \tag{B.4}$$

and find for the numerator coefficients

$$\gamma_o = \langle |r| e^a \cos(b+\phi-\theta) \rangle_{a,b}$$

$$= |r| D_1 B_1 \cos(\phi-\theta)$$

$$\gamma_1 = \langle |r|^2 e^{2a} \cos^2(b+\phi-\theta) - e^{2a} \rangle_{a,b}$$

$$= \frac{|r|^2 D_2}{2} + \frac{|r|^2 D_2 B_2 \cos(2\phi-2\theta) - D_2}{2}$$

$$\gamma_2 = \left\langle \frac{-3}{2} |r| e^{3a} \cos(b+\phi-\theta) + \frac{1}{2} |r|^2 e^{3a} \cos^3(b+\phi-\theta) \right\rangle_{a,b}$$

$$= \frac{-3}{2} |r| D_3 B_1 + \frac{1}{2} |r|^2 D_3 \langle \cos^3(b+\phi-\theta) \rangle_b \qquad \text{(B. 5)}$$

and for the denominator

$$\delta_1 = \langle |r| e^a \cos(b+\phi-\theta) \rangle_{a,b}$$

$$= |r| D_1 B_1 \cos(\phi-\theta)$$

$$\delta_2 = \left\langle \frac{1}{2} |r|^2 e^{2a} \cos^2(b+\phi-\theta) - \frac{e^{2a}}{2} \right\rangle_{a,b}$$

$$= \frac{|r|^2 D_2}{4} [1 + B_2 \cos(2\phi-2\theta)] \frac{-D_2}{2}. \qquad \text{(B. 6)}$$

Dividing and squaring the two series gives the representation

$$\left[\frac{\partial}{\partial x} \ln p(r/x,\phi)\right]^2 = \gamma_o^2 + x2\gamma_o(\gamma_1 - \gamma_o\gamma_1)$$

$$+ x^2\left[2\gamma_o\left(\gamma_2 + \delta_1^2\gamma_o - \delta_2\gamma_o - \delta_1\gamma_1\right) - (\gamma_1 - \gamma_o\gamma_1)^2\right]$$

$$+ \text{higher order terms in } x. \qquad \text{(B. 7)}$$

This expression must now be averaged over the random variable r which is itself dependent upon x. If we express the resultant average as the power series

$$\text{Er}\left[\frac{\partial \ln p(r/x,\phi)}{\partial x}\right]^2 = g_o + g_1 x + g_2 x^2 + \ldots, \qquad \text{(B. 8)}$$

we find that g_o, the zero-order term in $\overline{\gamma_o^2}$, is

$$g_o = \overline{\gamma_o^2}_{\text{zero-order}} = D_1^2 B_1^2. \qquad \text{(B. 9)}$$

Since $\overline{\gamma_o^2}$ contains only zero- and second-order terms, the coefficient g_1 must be the zero-order component of $\overline{2\gamma_o(\gamma_1 - \gamma_o\delta_1)}$, where

$$\overline{2\gamma_o(\gamma_1 - \gamma_o\delta_1)} = \overline{2|r| D_1 B_1 \cos(\phi-\theta)\left[\frac{|r|^2 D_2}{2} + \frac{|r|^2 D_2 B_2}{2}\cos(2\phi-2\theta) - D_2\right]}$$

$$- \overline{2|r|^3 D_1^3 B_1^3 \cos^3(\phi-\theta)}. \qquad \text{(B. 10)}$$

Upon inspection of this expression, we note that g_1 must be of order B_1^2 or less, and hence the term $g_1 x$ will only be significant in comparison with g_o (which also is of order B_1^2) when x is of the order of one or more. If we restrict ourselves only to values of x much less than one, the first-order term is then negligible.

The next coefficient in the expansion g_2 is composed of

1. the second-order component of $\overline{\gamma_o^2}$
2. the first-order component of $\overline{2\gamma_o(\gamma_1-\gamma_o\delta_1)}$
3. the zero-order component of $\overline{2\gamma_o\left(\gamma_2+\delta_1^2\gamma_o-\delta_2\gamma_o-\delta_1\gamma_1\right)+(\gamma_1-\gamma_o\delta_1)^2}$.

All of these components will be of the order of B_1^2 or less, except for part of the zero-order component of $\overline{(\gamma_1-\gamma_o\delta_1)^2}$. Since B_1 is very small in cases of practical interest (variance of b is very large), the only significant component of g_2 is $g_2 \approx D_2^2$.

An asymptotic approximation to the left-hand side of the C-R inequality can now be constructed by using only the first two significant terms $g_o + g_2 x^2$, and yields

$$\text{Variance } \hat{A} \geq \frac{4A}{N\left[D_1^2 B_1^2 + D_2^2 A\right]}. \tag{B.11}$$

If we normalize by dividing by A^2 we obtain

$$\frac{\text{Variance } \hat{A}}{A^2} \geq \frac{4}{N\left[D_1^2 B_1^2 A + D_2^2 A^2\right]}. \tag{B.12}$$

B.2 APPROXIMATION TO C-R INEQUALITY WHEN AMPLITUDE IS CONSTANT AND PHASE IS UNIFORM

Under the conditions of constant amplitude and uniform phase, the conditional probability of a particular r_i is

$$p(r/A,\phi) = \frac{e^{-\frac{1}{2}\left[|r|^2+AD_2^{1/2}\right]}}{2\pi} \frac{1}{2\pi}\int_0^{2\pi} e^{A^{1/2}D_2^{1/2}|r|\cos(b+\phi-\theta)}\, d\theta. \tag{B.13}$$

The inner integral can be expressed in terms of a zero-order modified Bessel function of the first kind $I_o(x)$ which is independent of ϕ and θ (see Wozencraft and Jacobs[22]), and we obtain

$$p(r/A,\phi) = \frac{1}{2} e^{-\frac{1}{2}\left[|r|^2+AD_2\right]} I_o\left(A^{1/2}D_2^{1/2}|r|\right). \tag{B.14}$$

Differentiating the logarithm of expression (B.14) twice with respect to A gives

$$\frac{\partial^2}{\partial A^2} \ln p(r/A, \phi) = \frac{I_o \frac{\partial^2}{\partial A^2} I_o - \left[\frac{\partial}{\partial A} I_o\right]^2}{I_o^2}. \tag{B.15}$$

The function $I_o(x)$ has the power-series expansion

$$I_o(x) = 1 + \frac{x^2}{2^2} + \frac{x^4}{2^2 4^2} + \frac{x^6}{2^2 4^2 6^2} + \ldots . \tag{B.16}$$

From a convexity argument we can show that the first term of the numerator of Eq. B.15 is always positive, and hence

$$-\frac{\partial^2}{\partial A^2} \ln p(r/A, \phi) \leq \left[\frac{\partial}{\partial A} \frac{I_o}{I_o}\right]^2. \tag{B.17}$$

Upon letting $x = A^{1/2} D_2^{1/2} r$, Eq. B.17 becomes

$$-\frac{\partial^2}{\partial A^2} \ln p(r/A, \phi) \leq \frac{D_2 |r|^2}{4A} \left[\frac{d}{dx} \frac{I_o(x)}{I_o(x)}\right]^2. \tag{B.18}$$

Furthermore, it can be shown by using the power-series expansion for $I_o(x)$ that

$$\frac{\frac{d}{dx} I_o(x)}{I_o(x)} \leq \frac{x}{2}; \tag{B.19}$$

hence,

$$-\frac{\partial^2}{\partial A^2} \ln p(r/A, \phi) \leq \frac{D_2^2}{16} \overline{|r|^4}. \tag{B.20}$$

Averaging over r yields

$$-\frac{\partial^2}{\partial A^2} \ln p(r/A\,\phi) \leq \frac{D_2^4 A^2 + 8D_2^3 A + 8D_2^2}{16}, \tag{B.21}$$

and the lower bound to the variance of A then is

$$\text{Variance } \hat{A} \geq \frac{1}{N} \frac{16}{D_2^4 A^2 + 8D_2^3 A + 8D_2^2}, \tag{B.22}$$

and dividing by A^2, we finally obtain

$$\frac{\text{Variance } \hat{A}}{A^2} \geq \frac{1}{N} \frac{16}{8D_2^2A^2 + 8D_2^3A^3 + D_2^4A^4}. \tag{B. 23}$$

B. 3 ASYMPTOTIC EXPANSION FOR C-R BOUND TO PHASE VARIANCE IN THE LIMIT OF VERY SMALL SIGNAL LEVEL

The C-R inequality requires

$$\frac{\partial}{\partial\phi} \ln p(r/A,\phi) = \frac{\left\langle -x|r|\, e^a \sin(b+\phi-\theta)\, e^{x|r|\, e^a \cos(b+\phi-\theta) - x^2 e^{2a}/2} \right\rangle_{a,b}}{\left\langle e^{x|r|\, e^a \cos(b+\phi-\theta) - x^2 e^{2a}/2} \right\rangle_{a,b}}, \tag{B. 24}$$

where $A^{1/2} = x$, and $r = |r|\, e^{j\theta}$. To first order in x, this behaves simply as

$$\frac{\partial}{\partial\phi} \ln p(r/A,\phi) \sim \langle -x|r|\, e^a \sin(b+\phi-\theta) \rangle_{a,b}$$

$$\sim -x|r|\, D_1 B_1 \sin(\phi-\theta). \tag{B. 25}$$

Squaring, averaging over r, and retaining only the lowest order term in x yields

$$\frac{\partial}{\partial\phi} \ln p(r/A,\phi)^2 \sim x^2 D_1^2 B_1^2. \tag{B. 26}$$

We thus obtain in the limit of very small A

$$\text{Variance } \hat{\phi} \geq \frac{1}{N D_1^2 B_1^2 A}. \tag{B. 27}$$

B. 4 APPROXIMATION TO C-R INEQUALITY FOR NOISY PHASE REFERENCE AND CONSTANT AMPLITUDE

The joint probability density of a pair of samples r_i and v_i (under the assumption that the fading coefficient e^{ai} is replaced by $D_2^{1/2}$) is

$$p(r,v/A,\phi) = \frac{1}{2\pi} e^{-\frac{1}{2}\left[|r|^2 + |v|^2 + 2A D_2\right]} \left\langle e^{A^{1/2} D_2^{1/2} [|r| \cos(b+\phi-\theta) + |v| \cos(b-\gamma)]} \right\rangle_b, \tag{B. 28}$$

where

$$r = |r|\, e^{j\theta} \quad \text{and} \quad v = |v|\, e^{j\gamma}. \tag{B. 29}$$

The term that must be averaged on b can be rewritten after some trigonometric gymnastics as

$$\langle\ \rangle_b = \left\langle e^{A^{1/2}D_2^{1/2}\left[|r|^2+|v|^2+2|r|\,|v|\cos(\phi+\gamma-\theta)\right]^{1/2}\cos(b+\delta)} \right\rangle_b. \tag{B.30}$$

The exact functional form of the angle δ is unimportant, since the average over b is independent of δ anyway. This average is again expressed in terms of the zero-order modified Bessel function $I_o(x)$ as

$$\langle\ \rangle_b = \frac{1}{2\pi}\, I_o\left[A^{1/2}D_2^{1/2}\left[|r|^2+|v|^2+2|r|\,|v|\cos(\phi+-\theta)\right]^{1/2}\right]. \tag{B.31}$$

It then follows that

$$\left[\frac{\partial}{\partial\phi}\ln p(r,v/A,\phi)\right]^2 = \left[\frac{d/dy\ I_o(y)}{I_o(y)}\right]^2\left[\frac{\partial y}{\partial x}\right]^2\left[\frac{\partial x}{\partial\phi}\right]^2, \tag{B.32}$$

where $y = x^{1/2}$, and $x = A\,D_2[|r|^2+|v|^2+2|r|\,|v|\cos(\phi+-\theta)]$.

With the aid of inequality (B.19) we obtain

$$\left[\frac{\partial}{\partial\phi}\ln p(r,v/A,\phi)\right]^2 = \frac{1}{4}A^2D_2^2\,|r|^2\,|v|^2\sin^2(\phi+-\theta). \tag{B.33}$$

This is now averaged over r and v to yield

$$\overline{\left[\frac{\partial}{\partial\phi}\ln p(r,v/A,\phi)\right]^2} = \frac{A^4D_2^4}{8}+\frac{A^3D_2^3}{2}+\frac{A^2D_2^2}{2}. \tag{B.34}$$

The final result then is

$$\text{Variance}\ \hat{\phi} \geq \frac{8}{N\left(4D_2^2A^2+4D_2^3A^3+D_2^4A^4\right)}. \tag{B.35}$$

Acknowledgment

I want to express my sincere gratitude to Professor Robert S. Kennedy who guided and encouraged me through the course of this study. I am also grateful to Professor Peter Elias and Professor Estil V. Hoversten for their reading of my thesis.

The cooperation of members of The Museum of Science, in Boston, and of Harvard College Observatory, in Cambridge, in making facilities available for the experimental work is greatly appreciated. My friends Seppo J. Halme and Jeffrey H. Shapiro must not be forgotten, as they patiently spent many a cold night on the roof tops aligning the laser.

I also wish to thank the Research Laboratory of Electronics, M.I.T., and the Defence Research Board of Canada for their assistance.

References

1. National Academy of Sciences U.S., "Restoration of Atmospherically Degraded Images," Vol. 1, 2, and 3, Woods Hole Summer Study, July 1966 (Defense Documentation Center, Cameron Station, Alexandria, Virginia).
2. M. Born and W. Wolf, Principles of Optics (Pergamon Press, London, 1959).
3. R. E. Hufnagel and N. R. Stanley, "Modulation Transfer Function Associated with Image Transmission through Turbulent Media," J. Opt. Soc. Am. 54, 52-61 (1964).
4. D. L. Fried, "Optical Resolution through a Randomly Inhomogeneous Medium for Very Long and Very Short Exposures," J. Opt. Soc. Am. 56, 1372-1379 (1966).
5. V. I. Tatarski, Wave Propogation in a Turbulent Medium (McGraw-Hill Book Company, Inc., New York, 1961).
6. E. Djurle and A. Back, "Some Measurements of the Effects of Air Turbulence on Photographic Images," J. Opt. Soc. Am. 51, 1029-1030 (1961).
7. J. L. Harris, Sr., "Image Evaluation and Restoration," J. Opt. Soc. Am. 56, 569-574 (1966).
8. C. W. Helstrom, "Image Restoration by Method of Least Squares," J. Opt. Soc. Am. 57, 297-303 (1967).
9. Y. W. Lee, Statistical Theory of Communication (John Wiley and Sons, Inc., New York, 1960).
10. G. R. Heidbreder, "Image Degradation with Random Waveform Tilt Compensation," IEEE Trans. on Antennas and Propagation (Special Issue on Partial Coherence), Vol. AP-15, No. 1, January 1967.
11. R. Hanbury Brown and R. Q. Twiss, "Interferometry of the Intensity Fluctuations in Light I," Proc. Roy. Soc. (London) A242, 300 (1957).
12. R. Hanbury Brown and R. Q. Twiss, "Interferometry of the Intensity Fluctuations in Light II," Proc. Roy. Soc. (London) A243, 291 (1958).
13. H. L. Van Trees, Detection, Estimation and Modulation Theory, Part I (John Wiley and Sons, Inc., New York, 1968); see especially p. 178.
14. A. A. M. Saleh, "Laser Wave Depolarization by Atmospheric Transmission," S. M. Thesis, Department of Electrical Engineering, Massachusetts Institute of Technology, June 1968.
15. H. L. Van Trees, op. cit., p. 66.
16. J. V. Ramsay and H. Kobler, "A Stellar Image Monitor," Observatory 82, 107 (June 1962).
17. M. Born and W. Wolf, op. cit., p. 270.
18. J. E. Ehrenberg, "A Study of the Effects of Atmospheric Turbulence on Intensity Properties at 6328 Å and 1.15 μ," S. M. Thesis, Department of Electrical Engineering, Massachusetts Institute of Technology, February 1968.
19. D. L. Fried, "Statistics of Geometric Representation of Wavefront Distortion," J. Opt. Soc. Am. 55, 1427-1435 (1965).
20. J. H. Shapiro, " A Plane Wave Model for a Turbulence Corrupted Laser Beam," S. M. Thesis, Department of Electrical Engineering, Massachusetts Institute of Technology, September 1968.
21. M. Tamny, "Heterodyne Measurements of Atmospheric Turbulence at 6328 Å," S. M. Thesis, Department of Electrical Engineering, Massachusetts Institute of Technology, June 1968.
22. J. M. Wozencraft and I. M. Jacobs, Principles of Communication Engineering (John Wiley and Sons, Inc., New York, 1965), see p. 515.

JOINT SERVICES ELECTRONICS PROGRAM
REPORTS DISTRIBUTION LIST

Department of Defense

Dr. A. A. Dougal
Asst Director (Research)
Ofc of Defense Res & Eng
Department of Defense
Washington, D. C. 20301

Office of Deputy Director
(Research and Information, Rm 3D1037)
Department of Defense
The Pentagon
Washington, D. C. 20301

Director
Advanced Research Projects Agency
Department of Defense
Washington, D. C. 20301

Director for Materials Sciences
Advanced Research Projects Agency
Department of Defense
Washington, D. C. 20301

Headquarters
Defense Communications Agency (340)
Washington, D. C. 20305

Defense Documentation Center
Attn: DDC-TCA
Cameron Station
Alexandria, Virginia 22314

Director
National Security Agency
Attn: TDL
Fort George G. Meade, Maryland 20755

Weapons Systems Evaluation Group
Attn: Colonel Blaine O. Vogt
400 Army-Navy Drive
Arlington, Virginia 22202

Central Intelligence Agency
Attn: OCR/DD Publications
Washington, D. C. 20505

Department of the Air Force

Hq USAF (AFRDDD)
The Pentagon
Washington, D. C. 20330

Hq USAF (AFRDDG)
The Pentagon
Washington, D. C. 20330

Hq USAF (AFRDSD)
The Pentagon
Washington, D. C. 20330

Colonel E. P. Gaines, Jr.
ACDA/FO
1901 Pennsylvania Avenue N. W.
Washington, D. C. 20451

Lt Col R. B. Kalisch (SREE)
Chief, Electronics Division
Directorate of Engineering Sciences
Air Force Office of Scientific Research
Arlington, Virginia 22209

Dr. I. R. Mirman
AFSC (SCT)
Andrews Air Force Base, Maryland 20331

AFSC (SCTSE)
Andrews Air Force Base, Maryland 20331

Mr. Morton M. Pavane, Chief
AFSC Scientific and Technical Liaison
Office
26 Federal Plaza, Suite 1313
New York, New York 10007

Rome Air Development Center
Attn: Documents Library (EMTLD)
Griffiss Air Force Base, New York 13440

Mr. H. E. Webb (EMIIS)
Rome Air Development Center
Griffiss Air Force Base, New York 13440

Dr. L. M. Hollingsworth
AFCRL (CRN)
L. G. Hanscom Field
Bedford, Massachusetts 01730

AFCRL (CRMPLR), Stop 29
AFCRL Research Library
L. G. Hanscom Field
Bedford, Massachusetts 01730

Hq ESD (ESTI)
L. G. Hanscom Field
Bedford, Massachusetts 01730

Professor J. J. D'Azzo
Dept of Electrical Engineering
Air Force Institute of Technology,
Wright-Patterson Air Force Base,
Ohio 45433

Dr. H. V. Noble (CAVT)
Air Force Avionics Laboratory
Wright-Patterson Air Force Base,
Ohio 45433

Director
Air Force Avionics Laboratory
Wright-Patterson Air Force Base,
Ohio 45433

AFAL (AVTA/R. D. Larson)
Wright-Patterson Air Force Base,
Ohio 45433

Director of Faculty Research
Department of the Air Force
U.S. Air Force Academy
Colorado Springs, Colorado 80840

Academy Library (DFSLB)
USAF Academy
Colorado Springs, Colorado 80840

Director
Aerospace Mechanics Division
Frank J. Seiler Research Laboratory (OAR)
USAF Academy
Colorado Springs, Colorado 80840

Director, USAF PROJECT RAND
Via: Air Force Liaison Office
The RAND Corporation
Attn: Library D
1700 Main Street
Santa Monica, California 90406

Hq SAMSO (SMTTA/Lt Nelson)
Air Force Unit Post Office
Los Angeles, California 90045

Det 6, Hq OAR
Air Force Unit Post Office
Los Angeles, California 90045

AUL3T-9663
Maxwell Air Force Base, Alabama 36112

AFETR Technical Library
(ETV, MU-135)
Patrick Air Force Base, Florida 32925

ADTC (ADBPS-12)
Eglin Air Force Base, Florida 32542

Mr. B. R. Locke
Technical Adviser, Requirements
USAF Security Service
Kelly Air Force Base, Texas 78241

Hq AMD (AMR)
Brooks Air Force Base, Texas 78235

USAFSAM (SMKOR)
Brooks Air Force Base, Texas 78235

Commanding General
Attn: STEWS-RE-L, Technical Library
White Sands Missile Range,
New Mexico 88002

Hq AEDC (AETS)
Attn: Library/Documents
Arnold Air Force Station, Tennessee 37389

European Office of Aerospace Research
APO New York 09667

Department of the Army

Physical & Engineering Sciences Division
U.S. Army Research Office
3045 Columbia Pike
Arlington, Virginia 22204

Commanding General
U.S. Army Security Agency
Attn: IARD-T
Arlington Hall Station
Arlington, Virginia 22212

Commanding General
U.S. Army Materiel Command
Attn: AMCRD-TP
Washington, D. C. 20315

Commanding Officer
Harry Diamond Laboratories
Attn: Dr. Berthold Altman (AMXDO-TI)
Connecticut Avenue and
Van Ness Street N. W.
Washington, D. C. 20438

Director
Walter Reed Army Institute of Research
Walter Reed Army Medical Center
Washington, D. C. 20012

Commanding Officer (AMXRD-BAT)
U.S. Army Ballistics Research Laboratory
Aberdeen Proving Ground
Aberdeen, Maryland 21005

Technical Director
U.S. Army Limited War Laboratory
Aberdeen Proving Ground
Aberdeen, Maryland 21005

Commanding Officer
Human Engineering Laboratories
Aberdeen Proving Ground
Aberdeen, Maryland 21005

U.S. Army Munitions Command
Attn: Science & Technology Information Branch, Bldg 59
Picatinny Arsenal, SMUPA-VA6
Dover, New Jersey 07801

U.S. Army Mobility Equipment Research and Development Center
Attn: Technical Document Center, Bldg 315
Fort Belvoir, Virginia 22060

Director
U.S. Army Engineer Geodesy, Intelligence & Mapping Research and Development Agency
Fort Belvoir, Virginia 22060

Dr. Herman Robl
Deputy Chief Scientist
U.S. Army Research Office (Durham)
Box CM, Duke Station
Durham, North Carolina 27706

Richard O. Ulsh (CRDARD-IPO)
U.S. Army Research Office (Durham)
Box CM, Duke Station
Durham, North Carolina 27706

Technical Director (SMUFA-A2000-107-1)
Frankford Arsenal
Philadelphia, Pennsylvania 19137

Redstone Scientific Information Center
Attn: Chief Document Section
U.S. Army Missile Command
Redstone Arsenal, Alabama 35809

Commanding General
U.S. Army Missile Command
Attn: AMSMI-REX
Redstone Arsenal, Alabama 35809

Commanding General
U.S. Army Strategic Communications Command
Attn: SCC-CG-SAE
Fort Huachuca, Arizona 85613

Commanding Officer
Army Materials and Mechanics Research Center
Attn: Dr. H. Priest
Watertown Arsenal
Watertown, Massachusetts 02172

Commandant
U.S. Army Air Defense School
Attn: Missile Science Division, C&S Dept,
P. O. Box 9390
Fort Bliss, Texas 79916

Commandant
U.S. Army Command and General Staff College
Attn: Acquisitions, Lib Div
Fort Leavenworth, Kansas 66027

Commanding Officer
U.S. Army Electronics R&D Activity
White Sands Missile Range,
New Mexico 88002

Mr. Norman J. Field, AMSEL-RD-S
Chief, Office of Science & Technology
Research and Development Directorate
U.S. Army Electronics Command
Fort Monmouth, New Jersey 07703

Mr. Robert O. Parker, AMSEL-RD-S
Executive Secretary, JSTAC
U. S. Army Electronics Command
Fort Monmouth, New Jersey 07703

Commanding General
U.S. Army Electronics Command
Fort Monmouth, New Jersey 07703
Attn: AMSEL-SC
RD-GF
RD-MT
XL-D
XL-E
XL-C
XL-S (Dr. R. Buser)
HL-CT-DD
HL-CT-R
HL-CT-L (Dr. W.S. McAfee)
HL-CT-O
HL-CT-I
HL-CT-A
NL-D
NL-A
NL-P
NL-P-2 (Mr. D. Haratz)
NL-R (Mr. R. Kulinyi)
NL-S
KL-D
KL-E
KL-S (Dr. H. Jacobs)
KL-SM (Drs. Schiel/Hieslmair)
KL-T
VL-D
VL-F (Mr. R.J. Niemela)
WL-D

Dr. A. D. Schnitzler, AMSEL-HL-NVII
Night Vision Laboratory, USAECOM
Fort Belvoir, Virginia 22060

Dr. G. M. Janney, AMSEL-HL-NVOR
Night Vision Laboratory, USAECOM
Fort Belvoir, Virginia 22060

Atmospheric Sciences Office
Atmospheric Sciences Laboratory
White Sands Missile Range,
New Mexico 88002

Missile Electronic Warfare Technical
Area, (AMSEL-WT-MT)
White Sands Missile Range,
New Mexico 88002

Deputy for Research and Engineering
(AMSWE-DRE)
U.S. Army Weapons Command
Rock Island Arsenal
Rock Island, Illinois 61201

Project Manager
Common Positioning & Navigation Systems
Attn: Harold H. Bahr (AMCPM-NS-TM),
Bldg 439
U.S. Army Electronics Command
Fort Monmouth, New Jersey 07703

Director
U.S. Army Advanced Materiel
Concepts Agency
Washington, D. C. 20315

Department of the Navy

Director, Electronic Programs
Attn: Code 427
Department of the Navy
Washington, D. C. 20360

Commander
U.S. Naval Security Group Command
Attn: G43
3801 Nebraska Avenue
Washington, D. C. 20390

Director
Naval Research Laboratory
Washington, D. C. 20390
Attn: Code 2027
Dr. W. C. Hall, Code 7000
Dr. A. Brodzinsky, Supt. Elec. Div.

Dr. G. M. R. Winkler
Director, Time Service Division
U.S. Naval Observatory
Washington, D. C. 20390

Naval Air Systems Command
AIR 03
Washington, D. C. 20360

Naval Ship Systems Command
Ship 031
Washington, D. C. 20360

Naval Ship Systems Command
Ship 035
Washington, D. C. 20360

U. S. Naval Weapons Laboratory
Dahlgren, Virginia 22448

Naval Electronic Systems Command
ELEX 03, Room 2046 Munitions Building
Department of the Navy
Washington, D. C. 20360

Head, Technical Services Division
Naval Investigative Service Headquarters
4420 North Fairfax Drive
Arlington, Virginia 22203

Commander
U.S. Naval Ordnance Laboratory
Attn: Librarian
White Oak, Maryland 21502

Commanding Officer
Office of Naval Research Branch Office
Box 39 FPO
New York, New York 09510

Commanding Officer
Office of Naval Research Branch Office
219 South Dearborn Street
Chicago, Illinois 60604

Commanding Officer
Office of Naval Research Branch Office
495 Summer Street
Boston, Massachusetts 02210

Commander (ADL)
Naval Air Development Center
Johnsville, Warminster,
Pennsylvania 18974

Commanding Officer
Naval Training Device Center
Orlando, Florida 32813

Commander (Code 753)
Naval Weapons Center
Attn: Technical Library
China Lake, California 93555

Commanding Officer
Naval Weapons Center
Corona Laboratories
Attn: Library
Corona, California 91720

Commander
U.S. Naval Missile Center
Point Mugu, California 93041

W. A. Eberspacher, Associate Head
Systems Integration Division
Code 5340A, Box 15
U.S. Naval Missile Center
Point Mugu, California 93041

Commander
Naval Electronics Laboratory Center
Attn: Library
San Diego, California 92152

Deputy Director and Chief Scientist
Office of Naval Research Branch Office
1030 East Green Street
Pasadena, California 91101

Library (Code 2124)
Technical Report Section
Naval Postgraduate School
Monterey, California 93940

Glen A. Myers (Code 52 Mv)
Assoc. Prof. of Electrical Engineering
Naval Postgraduate School
Monterey, California 93940

Commanding Officer and Director
U.S. Naval Underwater Sound Laboratory
Fort Trumbull
New London, Connecticut 06840

Commanding Officer
Naval Avionics Facility
Indianapolis, Indiana 46241

Other Government Agencies

Dr. H. Harrison, Code RRE
Chief, Electrophysics Branch
National Aeronautics and
Space Administration
Washington, D. C. 20546

NASA Lewis Research Center
Attn: Library
21000 Brookpark Road
Cleveland, Ohio 44135

Los Alamos Scientific Laboratory
Attn: Reports Library
P. O. Box 1663
Los Alamos, New Mexico 87544

Federal Aviation Administration
Attn: Admin Stds Div (MS-110)
800 Independence Avenue S. W.
Washington, D. C. 20590

Mr. M. Zane Thornton, Chief
Network Engineering, Communications
and Operations Branch
Lister Hill National Center for
Biomedical Communications
8600 Rockville Pike
Bethesda, Maryland 20014

U. S. Post Office Department
Library - Room 6012
12th & Pennsylvania Avenue, N. W.
Washington, D. C. 20260

Non-Government Agencies

Director
Research Laboratory of Electronics
Massachusetts Institute of Technology
Cambridge, Massachusetts 02139

Mr. Jerome Fox, Research Coordinator
Polytechnic Institute of Brooklyn
333 Jay Street
Brooklyn, New York 11201

Director
Columbia Radiation Laboratory
Columbia University
538 West 120th Street
New York, New York 10027

Director
Coordinated Science Laboratory
University of Illinois
Urbana, Illinois 61801

Director
Stanford Electronics Laboratories
Stanford University
Stanford, California 94305

Director
Microwave Physics Laboratory
Stanford University
Stanford, California 94305

Director
Electronics Research Laboratory
University of California
Berkeley, California 94720

Director
Electronic Sciences Laboratory
University of Southern California
Los Angeles, California 90007

Director
Electronics Research Center
The University of Texas at Austin
Austin, Texas 78712

Division of Engineering and
Applied Physics
Harvard University
Cambridge, Massachusetts 02138

Dr. G. J. Murphy
The Technological Institute
Northwestern University
Evanston, Illinois 60201

Dr. John C. Hancock, Head
School of Electrical Engineering
Purdue University
Lafayette, Indiana 47907

Department of Electrical Engineering
Texas Technological College
Lubbock, Texas 79409

Aerospace Corporation
P. O. Box 95085
Los Angeles, California 90045
Attn: Library Acquisition Group

Prof. Nicholas George
California Institute of Technology
Pasadena, California 91109

Aeronautics Library
Graduate Aeronautical Laboratories
California Institute of Technology
1201 E. California Blvd.
Pasadena, California 91109

The Johns Hopkins University
Applied Physics Laboratory
Attn: Document Librarian
8621 Georgia Avenue
Silver Spring, Maryland 20910

Hunt Library
Carnegie-Mellon University
Schenley Park
Pittsburgh, Pennsylvania 15213

Dr. Leo Young
Stanford Research Institute
Menlo Park, California 94025

School of Engineering Sciences
Arizona State University
Tempe, Arizona 85281

Engineering and Mathematical
Sciences Library
University of California at Los Angeles
405 Hilgard Avenue
Los Angeles, California 90024

The Library
Government Publications Section
University of California
Santa Barbara, California 93106

Carnegie-Mellon University
Electrical Engineering Department
Pittsburgh, Pennsylvania 15213

Prof. Joseph E. Rowe
Chairman, Dept of Electrical Engineering
The University of Michigan
Ann Arbor, Michigan 48104

New York University
College of Engineering
New York, New York 10019

Syracuse University
Department of Electrical Engineering
Syracuse, New York 13210

Yale University
Engineering Department
New Haven, Connecticut 06520

Airborne Instruments Laboratory
Deerpark, New York 11729

Raytheon Company
Attn: Librarian
Bedford, Massachusetts 01730

Raytheon Company
Research Division Library
28 Seyon Street
Waltham, Massachusetts 02154

Dr. Sheldon J. Welles
Electronic Properties Information Center
Mail Station E-175
Hughes Aircraft Company
Culver City, California 90230

Dr. Robert E. Fontana
Systems Research Laboratories Inc.
7001 Indian Ripple Road
Dayton, Ohio 45440

Nuclear Instrumentation Group
Bldg 29, Room 101
Lawrence Radiation Laboratory
University of California
Berkeley, California 94720

Sylvania Electronic Systems
Applied Research Laboratory
Attn: Documents Librarian
40 Sylvan Road
Waltham, Massachusetts 02154

Hollander Associates
P. O. Box 2276
Fullerton, California 92633

Illinois Institute of Technology
Department of Electrical Engineering
Chicago, Illinois 60616

The University of Arizona
Department of Electrical Engineering
Tucson, Arizona 85721

Utah State University
Department of Electrical Engineering
Logan, Utah 84321

Case Western Reserve University
Engineering Division
University Circle
Cleveland, Ohio 44106

Lincoln Laboratory
Massachusetts Institute of Technology
Lexington, Massachusetts 02173

The University of Iowa
The University Libraries
Iowa City, Iowa 52240

Lenkurt Electric Co., Inc.
1105 County Road
San Carlos, California 94070
Attn: Mr. E. K. Peterson

Philco Ford Corporation
Communications & Electronics Division
Union Meeting and Jolly Roads
Blue Bell, Pennsylvania 19422

Union Carbide Corporation
Electronic Division
P. O. Box 1209
Mountain View, California 94041

Department of Electrical Engineering
Rice University
Houston, Texas 77001

Research Laboratories for the
Engineering Sciences
School of Engineering and Applied Science
University of Virginia
Charlottesville, Virginia 22903

Department of Electrical Engineering
College of Engineering and Technology
Ohio University
Athens, Ohio 45701

Project MAC
Document Room
Massachusetts Institute of Technology
545 Technology Square
Cambridge, Massachusetts 02139

Department of Electrical Engineering
Lehigh University
Bethlehem, Pennsylvania 18015

UNCLASSIFIED

Security Classification

DOCUMENT CONTROL DATA - R & D

(Security classification of title, body of abstract and indexing annotation must be entered when the overall report is classified)

1. ORIGINATING ACTIVITY *(Corporate author)*
Research Laboratory of Electronics
Massachusetts Institute of Technology
Cambridge, Massachusetts 02139

2a. REPORT SECURITY CLASSIFICATION
Unclassified

2b. GROUP

3. REPORT TITLE
Imaging of Objects Viewed through a Turbulent Atmosphere

4. DESCRIPTIVE NOTES *(Type of report and inclusive dates)*
Technical Report

5. AUTHOR(S) *(First name, middle initial, last name)*
John C. Moldon

6. REPORT DATE	7a. TOTAL NO. OF PAGES	7b. NO. OF REFS
March 3, 1969	124	22

8a. CONTRACT OR GRANT NO.	9a. ORIGINATOR'S REPORT NUMBER(S)
DA 28-043-AMC-02536(E)	Technical Report 469
b. PROJECT NO. 200-14501-B31F	
c. NASA Grant NGL 22-009-013	9b. OTHER REPORT NO(S) *(Any other numbers that may be assigned this report)*
d.	None

10. DISTRIBUTION STATEMENT
This document has been approved for public release and sale; its distribution is unlimited.

11. SUPPLEMENTARY NOTES	12. SPONSORING MILITARY ACTIVITY
	Joint Services Electronics Program through U.S. Army Electronics Command

13. ABSTRACT

This report is concerned with estimating the high-resolution amplitude and phase parameters of the spatial Fourier transform of an object illuminated with incoherent radiation and viewed through a turbulent atmosphere.

The Cramer-Rao technique is employed to lower-bound the variance of any unbiased estimator, and receiver structures that approach these bounds are then exhibited. It is found that significant improvement over many existing systems is often possible, provided one is willing to pay for increased system complexity. The reduction of the processors to somewhat less efficient but more practically attractive forms is then considered.

Some experimental results are presented which illustrate the effects of turbulence on wave-front coherence.

DD FORM 1 NOV 65 1473

UNCLASSIFIED

Security Classification

14. KEY WORDS	LINK A		LINK B		LINK C	
	ROLE	WT	ROLE	WT	ROLE	WT
Atmospheric Optics						
High-resolution Imaging						
Pattern Recognition						